Automatic Affine and Elastic Registration Strategies for

Multi-Dimensional Medical Images

by

Wei Huang

A Dissertation

Submitted to the Faculty of the

WORCESTER POLYTECHNIC INSTITUTE

in partial fulfillment of the requirements for the

Degree of Doctor of Philosophy

in

Mechanical Engineering

_____

May 2007

Committee Approval:

_____ _____

Prof. John M. Sullivan, Jr., Advisor   Prof. Reinhold Ludwig, Committee Member

_____ _____

Prof. Allen H. Hoffman, Committee Member   Dr. Jean King, Committee Member

_____

Prof. Kevin (Yiming) Rong, Graduate Committee Representative

ABSTRACT

Medical images have been used increasingly for diagnosis, treatment planning, monitoring disease processes, and other medical applications. A large variety of medical imaging modalities exists including CT, X-ray, MRI, Ultrasound, etc. Frequently a group of images need to be compared to one another and/or combined for research or cumulative purposes. In many medical studies, multiple images are acquired from subjects at different times or with different imaging modalities. Misalignment inevitably occurs, causing anatomical and/or functional feature shifts within the images. Computerized image registration (alignment) approaches can offer automatic and accurate image alignments without extensive user involvement and provide tools for visualizing combined images.

This dissertation focuses on providing automatic image registration strategies. After a through review of existing image registration techniques, we identified two registration strategies that enhance the current field: (1) an automated rigid body and affine registration using voxel similarity measurements based on a sequential hybrid genetic algorithm, and (2) an automated deformable registration approach based upon a linear elastic finite element formulation. Both methods streamlined the registration process. They are completely automatic and require no user intervention.

The proposed registration strategies were evaluated with numerous 2D and 3D MR images with a variety of tissue structures, orientations and dimensions. Multiple registration pathways were

provided with guidelines for their applications. The sequential genetic algorithm mimics the pathway of an expert manually doing registration. Experiments demonstrated that the sequential genetic algorithm registration provides high alignment accuracy and is reliable for brain tissues. It avoids local minima/maxima traps of conventional optimization techniques, and does not require any preprocessing such as threshold, smoothing, segmentation, or definition of base points or edges.

The elastic model was shown to be highly effective to accurately align areas of interest that are automatically extracted from the images, such as brains. Using a finite element method to get the displacement of each element node by applying a boundary mapping, this method provides an accurate image registration with excellent boundary alignment of each pair of slices and consequently align the entire volume automatically.

This dissertation presented numerous volume alignments. Surface geometries were created directly from the aligned segmented images using the Multiple Material Marching Cubes algorithm. Using the proposed registration strategies, multiple subjects were aligned to a standard MRI reference, which is aligned to a segmented reference atlas. Consequently, multiple subjects are aligned to the segmented atlas and a full fMRI analysis is possible.

Dedicated to my father, Linshui Huang,

in whose footsteps I follow.

ACKNOWLEDGEMENTS

My deepest gratitude goes to my advisor John M. Sullivan, Jr., who has been tirelessly guiding and supporting my work through all the five years with his great patience, intelligence and nonstop encouragement during my whole study.

I thank my parents, with speechless grief and sadness, for their lifelong selfless love, support, and directions. This work could not have been started and finished without them being an excellent model.

I would like to thank Dr. J. King, Prof. R. Ludwig, Prof. A. Hoffman and Prof. Kevin Rong for being my dissertation committee members and offering their professional suggestions.

I would like to thank my lab mates, Murali Murugavel, Praveen Kulkarni and Hamid Ghadyani, for the precious friendship and cooperation they have provided.

My appreciation goes to all my friends who have given me spiritual support and comfort in my life and the strength to finish this work. I appreciate the unlimited love from all my family members in Ohio.

Finally, I thank my husband Stephen Snyder, for his continuous love and spiritual support during the hard times, and the tears and joys we shared together which made life more beautiful.

CONTENTS

LIST OF FIGURES

LIST OF TABLES

1   INTRODUCTION

In recent years medical images are used increasingly in healthcare and medical research. Within healthcare they are used for diagnosis, treatment planning, monitoring disease progression, and other applications. Within medical research (especially neuroscience) they are used to investigate disease processes and understand normal development and ageing. There are numerous medical imaging modalities that delineate anatomy or morphology. These modalities include X-ray, CT (computed tomography), MRI (magnetic resonance imaging), US (ultrasound), portal images, and video sequences obtained by various catheter scopes such as laparoscopy and laryngoscopy, and others. Among all these, MRI is a noninvasive method for producing three-dimensional (3D) tomographic images of an interested part of body. MRI is most often used for the detection of tumors, lesions, and other abnormalities in soft tissues, such as the brain.

1.1   Motivation

Computer-aided techniques are the dominant mode for analyzing and visualizing magnetic resonance images. Many researchers are focused on detecting and quantifying brain abnormalities. In many of these studies, multiple images are acquired from subjects at different times (longitudinal studies) and often with different imaging modalities. These images need to be compared and/or combined to one another or amongst multiple subjects or patients (Figure 1-1), or compared to different modalities (Figure 1-2). Many current clinical practices involve printing the images onto radiographic film and viewing them (side-by-side) on a light box. This comparison strategy requires total user involvement and has significant, serious constraints.

Computerized approaches offer potential benefits, particularly by accurately aligning and quantifying the information in the different images, and providing tools for visualizing the combined images. A critical stage in this process is the alignment or *registration* of the images, which is the main topic of this dissertation (Figure 1-3).
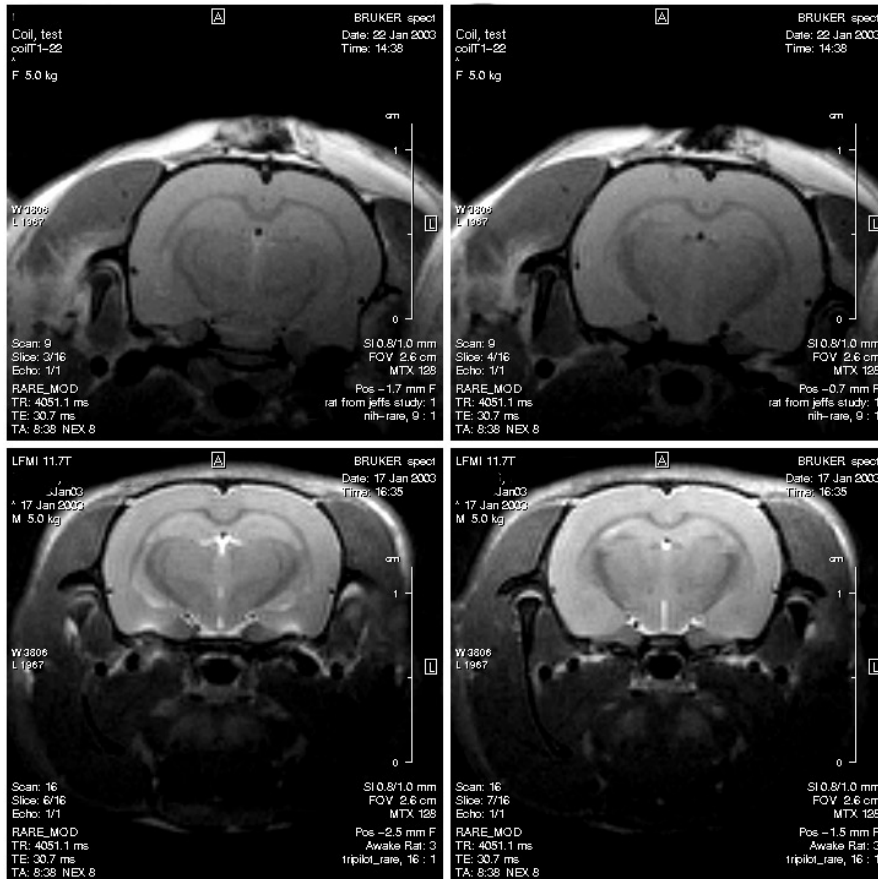
Figure 1-1   High field MRI of rat brains

Top: two MRI slices of rat 1   Bottom: two MRI slices of rat 2

Source: www.insightMRI.com
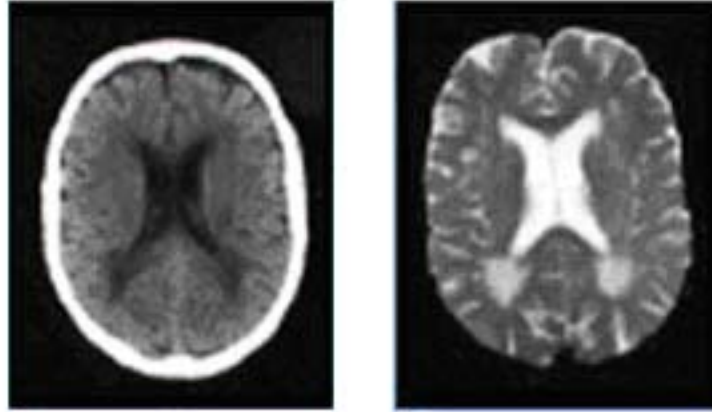
(a) T1 weighted brain MRI   **(b) CT**

Figure 1-2   a T1 weighted Brain MRI and CT

Source: www.medical.siemens.com

The process of registration, which is also referred to as image fusion, superposition, matching or simply alignment, is based on a systematic sequence of operations that transform an image of one modality to another image of the same or different modality. Once spatially aligned comparisons can be made and differences/similarities quantified, the image registration process maps each point in one image onto the corresponding point in the other image.

1.2 Goals

The primary goal of this dissertation is to develop efficient automatic methods for medical image registration. Examples and results are presented using rat brain MRI anatomies obtained through collaborative studies with the University of Massachusetts Medical School, human breast images from our investigations with the Thayer School of Engineering, Dartmouth College, and human brain images from Insight MRI [21]. However, these methods are not restricted to these image sets, neither are they restricted to MR images.
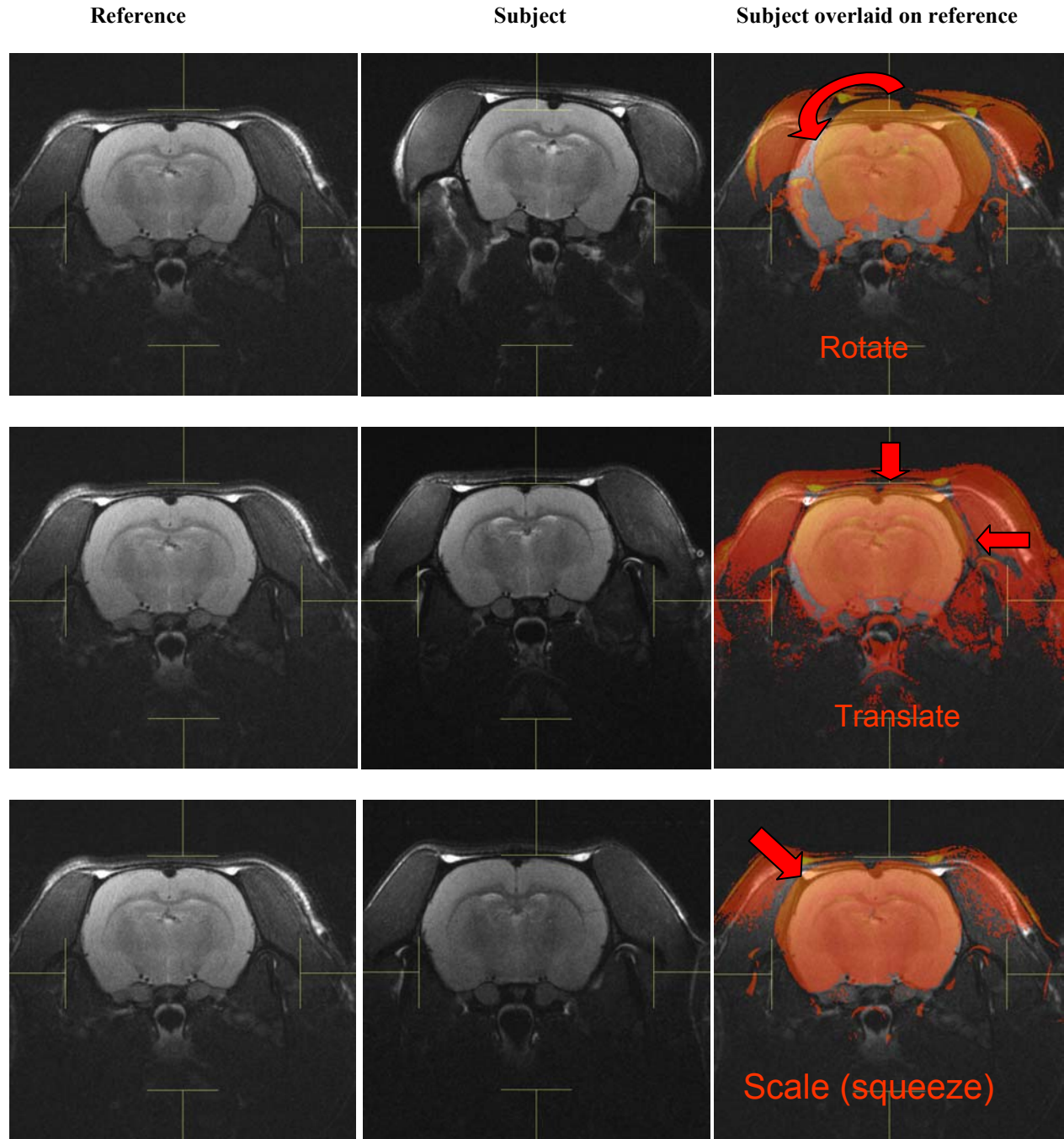
Figure 1-3   A few basic operations for affine image registration

1.3   Methodology

Two major registration methods are introduced in this dissertation.   One is a grayscale registration based on the Genetic Algorithm (GA) methodology.   It can apply numerous rigid body through affine parameter options culminating into a 4x4 homogeneous transformation matrix.   The second strategy uses a nonlinear registration via an elastic finite element model that warps one image onto another.

1.4   Dissertation overview and scope

This dissertation is subdivided into the following chapters:

Chapter 2: Background, includes a full review of the available image registration methods in the area.

Chapter 3: Genetic algorithm for registration, describes a set of registration algorithms based on the optimization of a similarity measurement, using genetic algorithm.

Chapter 4: Linear elastic model, describes a contour-based linear elastic registration using a finite element model.

Chapter 5: Addresses strategies to align 3D volume sets.

Chapter 6: Presents numerous results for 2D and 3D registrations.

Chapter 7: Concludes the dissertation by summarizing the work and suggests future work in relation to observed results.

2 BACKGROUND

Researchers need accurate information obtained from different radiological images for diagnosis, treatment and basic science. The most widely used application of medical image registration is aligning tomographic images, which are two dimensional slices obtained from three-dimensional space by blurring out the images from other planes. Applications of image registration include combining images of the same subject from different modalities, aligning temporal sequences of images to compensate for motion of the subject between scans, image guidance during interventions and aligning images from multiple subjects in cohort studies. In many cases, current registration algorithms can automatically register images via rigid body transformations if tissue deformation is not an issue. Numerous non-rigid registration algorithms exist that can compensate for tissue deformation, or align images from different subjects, albeit not automatically. Substantial progress in automatic or semi-automatic non-rigid and/or elastic registration algorithms have occurred in the last decade [5][11]. However, many registration problems remain unsolved, such as accuracy of alignment [33] [38] [39] [43][48][49][61], level of automation [36][52][55][70], computational expenses [27][29], and the tradeoff among these factors [42][44][72], etc. Therefore, medical image registration continues to be an active field of research.

This chapter reviews research that has been done in this area and current registration techniques that have been practically applied. It discusses on some of the most widely used and most

recently published registration algorithms, and afterwards introduces the necessity of the work of this dissertation.

2.1 Medical images

The term "medical image" covers a wide variety of images, with very different underlying physical principles, and very different applications. In this dissertation we primarily consider the main radiological imaging modalities. These include traditional projection radiographs, with or without contrast and subtraction, nuclear medicine projection images, ultrasound images and the cross-sectional modalities of x-ray, computed tomography (CT), magnetic resonance imaging (MRI), single photon emission computed tomography (SPECT) and positron emission tomography (PET) [147]. The last four modalities (CT, MRI, SPECT, PET) are referred as the tomographic modalities. Tomographic modalities are the easiest modalities from the point of view of image registration, because they provide voxel datasets in which the sampling is normally uniform along each axis, though the voxels themselves tend to have anisotropic resolution.[5]

2.1.1 X-ray

X-rays are the oldest and most frequently used form of medical imaging. In an X-ray system, X-rays impinging on the image intensifier are transformed into a distribution of electrons, which produces an amplified light image on a smaller fluorescent screen after acceleration [143][144][145]. The image is observed by a television camera and a film camera and can be stored and viewed on a computer screen (Figure 2-1).
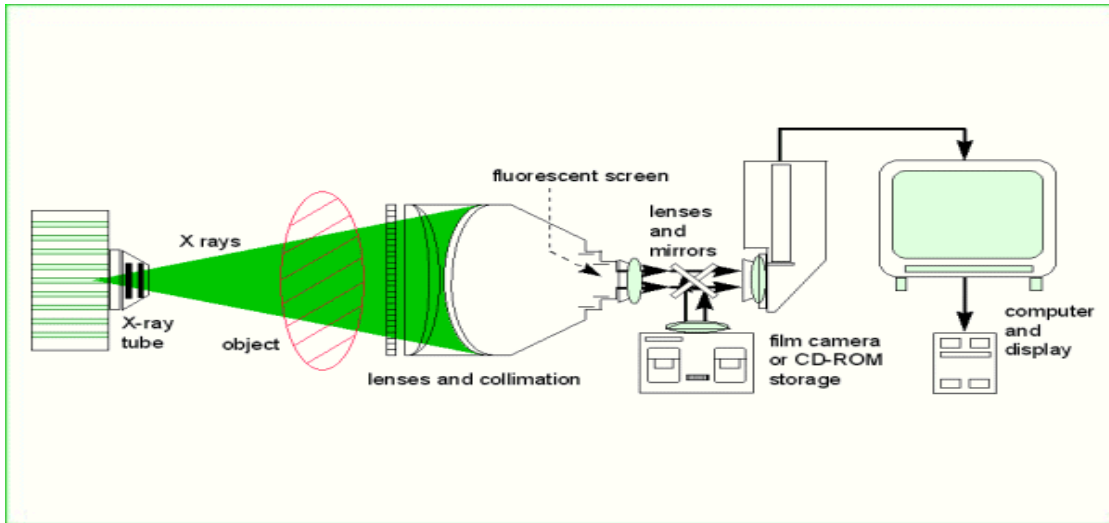
Figure 2-1   X-Ray system [146]

X-ray technologies include planar X-ray such as mammography and chest X-ray (Figure 2-2, 2-3), and computerized tomography (CAT scan or CT). Computerized Tomography (CT) was first invented by Dr. G. N. Housfield in 1971. It produces an image of a cross sectional slice of the body using X-rays technology.   The method constructs images from large number of measurements of rotated X-ray transmission through the patient. (Figure 2-4, 2-5)
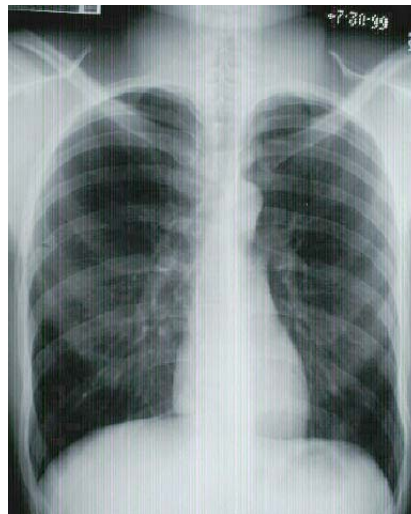
Figure 2-2   Chest X-ray image
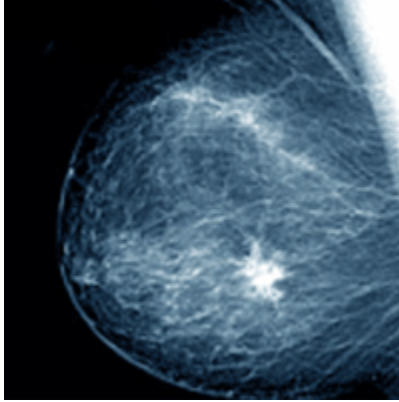
Figure 2-3   Mammography

www.gsmc.org/images/ imaging/imaging_mam1.gif
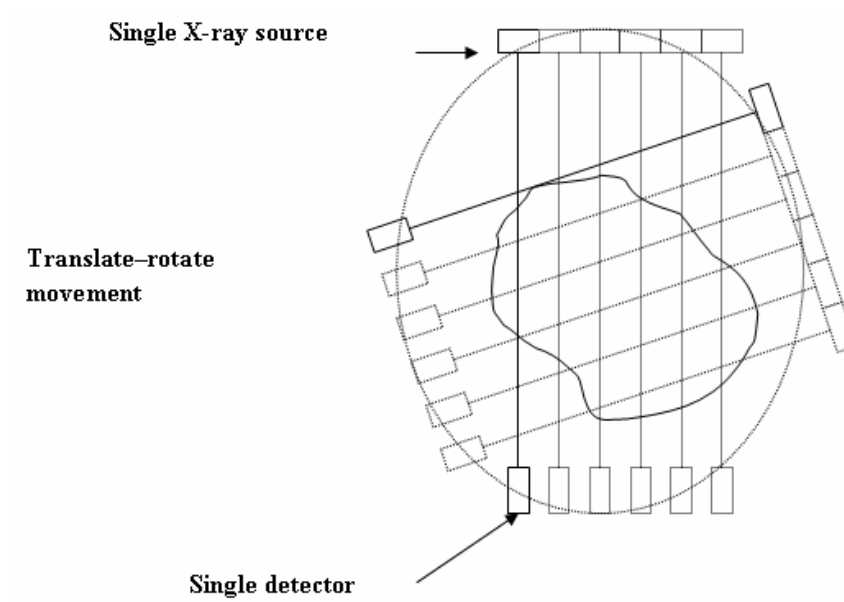
Figure 2-4   First generation CT with rotating x-ray source and detectors [146]
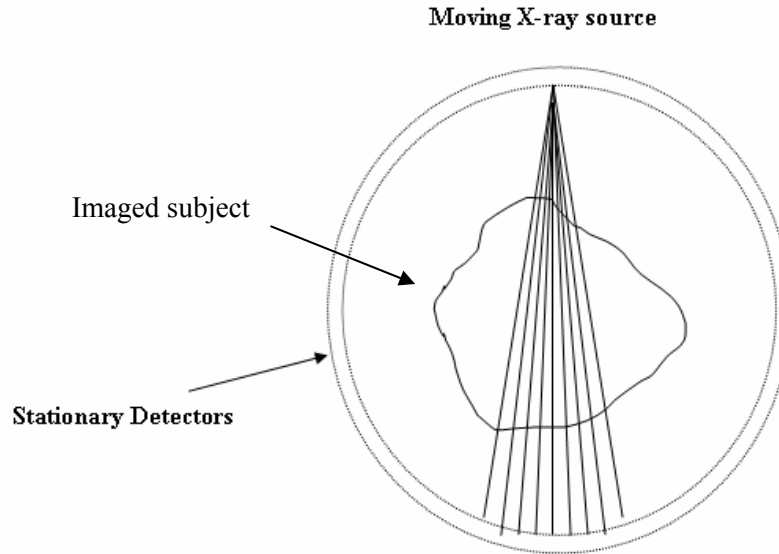
Figure 2-5   5th generation CT with fan beam and stationary detectors [146]

2.1.2   Nuclear imaging

Nuclear imaging is a use of Γ (gamma) rays, radionuclides and radiopharmaceuticals in the medical imaging field [146]. Nuclear imaging looks at physiological processes rather than at anatomical structures. In nuclear imaging, short-lived radiopharmaceuticals (radioactive drugs that emit gamma rays and that are attracted to the organ of interest) are injected into a patient's bloodstream (in amounts of picomolar concentrations thus not having any effect on the process being studied) [147]. The half life of these materials is between few minutes to weeks. The time course of the process being studied and the radiation dose to the target are considered. The nuclear camera then, in effect, takes a time-exposure "photograph" of the pharmaceutical as it enters and concentrates in these tissues or organs. By tracing this blood flow activity, the resulting nuclear medicine image tells physicians about the biological activity of the organ or the vascular system that nourishes it. Nuclear imaging has a wide variety of uses, including the diagnosis of cancer, studying heart disease, circulatory problems, detecting kidney malfunction,

and other abnormalities in veins, tissues and organs. Technologies include planar imaging (e.g.
bone scan), positron emission tomography (PET) and single photon emission computed
tomography (SPECT) [144][146]. (Figure 2-6)
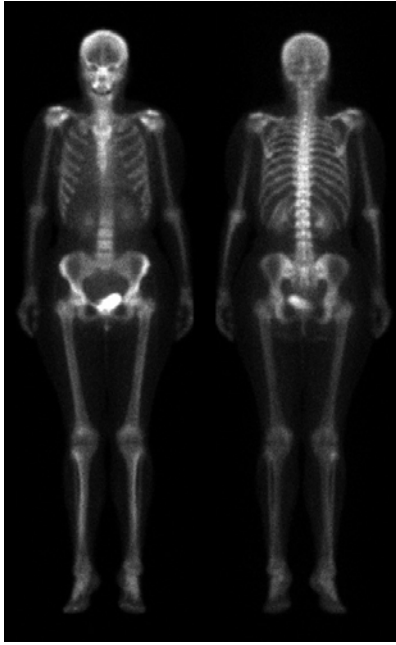
Figure 2-6   Whole body nuclear image [146]

2.1.3   Magnetic resonance images (MRI)

Magnetic resonance imaging (MRI) was first described as an imaging technique in 1973 by Paul
Lauterbur [134] . Compared to a CT scanner which uses X-rays, a type of ionizing radiation to
acquire its images, MRI uses non-ionizing radio frequency signals to acquire its images. It is a
non-invasive method used to render images of the inside of an object. Unlike CT, which uses
only X-ray attenuation to generate image contrast, MRI has a long list of properties that can be
used to generate image contrast. By variation of scanning parameters, tissue contrast can be
altered and enhanced in various ways to detect different features.   MRI can generate cross-
sectional images in any plane (including oblique planes) (Figure 2-7) [144][147].

11
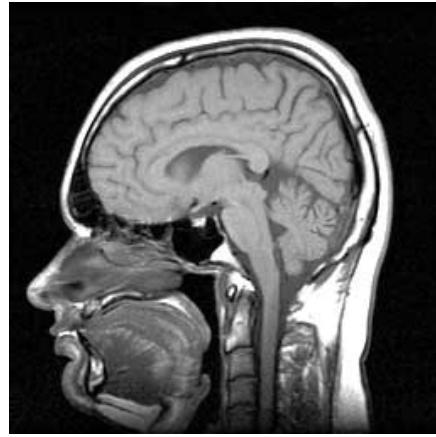
(a)   (b)

Figure 2-7   Magnetic resonance imaging

(a) a MRI machine; (b) a MR image showing a vertical (sagittal) cross section through a human head

http://en.wikipedia.org/wiki/Magnetic_resonance_imaging

In the MRI procedure, radiofrequency waves are directed at protons, the nuclei of hydrogen atoms, in a strong magnetic field. The protons are first "excited" and then "relaxed," emitting radio signals that can be computer-processed to form an image. In the body, protons are most abundant in the hydrogen atoms of water – the "H" of H_2O – so that an MR image shows differences in the water content and distribution in various body tissues. Even different types of tissue within the same organ, such as the gray and white matter of the brain, can easily be distinguished. [3]

The slice selection is accomplished by varying the gradient of the magnetic field as a function of position. This causes the linear variation of the proton resonance frequency along with the

position. The MR imaging system uses the frequency encoding and phase encoding to determine the position of each signal within the patient [146].

2.1.4   Functional MRI (fMRI)

fMRI is a technique that measures signal changes in the brain that are due to changing neural activity [134]. The brain is scanned at low resolution but at a rapid rate. Increases in neural activity cause changes in the MR signal via T2* changes. This mechanism is referred to as the BOLD (blood-oxygen-level dependent) effect (Figure 2-8) [144][146][147].
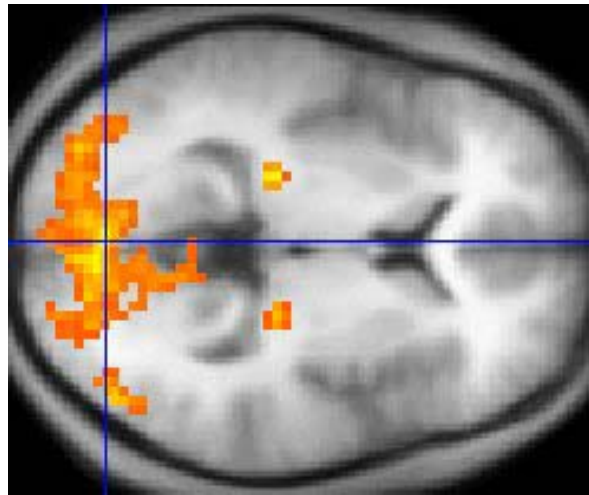
Figure 2-8   fMRI data showing brain regions of activation

http://en.wikipedia.org/wiki/Image:FMRI.jpg

2.1.5   Ultrasound imaging

Ultrasound operates much the same as sonar, using high-frequency sound waves as its imaging source. Ultrasound is the reflection of a sound wave as it collides with the anatomy being studied. The resulting pattern of that reflection is converted into diagnostic information via a hand-held transducer passed over the area being imaged [146].

This medical technology's non-radioactive nature has made it the modality of choice for ob-gyn procedures. In fact, it is most commonly associated with fetal imaging (Figure 2-9). Advances in ultrasound technology have resulted in applications that extend far beyond fetal imaging to include cardiac, vascular and breast imaging, as well as cyst identification and guidance of a variety of surgical and other therapeutic procedures [146].

Ultrasound is also used for other applications such as measurement of blood flow in the blood vessels, etc.

Figure 2-9   Fetus ultrasound

Source: http://www.tcmedcenter.com/portal/tabid__6926/Default.aspx

2.2 Image registration

In principle, medical image registration could involve bringing all the information from a given patient, whatever the form, together into a single representation of the individual that acts like a multimedia electronic patient record with implicit information about the spatial and temporal relationship between all the image information [1]. Various data mining strategies and structural characterizations are trying to reach this ideal target [148] [149] [150] [151] [152]. However, the huge variety of spatial and temporal resolutions and fields of view of the different images makes this difficult, and the clinical benefit of such an approach has not yet been demonstrated. No system exists yet that can simply align any two image volumes based on grayscale pixel information robustly and automatically.

2.2.1 Registration methods

There are four general approaches to image registration or alignment problems: manual registration, control-point based registration, edge-based registration, and voxel property based registration.[2][5]

2.2.1.1 Manual registration

The user performs all the alignment work usually with an interactive graphics interface with visual feedback. The accuracy of registration depends on the user's judgment to match corresponding anatomical features. Registration efficiency (or speed) is mostly based on user's experience. Table 2-1 shows the manual registration time it took to register two 256x256x12 rat brain MRI volume sets for two skilled users in performing registration and three technically

qualified users. Different users can have different results and the time requirement can vary significantly.

Table 2-1   3D manual registration time comparison

SU: Skilled user (expert)   QU: Qualified user

	SU 1	SU 2	QU 1	QU 2	QU 3
Time	3 min	5 min	32 min	25 min	20 min

2.2.1.2   Control-point based registration

This strategy, also called landmark based registration, is used frequently to find rigid or affine transformations. In landmark based registration, several landmarks (control points) are usually identified interactively by the user. These landmarks can be anatomical, i.e., salient and accurately locatable points of the morphology of the visible anatomy, or geometrical, i.e., points at the locus of the optimum of some geometric property, e.g., local curvature extrema, corners, etc [33][34][35][36][39][40]. The set of identified points is sparse compared to the original image content, which makes for relatively fast optimization procedures (Figure 2-10).
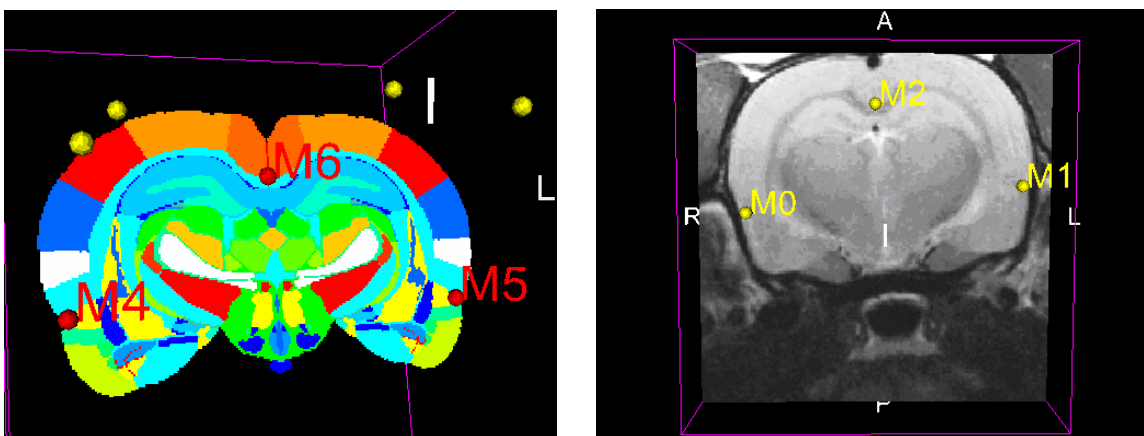
Figure 2-10   Landmarks on Atlas (M4, M5, M6) and subject image (M0, M1, M2)

Landmark based methods are mostly used to find rigid or affine transformations. Anatomical landmarks are also often used in combination with a different registration basis [37][38]: methods that rely on optimization of a parameter space that is not quasiconvex are prone to sometimes get stuck in local optima, possibly resulting in a large mismatch. By constraining the search space according to anatomical landmarks, such mismatches are reduced. Moreover, the search procedure can be sped up considerably. The drawback of a landmark based registration is that user interaction is usually required for the identification of the landmarks.

2.2.1.3   Edge based registration

Edge based registration, also called segmentation based registration, is to extract (segment) anatomical structures from both images and use the segmented images as input for the alignment procedure. Segmentation based registration can be rigid model based or deformable model based [5].

Rigid body model based approaches became popular due to the success of the "head-hat" method introduced by Pelizzari and co-workers [41][42][43], which relies on the segmentation of the skin surface from CT, MR and PET images of the head. A drawback of segmentation based methods is that the registration accuracy is limited to the accuracy of the segmentation step. In theory, segmentation based registration is applicable to images of many areas of the body, yet in practice the application areas have largely been limited to neuroimaging and orthopedic imaging. The methods are commonly automated but the segmentation step is usually performed semi-automatically.

The optimization criterion of deformable model based approaches is different [44][45][46]. It is always locally defined and computed, and the deformation is constrained by elastic modeling constraints imposed onto the segmented curve or surface. The deformation process is always done iteratively, small deformations at a time. Deformable model approaches are based on a template model that needs to be defined in one image. After this, two types of approaches can be identified: the template is either deformed to match a segmented structure in the second image, or the second image is used unsegmented. Opposed to registration based on extracted rigid models, which is mainly suited for intrasubject registration, deformable models are in theory very well suited for intersubject and atlas registration, as well as for registration of a template obtained from a patient to a mathematically defined general model of the templated anatomy (Figure 2-11). A drawback of deformable models is that they often need a good initial position in order to properly converge, which is generally realized by (rigid) pre-registration of the images involved. Another disadvantage is that the local deformation of the template can be unpredictably erratic if the target structure differs sufficiently from the template structure.

(a) Initial alignment   (b) Registered based on a deformable model
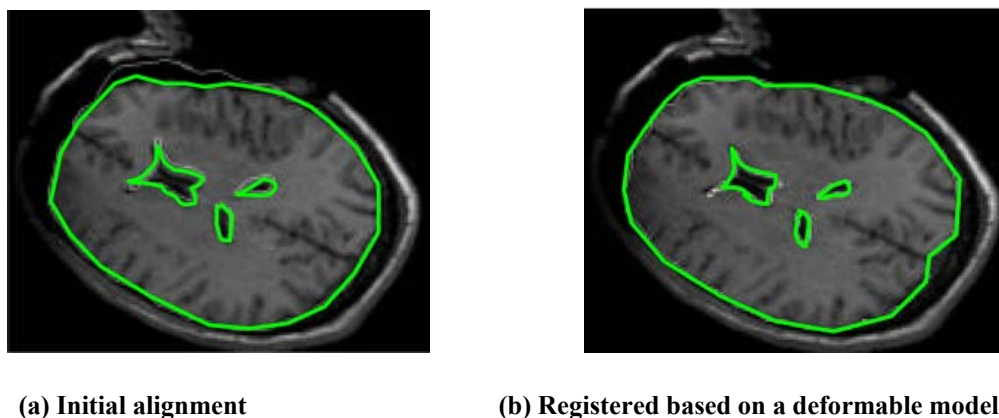
Figure 2-11   Axial cut through surfaces overlaid on corresponding MR slice [45]

2.2.1.4 Voxel property based registration

These methods operate directly on the gray-scale images, without prior data reduction by the user or segmentation, also called optimization of a similarity measurement [47] [48] [49] [51] [52] [55]. Genetic algorithm [8] [9] is one of the typical algorithms used for voxel property based registration, which is presented in detail in chapter 3. Mutual information is also a popular approach [52][61][62]. Theoretically these are the most flexible registration methods since they do not start with reducing the grayscale valued image to relatively sparse extracted information, but use all of the available information throughout the registration process. However, these methods have been limited in use of 3D/3D registration by the considerable computational costs [50] [53] [54].

2.2.2   Transformation models

Based on transformation models, registration methods are classified into two main categories: 1. rigid body and affine transformation; 2. deformable transformation.

2.2.2.1 Rigid body and affine transformation

Rigid body and affine transformations overlay one image volume onto another via a 4x4 homogeneous transformation matrix [25] [153].

Translation matrix Tr describes the displacements $[T_x \quad T_y \quad T_z]$ in x, y, and z directions:

$$Tr = \begin{bmatrix} 1 & 0 & 0 & T_x \\ 0 & 1 & 0 & T_y \\ 0 & 0 & 1 & T_z \\ 0 & 0 & 0 & 1 \end{bmatrix}$$
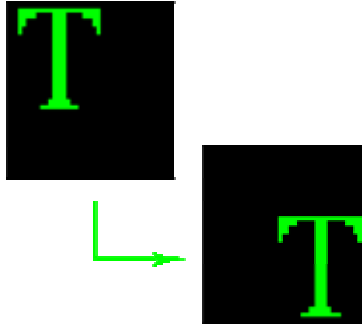
Figure 2-12   Image translation [153]

Rotation matrix R_y describes the rotation about y axis (roll):

$$R_y = \begin{bmatrix} \cos\beta & 0 & -\sin\beta & 0 \\ 0 & 1 & 0 & 0 \\ \sin\beta & 0 & \cos\beta & 0 \\ 0 & 0 & 0 & 1 \end{bmatrix}$$

Rotation matrix R_x describes the rotation about x axis (pitch):

$$R_x = \begin{bmatrix} 1 & 0 & 0 & 0 \\ 0 & \cos\gamma & \sin\gamma & 1 \\ 0 & -\sin\gamma & \cos\gamma & 1 \\ 0 & 0 & 0 & 1 \end{bmatrix}$$

Rotation matrix R_z describes the rotation about z axis (yaw):

$$R_z = \begin{bmatrix} \cos\theta & \sin\theta & 0 & 0 \\ -\sin\theta & \cos\theta & 0 & 0 \\ 0 & 0 & 1 & 0 \\ 0 & 0 & 0 & 1 \end{bmatrix}$$

Scaling matrix S describes the scaling ratios about the origin in x, y, z directions:

$$S = \begin{bmatrix} S_x & 0 & 0 & 0 \\ 0 & S_y & 0 & 0 \\ 0 & 0 & S_z & 0 \\ 0 & 0 & 0 & 1 \end{bmatrix}$$
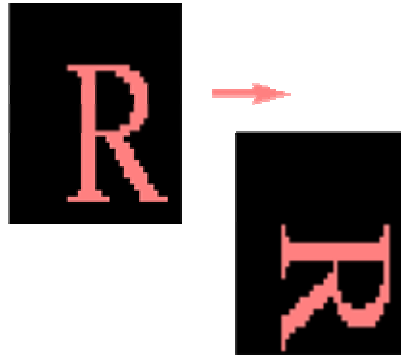
Figure 2-13   Image rotation [153]
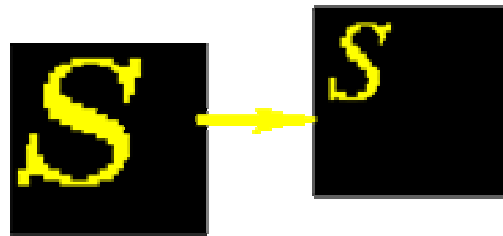
Figure 2-14   Image scaling [153]

The overall transformation matrix for affine model is the product of translations, rotations and scalings:

$$T = Tr \cdot R_y \cdot R_x \cdot R_z \cdot S$$

$$T = \begin{bmatrix} S_x \cos\theta\cos\beta & -S_y \sin\theta\cos\beta & S_z \sin\beta & T_x \\ S_x(\cos\theta\sin\beta\sin\gamma+\sin\theta\cos\gamma) & S_y(\cos\theta\cos\gamma-\sin\theta\sin\beta\sin\gamma) & -S_z \cos\beta\sin\gamma & T_y \\ S_x(\sin\theta\sin\gamma-\cos\theta\sin\beta\cos\gamma) & S_y(\sin\theta\sin\beta\cos\gamma+\sin\gamma\cos\theta) & S_z \cos\beta\cos\gamma & T_z \\ 0 & 0 & 0 & 1 \end{bmatrix}$$

Eq. 2-1
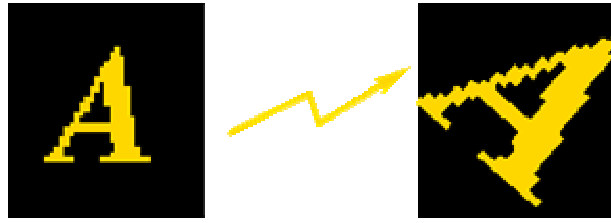
Figure 2-15   Affine transformation [153]

2.2.2.2   Deformable transformation

Deformable (non-affine) transformation algorithms normally either include an initial rigid body or affine transformation [55], or are run based on a surface to surface mapping (segmentation) [44][46][56]. When point landmarks are available, thin-plate splines are often used to determine the transformation.   Using intensity-based algorithms, the non-rigid component of the transformation can be determined using a linear combination of polynomial terms [57] [58] or B-spline surfaces defined by a regular grid of control points [11][60].   An effective method for deformable transformation is the finite element method (FEM) [45] [63] [64] [65], which will be discussed in greater detail in chapter 4.   It is also possible to mix rigid and non-rigid transformations in the same image [59].

2.2.3   Error evaluation

For all types of image registration, the assessment of registration accuracy is very important. The required accuracy will vary between applications, but for all applications it is desirable to know both the expected accuracy of a technique and also the registration accuracy achieved on each individual set of images. For one type of registration algorithm, point-landmark registration, the error propagation is well understood.   For other approaches, however, the algorithms

themselves provide no useful indication of accuracy. The current approach to ensuring acceptable accuracy is visual assessment of the registered images before they are used for the desired clinical or research application. For full-image content based voxel property registration methods, the following paradigms are used in the literature: [2][4]

2.2.3.1   Minimizing intensity difference

One of the simplest voxel similarity measures is the least square method, i.e., the sum of squared intensity differences between images, SSD, which is minimized during registration. For N voxels in $\Omega_{A,B}^{T}$, the overlap domain of images A and B for a given transformation estimate T,

$$SSD = \frac{1}{N} \sum_{x_A \in \Omega_{A,B}^{T}} \left| A(x_A) - B^T(x_A) \right|^2$$

where $B^T(x_A)$ is image B transformed into the coordinate space of A. The SSD measure is widely used for intramodality MR registration. It is very sensitive to a small number of voxels that have very large intensity differences between images A and B. This sensitivity can be reduced by using the sum of absolute differences, SAD:

$$SAD = \frac{1}{N} \sum_{x_A \in \Omega_{A,B}^{T}} \left| A(x_A) - B^T(x_A) \right|$$

2.2.3.2   Correlation techniques

The SSD measure makes the implicit assumption that after registration, the images differ only by Gaussian noise. A less strict assumption would be that, at registration, there is a linear relationship between the intensity values in the images. In this case, the optimum similarity measure is the correlation coefficient:

$$CC = \frac{\sum_{x_A \in \Omega_{A,B}^T} (A(x_A) - \overline{A})(B^T(x_A) - \overline{B})}{\{\sum_{x_A \in \Omega_{A,B}^T} (A(x_A) - \overline{A})^2 \sum_{x_A \in \Omega_{A,B}^T} (B^T(x_A) - \overline{B})^2\}^{1/2}}$$

Where $\overline{A}$ is the mean voxel value in image $A|_{\Omega_{A,B}^T}$ and $\overline{B}$ is the mean of $B^T|_{\Omega_{A,B}^T}$. This similarity measure has been used for intramodality registration [66]. The correlation coefficient can be thought of as a normalized version of the widely used cross correlation measure:

$$C = \sum_{x_A \in \Omega_{A,B}^T} A(x_A) B^T(x_A)$$

2.2.3.3 Minimization of ratio image uniformity

The ratio image uniformity (RIU) algorithm was originally introduced by Woods et al [67] for the registration of serial PET studies, but has been widely used more recently for serial MR registration, and is available in the AIR registration package from UCLA. The RIU algorithm is most easily thought of in terms of an intermediate ratio image R comprising N voxels within $\Omega_{A,B}^T$ ($N = \sum_{\Omega_{A,B}^T} 1$):

$$R(x_A) = \frac{A|_{\Omega_{A,B}^T}(x_A)}{B^T|_{\Omega_{A,B}^T}(x_A)} \qquad \overline{R} = \frac{1}{N} \sum_{x_A \in \Omega_{A,B}^T} R(x_A)$$

$$RIU = \frac{\sqrt{\frac{1}{N} \sum_{x_A \in \Omega_{A,B}^T} (R(x_A) - \overline{R})^2}}{\overline{R}}$$

2.2.3.4 Maximization of zero crossings in difference image

A difference image is a calculated image based on the voxel difference of two images (Figure 2-16). Difference images are widely used to compare intermodality images and evaluate the quality of deformable registration [11][68][69].

(a)   (b)   (c)

(d)   (e)
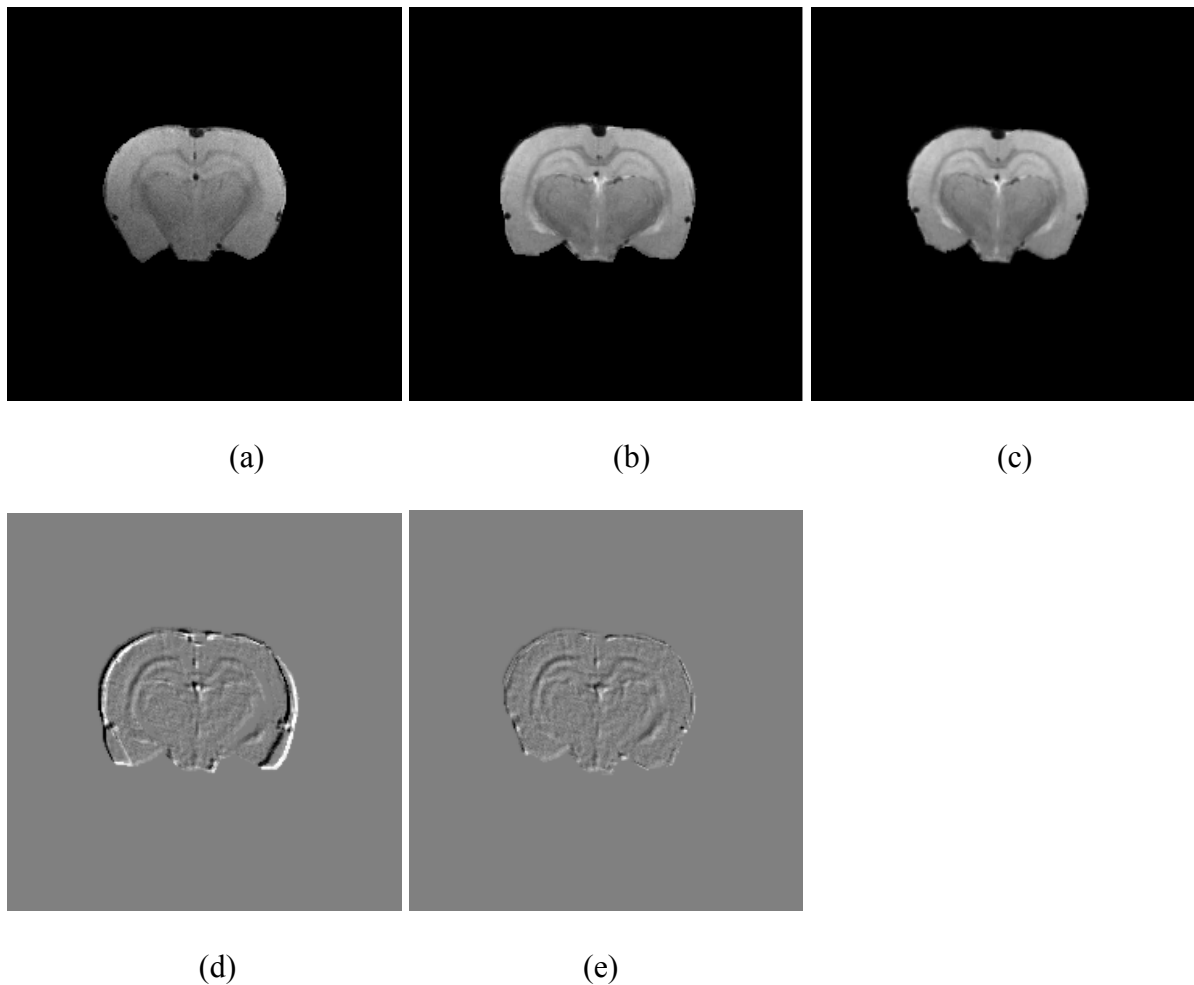
Figure 2-16   Difference Image [154]

(a) Reference   (b) Subject   (c) Subject registered to reference space (d) Difference   image   before registration   (e) Difference after registration

There are numerous other strategies to minimize registration error, such as histogram clustering and minimization of histogram dispersion [70][71][72][73][74], and maximization of mutual information (relative entropy) of the histogram [75], etc.

In this dissertation we use the intensity difference to quantify the registration error, because it is simple and reliable. Difference images are also used to help visualizing the elastic registration error.

2.3 Proposed registration strategies

In this dissertation we provide two 3D image registration strategies. 1) Genetic algorithm based registration which measures the voxel similarity of two volume sets, and 2) A nonlinear registration using a finite element model for elasticity based on the governing partial differential equations for plane stress.

2.3.1 Genetic algorithm

Genetic algorithms (GAs) have been used to achieve automatic, accurate, and robust image registrations [10][18][28][52]. However, researchers have pointed out that GAs are intrinsically computational expensive. Different approaches have been tried to decrease the cost [27][29][53][80]. In this dissertation we present a sequential registration method to increase its efficiency.

2.3.2   Elastic model

There are numerous elastic registration methods proposed [44][45][46][88][89]. Unlike rigid body transformations that keep the shape of an object, elastic models can map straight lines into curves therefore slightly change the shape of a subject. Therefore, elastic transformation can correct deformations caused by sampling process or imaging techniques. We present an elastic transformation of automatically cropped images. It uses finite element method (FEM) [44][45] to implement registration by applying a boundary mapping [83].

3   GENETIC ALGORITHM FOR REGISTRATION

3.1   Introduction

A genetic algorithm (GA) is a search technique used in computing to find true or approximate solutions to optimization and search problems. Genetic algorithms were formally introduced in the United States in the 1970s by John Holland at University of Michigan. In particular, genetic algorithms work very well on mixed (continuous and discrete), combinatorial problems. They are less susceptible to getting "stuck" at local optima than gradient search methods. But they tend to be computationally expensive. [8][9][14][15]

To use a genetic algorithm, the solution to the problem is represented as a set of chromosomes. The genetic algorithm creates a population of solutions, frequently arbitrary, and applies genetic operators such as mutation and crossover to evolve the solutions in order to find better ones.[10][18]

The advantage of the GA approach is the ease with which it can handle arbitrary kinds of constraints and objectives. All such things can be handled as weighted components of the fitness function, making it easy to adapt the GA scheduler to the particular requirements of a very wide range of possible overall objectives.

3.2   Genetic algorithm

Based on the principle of Darwinian natural selection, there are three basic biological operators on the population:

3.2.1   Selection

Selection is the stage of GA to select the individuals from the population for reproduction. The principle of selection is based on the fitness of individual. The individual genomes with higher fitness values are chosen from a population for later reproduction.

There are several generic selection algorithms. Certain selection methods rate the fitness of each solution and preferentially select the best solutions. However, if the fitness evaluation is time consuming some GA strategies rate only a random sample of the population. A typical algorithm can be implemented as follows:

1. The fitness function is evaluated for each individual, providing fitness values;
2. The population is sorted by descending fitness values;
3. Select the individuals with a fitness value that is higher than a given constant, or select a certain number (or percentage) of individuals that have higher fitness values.

3.2.2   Crossover

Crossover is one of the two main operators at the reproduction stage of a genetic algorithm. It is an analogy to biological crossover, by exchanging some chromosomes of parents at the crossover point to generate new individuals.

Numerous strategies exist for the crossover procedure. Figure 3-1 depicts a few options.

| a) one point crossover | b) two point crossover | c) "cut and splice" |
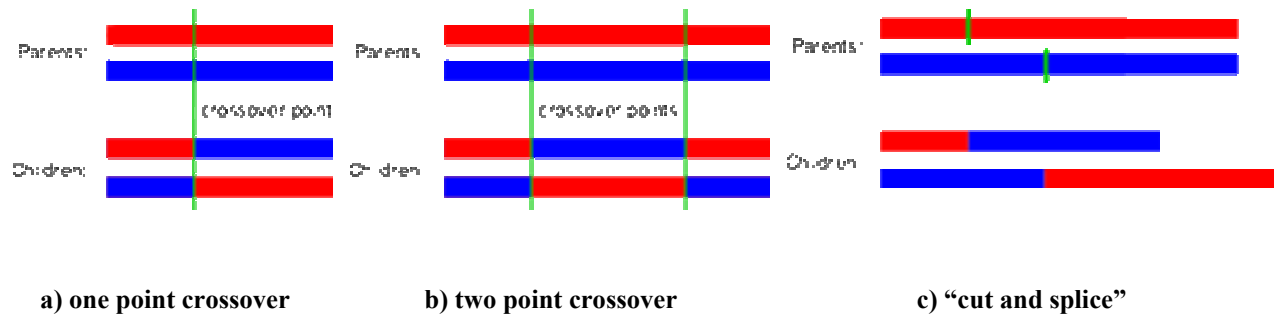
Figure 3-1   Crossover techniques

One point crossover: A crossover point on the parent organism string is selected. All data beyond that point in the organism string is swapped between the two parent organisms. [108]

Two point crossover: Two point crossover calls for two points to be selected on the parent organism strings. Everything between the two points is swapped between the parent organisms, rendering two child organisms. [105]

"Cut and splice" crossover: "Cut and splice" approach results in a change in length of the children strings. The reason for this difference is that each parent string has a separate choice of crossover point. [109]

Uniform crossover: A crossover that decides (with some probability – known as the mixing ratio) which parent will contribute each of the gene values in the offspring chromosomes. This

allows the parent chromosomes to be mixed at the gene level rather than the segment level (as with one and two point crossover) [106][107][112][113]. For some problems, this additional flexibility outweighs the disadvantage of destroying building blocks.

Consider the following two parents which have been selected for crossover:

Parent 1:   1 1 0 0 1 0 1 0

Parent 2:   0 0 1 0 0 1 1 1

If the mixing ratio is 0.5, approximately half of the genes in the offspring will come from parent 1 and the other half will come from parent 2. Below is a possible offspring after uniform crossover, subscripts indicating which parent each gene is from:

Child 1: 1_1 0_2 1_2 0_1 0_2 0_1 1_1 1_2

Child 2: 0_2 1_1 0_1 0_2 1_1 1_2 1_2 0_1

Arithmetic crossover: A crossover operator that linearly combines two parent chromosome vectors to produce two new offspring according to the following equations [53][54]:

$$\text{Offspring1} = a * \text{parent1} + (1-a) * \text{parent2}$$

$$\text{Offspring2} = (1-a) * \text{parent1} + a * \text{parent2}$$

Eq. 3-1

where "a" is a random weighting factor (chosen before each crossover operation).

Consider the following two parents (each consisting of four float genes) which have been selected for crossover:

Parent1:   (30) (20) (5) (7.4)

Parent2:   (35) (15) (3) (5.6)

If a=0.3, then the following two offspring would be produced:

Offspring1:   (33.5) (16.5) (3.6) (6.14)

Offspring2:   (31.5) (18.5) (4.4) (6.86)

Heuristic crossover: A crossover operator that uses the fitness values of the two parent chromosomes to determine the direction of the search [110][111]. The offspring are created according to the following equations:

Offspring1 = BestParent + r*(BestParent – WorstParent)

Offspring2 = BestParent

where r is a random number between 0 and 1.

It is possible that Offspring1 will not be feasible. This can happen if r is chosen such that one or more of its genes fall outside of the allowable upper or lower bounds. For this reason, heuristic crossover has a user settable parameter (n) for the number of times to try and find an r value that results in a feasible chromosome. If a feasible chromosome is not produced after n tries, the WorstParent is returned as Offspring1 [111].

3.2.3 Mutation

Mutation is the other main operator at the reproduction stage of a genetic algorithm, used to maintain genetic diversity as the generations evolve [134]. It is analogous to biological mutation. The classic example of a mutation operator involves a probability that an arbitrary chromosome changes from its original state during formation of the new individual. This probability should usually be set fairly low. If it is set to high, the search will turn into a primitive random search. The mutation rate is independent of the size of the population. Some literature says 0.01 is a good first choice for mutation rate [114], while more suggest 1/n (n is the number of chromosomes of an individual) produces good results 0. Most systems are not sensitive to reasonable changes in mutation rate, therefore an increase in the mutation rate gives only an insignificant acceleration of the search [160][161]. What is critical is that the mutation exists in the process and it is not applied at high frequency.

The purpose of mutation in GAs is to allow the algorithm to avoid local minima by preventing the population of chromosomes from becoming too similar to (or cloning) each other, thus slowing or even stopping evolution. This reasoning also explains the fact that most GA systems avoid only taking the fittest of the population in generating the next but rather a random (or semi-random) selection with a weighting toward those that are fitter.

3.2.4 Fitness function

In the process of GA selection, a fitness function that quantifies the optimality of a solution (a genome) is used to rank all the population. Optimal genomes are allowed to breed, producing a new generation that will hopefully improve the fitness level.

An ideal fitness function correlates closely with the algorithm's goal, and is computed quickly. Speed of execution is very important, as a typical genetic algorithm must be iterated many, many times in order to produce a useable result for a non-trivial problem.

3.2.5 Why GA

GAs are computational models of natural evolution in which stronger individuals are more likely to be the winners in a competitive environment. Besides their intrinsic parallelism, GAs are simple and efficient for optimization and search.

The main advantage of the GA approach for image registration is that pre-alignment between images is not necessary to guarantee a good result. However, GA is a stochastic method and generally time-consuming [156].

GAs have been applied to image registration problems before [10][18][28][52][157], and recently some range image registration algorithms based on GA were proposed [27] [156] [158], in order to improve performance or to decrease the computational cost. We present in this chapter a GA that works for 3D image registration more efficiently in a few aspects: 1) it avoids parents cloning; 2) instead of discarding all parents, our algorithm includes the better parents in ranking the offspring, to achieve a better result; 3) instead of applying all chromosomes for different degrees of freedom at the same time, our GA algorithm is sequentially applied [53][54], thus saves the computational time significantly. The sequential process of GA registration imitates the pathway of a manual image alignment performed by a professional – in-plane

shifting and rotation in the axial orientation followed by out-of-plane adjustments and maybe a small amount of scaling. Building these attributes into the GA registration provides a much improved system.

The three most important aspects of using genetic algorithms are: (1) definition of the objective function, (2) definition and implementation of the genetic representation, and (3) definition and implementation of the genetic operators. Beyond these basic definitions, different variations could be applied to improve performance[155][156], find multiple optima[10][18][105], or parallelize the algorithms[27][29][158]. Once these three components have been defined, the genetic algorithm is reasonably complete.
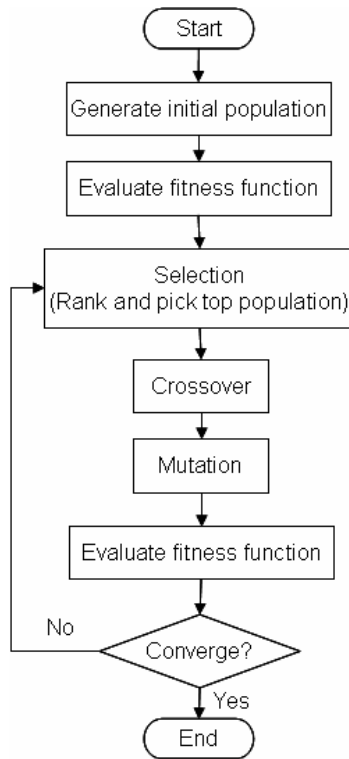
Figure 3-2   Flowchart of genetic algorithm

Figure 3-2 shows the general workflow of a genetic algorithm, which is described as follows:

1.   Generate an initial population.   For our system a random population of individuals is created among the multi-dimensional search space;

2.   Evaluate the fitness of initial population.   Sum of absolute difference (SAD) pixel intensities was selected as the fitness function (cost function) for our registration process;

3.   Repeat the following natural selection operation until the termination measure is satisfied:

   (a) the selection process identifies individuals as the parents based on their fitness to participate in the reproduction;

   (b) the selected parents' chromosomes are intermixed (crossover) to create new individuals;

   (c) the mutation factor, albeit infrequent, is applied at this stage to an offspring;

   (d) evaluate the fitness of current population including the parents and new individuals, and update the population based on the fitness while preserving the size of population;

   (e) once the termination criteria are satisfied (program converged), the best individual evolved from the population is selected. If not, return to step (a) and repeat the process.

3.3   Implementation

This section presents the implementation of GA for registration used to register MR images. The MR images have come from five sources: a) rat brain images using a fast-spin echo on a 4.7T Bruker magnet system from the University of Massachusetts Medical School, b) breast images using a 1.5T GE Magnet, c) a reference human brain image with high resolution from NIH visible human project, and d) human brain images from Insight MRI.
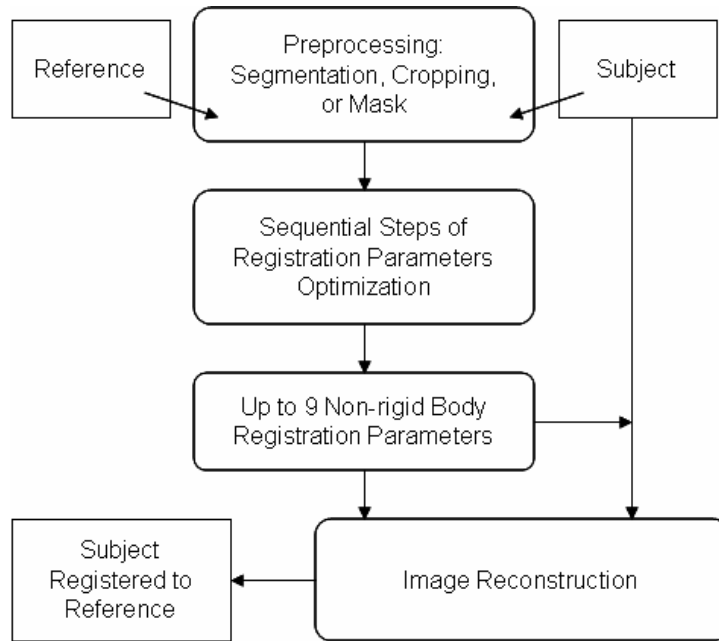
Figure 3-3   General synopsis of registration algorithm

Figure 3-3 describes the general synopsis of our implementation of GA registration. Prior to the GA registration, there is an optional step of image preprocessing. This preprocessing can be applied to a sub window of the main region of interest, or using some cropping technique [81], or other segmentation strategies to extract the interesting features (e.g., the skull). After the optional preprocessing, a sequential GA algorithm computing the parameters of the transformation is achieved based on genetic algorithm, which mitigated the time consuming problem of a simultaneous 8 chromosome GA strategy. Following the GA registration process, subsequent operations such as image interpolation or reconstruction can be implemented for different purposes.

3.3.1 Preprocessing

Based on the registration results of more than 8 sets of rat brain images and more than 4 breast images, the GA algorithm works well on original grayscale images. However, cropped or segmented volumes can achieve better results due to the reduced alignment spans. For brain images, the real region of interest for the rat studies is the brain, not the cranium or skull. Figure 3-4 shows that although two rat brains are aligned, the surrounding material can vary and trying to align the entire image might compromise the real region of interest. Therefore, before starting the GA registration process, some cropping strategies can be applied for identifying the region of interest, such as sub window (Figure 3-4d) or cropped image (Figure 3-4f) using a mask (Figure 3-4e) [81], etc. No system exists that can crop automatically for any geometry, but it is not a necessary requirement. As long as an algorithm crops "close" to the target or the cropped image includes most of the target area, the GA registration is implemented more on the interested area than the surrounding material, therefore provides a better optimization. The optimized transformation parameters will then be applied to the entire image.
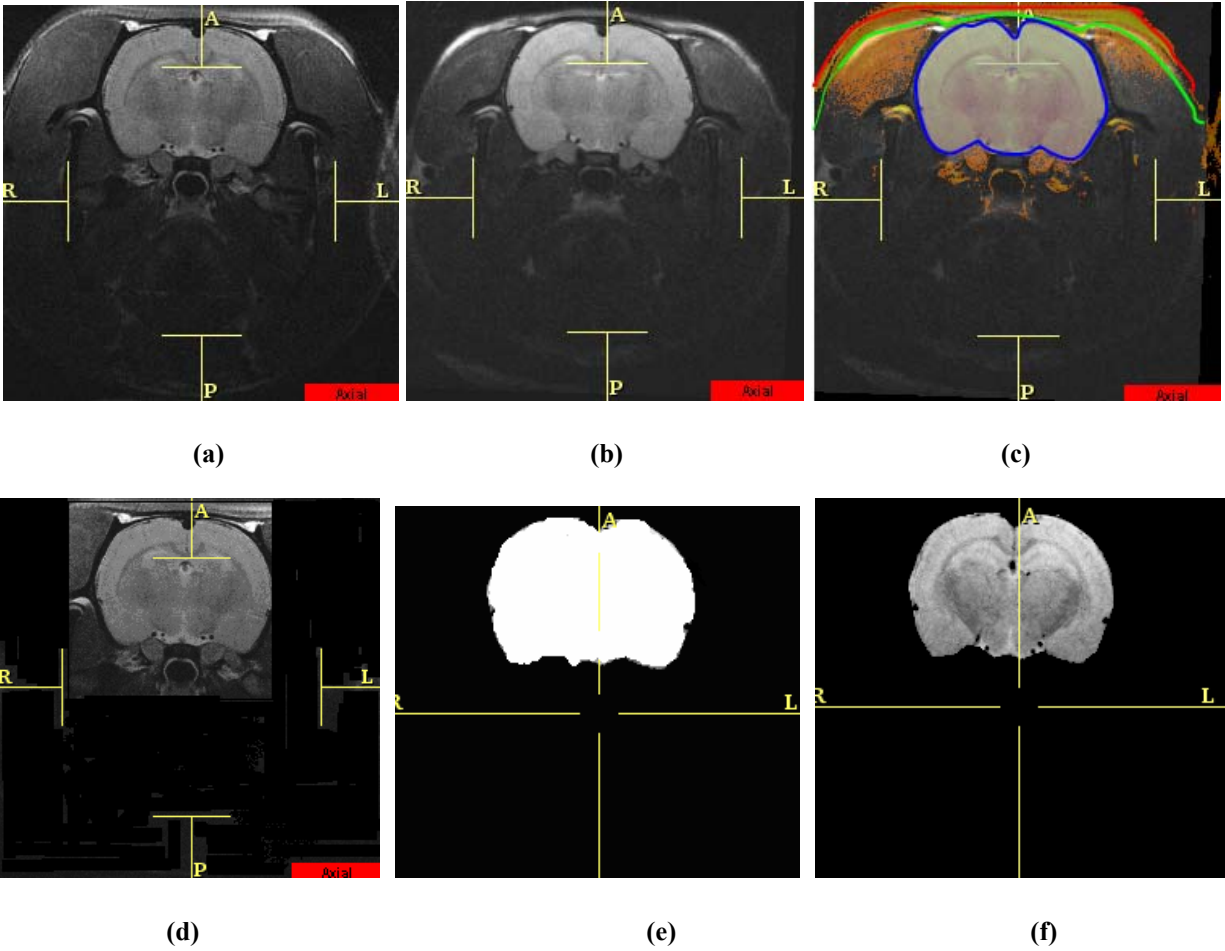
Figure 3-4   Brain MRI and the surrounding material

(a) Rat brain A; (b) Rat brain B; (c) Rat brain B superimposed on brain A. The blue curve surrounds the brain, and green indicates the outline of surrounding material of brain A and red indicates the outline of B; (d) A sub window that contains most part of the brain, if not all; (e) Mask; (f) Cropped image based on a mask;

3.3.2   GA registration

3.3.2.1   GA parameters

Our GA starts with creating an initial population of 20 parents. Each parent can have up to 8 chromosomes, one for each affine transformation parameter identified in matrix T in Eq.2-1,

except that the scaling in slice direction is determined by the header information of reference and subject images. This initial population is based on a random assignment of each chromosome within the specified range of that chromosome. For example Tx and Ty were both set within +/-30% of the lineal span whereas θ within +/- 30 degrees, etc. These chromosomes constructed the T matrix which was applied to the subject image. We used the sum of absolute difference (SAD, as described in chapter 2) as cost function on the transformed subject image compared to reference image to evaluate (rank) each individual M matrix. The top ranked 50% of the population were selected to be a parent. Their mates were a random selection from within this top 50% group, disallowing cloning. Our crossover function was a random percentage (X) and (1-X) of each chromosome for parent A and B, respectively. The mutation factor was $\frac{1}{n^2}$, where n is the number of chromosomes of each individual, introduced about every 30 generations 0[162]. The range of the mutated chromosome was the full spectrum of that parameter space, i.e. +/- 180 degrees for a rotation chromosome, providing a genetic offspring frequently outside the normally considered parameter boundaries.

3.3.2.2 Different registration heuristics

The original parents plus the offspring (creating a population size twice the original) were ranked. The top 50% of the original population size (not current population) were retained for subsequent generations. In this mode, if an original parent has a high ranking that genome can continue to produce in subsequent generations. Numerous GA implementations discard all the parents and rank only the offspring [10][18][80][162]. However, we have achieved better results including the parents within the ranking.

The GA was applied to MRI images of rat brains, human brains and breasts. The experimental rats used are Sprague-Dawley rats. This rat species is the overwhelming species used in research testing. Consequently, the size and shape of the rat brain is very consistent. The general pathway for manual alignment is to image the subject in an axial orientation, which is the dominant orientation of commercial rat-brain atlases. Therefore, the dominant component of registration is in-plane rotation and translation. Out-of-plane rotation might also be needed but the rotation angle is always small. A small scaling might be required too, but in many cases not (Figure 3-5).

This strategy was also tested on human brains and breasts. Results showed it is valid for human brain MRIs too but it didn't work nearly as well on breast images. Details will be illustrated in section 3.4.
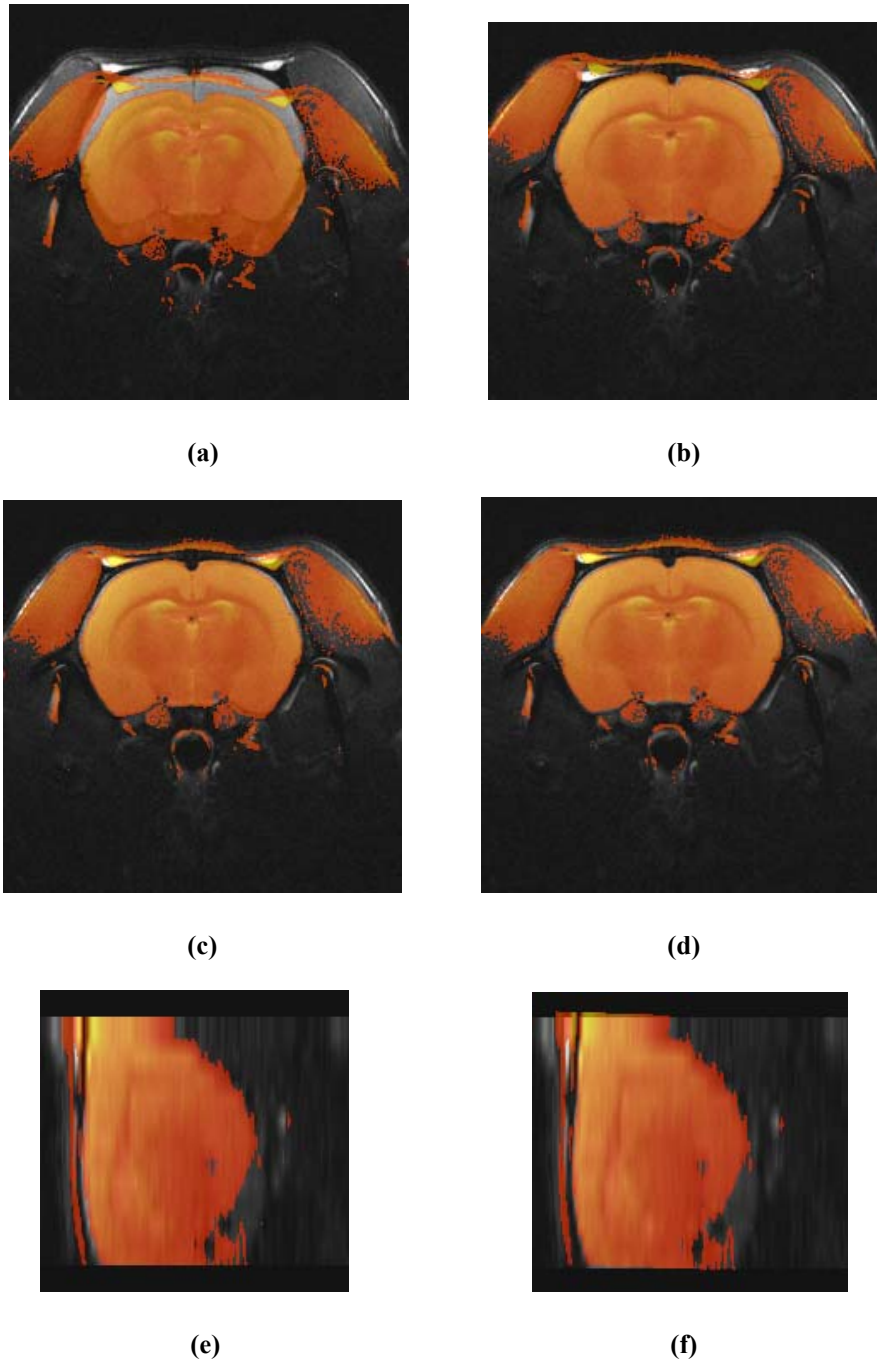
Figure 3-5   Registration components

(a) Initial misalignment: gray: reference; iron: subject   (b) Subject is translated to match reference

(c) Translated subject is rotated in plane to get a better alignment   (d) A small scaling 'might' be applied,

but perhaps not   (e) Sagittal view of the alignment   (f) A small out-of-place rotation may be required

3.3.2.2.1 In-plane registration applied to the whole volume

As described in the introduction, there are five transformation parameters for in-plane transformation: in-plane displacements T_x, T_y and axial rotation θ, and scaling factors S_x and S_y, that constructs the three chromosomes of each of the parents in GA algorithm. The 4×4 transformation matrix is:

$$T = \begin{bmatrix} S_x \cos\theta & \sin\theta & T_x & 0 \\ -\sin\theta & S_y \cos\theta & T_y & 0 \\ 0 & 0 & 1 & 0 \\ 0 & 0 & 0 & 1 \end{bmatrix}$$

Eq. 3-2

These five chromosomes can be applied either simultaneously or in a sequential mode of an initial rigid body transform followed by the two scaling factors. A single slice (usually the middle slice in the subject) is registered to the reference and the transformation matrix is applied to all slices.

3.3.2.2.2 Individual slice transformations

The five parameters are applied to each slice individually resulting in N transformation matrices, one for each of the N slices, thus form the registered N-slice volume.

3.3.2.2.3 3D non-rigid body transformation

The 9 transformation parameters for 3D non-rigid body registration are: displacements in x, y and z directions T_x, T_y and T_z, rotations about z, y and x axes θ, β and γ, and scaling factors in x,

y and z directions S_x, S_y and S_z. Among these 9 parameters, S_z can be determined directly from the reference and subject header information. The other 8 parameters form the 8 chromosomes in the genetic algorithm. The 4×4 transformation matrix:

$$T = \begin{bmatrix} S_x \cos\theta\cos\beta & -S_y \sin\theta\cos\beta & S_z \sin\beta & T_x \\ S_x(\cos\theta\sin\beta\sin\gamma + \sin\theta\cos\gamma) & S_y(\cos\theta\cos\gamma - \sin\theta\sin\beta\sin\gamma) & -S_z\cos\beta\sin\gamma & T_y \\ S_x(\sin\theta\sin\gamma - \cos\theta\sin\beta\cos\gamma) & S_y(\sin\theta\sin\beta\cos\gamma + \sin\gamma\cos\theta) & S_z\cos\beta\cos\gamma & T_z \\ 0 & 0 & 0 & 1 \end{bmatrix}$$

Eq. 3-3

3.3.2.2.4 Sequential steps of registration

The 8 chromosome GA registration is an extremely time consuming process, as shown in Table 3-1. In order to save computer resources and make the process computationally faster, we have implemented a strategy of sequential steps of registration.

Table 3-1   Quality of GA alignment on different images

$$GA\ Quality = \frac{(orig - GA)}{(orig - GS)} \times 100\%$$

	Rat Brain	Breast	Human Brain
GS	100%	100%	100%
GA	96.5%	65%	92%

Select a mid-slice 2D image and align it to the atlas using only in-plane translations and rotation. Generally the user manually positions the two images so that they are 'centered' and in-plane rotated appropriately. Subsequently, in-plane scaling is performed. The images are rotated to

the sagittal orientation and a rotation applied about the left-right axis which aligns the head-to-tail component. A translation in the slice direction is applied to match the subject/reference in the sagittal orientation. Finally, the images are rotated to the coronal orientation and a rotation applied about the superior-inferior axis.

A skilled user can align these 3D volume sets manually without frequent iterations of the sequential steps (Table 3-2). We have followed this sequential pattern observed with manual registration to our GA implementation. The sequential parameter group process has reduced the final 3D registration time significantly making it suitable for an automated alignment strategy. In summary, the sequential registration can be performed in 4 steps:

Step 1: Alignment in axial orientation

This process is executed with a 2D rigid body registration (translations and rotations in the axial plane). As stated previously, the scaling factor is considered a minor effect given the uniformity of rat brain's tissue properties. Therefore, a rigid body match can be a good initial guess of the final transformation. More importantly, it reduces the computing time significantly.

Step 2: In-plane scaling factors

Once the error is minimized via the 3-parameter GA alignment, an in-plane scaling is applied as a final correction factor in the registration process. The constant of GA scaling parameters is real numbers from 0 to 2.

Step 3: Translation in the slice direction

Step 4: rotation in the sagittal and coronal orientations

Rotations in the sagittal and coronal orientations can be very small. Once this final step is finished, the subject volume is aligned to the reference with an affine transformation matrix.

3.3.2.3   Cost function

The basic cost function we used is the sum of absolute difference (SAD) pixel intensities between the two images.   For a reference image R and subject S with dimension of $M \times N$ (usually M and N are even numbers), if the intermediate transformed image matrix is S^T, then the cost function is:

$$SAD = \frac{1}{M \times N} \sum_{i=1}^{M} \sum_{j=1}^{N} \left| S^T_{ij} - R_{ij} \right|$$

3.3.3   Image reconstruction

Once the proper transformation matrix M is found by GA algorithm, the new coordinates of each pixel in the subject are calculated.   For 2D images or in-plane registration, the new coordinates of pixel (x, y) are:

$$\begin{bmatrix} x* \\ y* \\ 1 \end{bmatrix} = T \cdot \begin{bmatrix} x \\ y \\ 1 \end{bmatrix}$$

Where x* and y* are the new coordinates for pixel value of (x, y) in the new image, and T is defined in Eq. 3-2.

For 3D transformation,

$$\begin{bmatrix} x* \\ y* \\ z* \\ 1 \end{bmatrix} = T_3 \cdot \begin{bmatrix} x \\ y \\ z \\ 1 \end{bmatrix}$$

where T_3 is defined in Eq. 3-3.

3.4   A sample result

In order to analyze the performance of GA registration, a user-friendly interface was designed for the registration package (Figure 3-6). This package includes all the GA registration strategies discussed in the previous section.
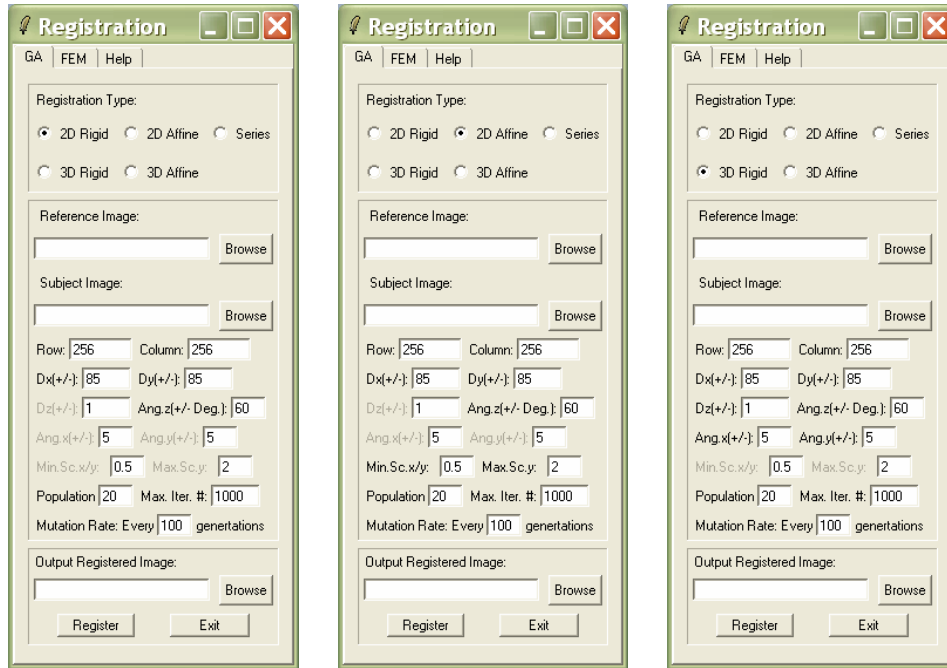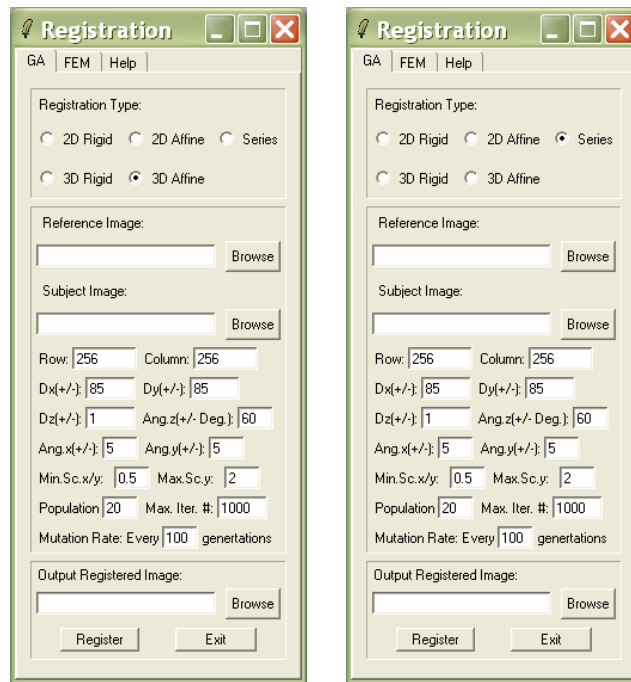
Figure 3-6   Registration package

(a) 2D rigid body (b) 2D affine (c) 3D rigid body (d) 3D affine (e) Sequential

Top frame: registration type

For user to choose one from the five exclusive GA methods;

Middle frame: user specifies reference and subject images.

The package takes sdt/spr raw files as the standard image type. Filename.sdt is the binary image data and Filename.spr stores the ascii header information, such as the pixel resolution, world coordinate spacing, etc. Other image formats can be converted to sdt/spr via some medical image processing software, such as MIVA (a package for Medical Image Visualization and Analysis) [32]. Once the header file is read in, pixel size of the image is shown on the interface.

In order to enhance the GA performance, users can specify transformation parameters based on experience. Or, the interface gives the default parameter settings as follows: in-plane translation Dx and Dy are restricted within +/- one third of the image's pixel size, out-of-plane translation Dz is restricted within +/- one slice. In-plane rotation angle is restricted within +/- 60 degrees, out-of-plane rotation +/- 5 degrees. For affine registration, scaling factors are between 0.5 to 2, which means the image can be shrunk to half the original size or expanded to twice. Also, user can specify the following GA parameters or take the defaults that the interface provides: population, maximum iteration number, mutation rate, etc.

Bottom frame: output

After choosing the output file name for the registered subject, user can go ahead and hit "Register" to run GA registration. On average, it takes about 4 minutes to run a 2D rigid body registration of a 256×256 image. 3D affine may be extremely slow but the sequential registration takes shorter, generally within 15 minutes for a volume with the dimension of $256 \times 256 \times 12$.

a) Original alignment   b) GA alignment   c) Gold Standard

(Manual registration by a skilled user)

d) brain image and its mask   e) cropped image   f) GA aligned based on cropped images
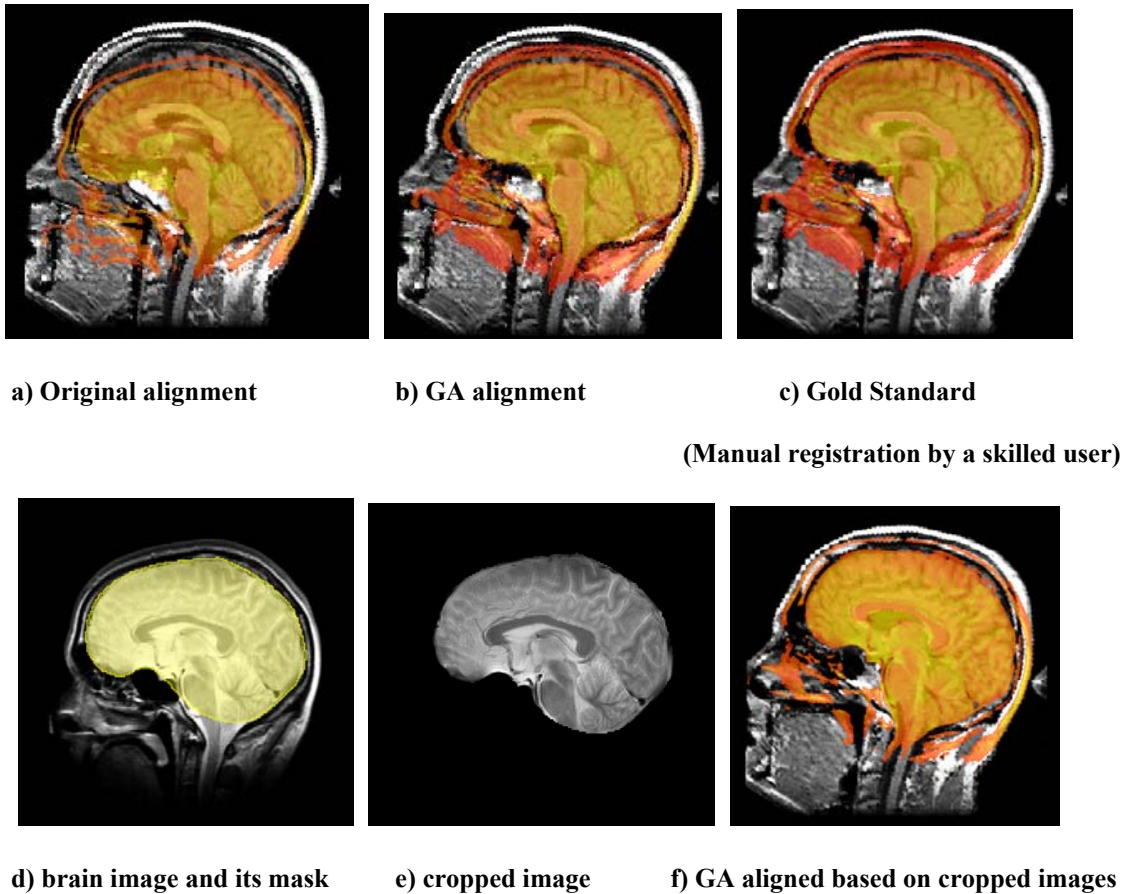
Figure 3-7   GA registration applied on human brains

3D MR images of rat brains, human breasts, and human brains were used as testing examples. Results showed good alignments for rat brains and human brains, but the quality for breast alignments is poor, as shown in Figure 3-7, 3-8. Figure 3-7 also shows that the registration

algorithm provides a better alignment on cropped images that contain only the interested region – brain (Figure 3-7 e, f). Table 3-1 lists the average registration accuracy of each image species compared to gold standard (manual registration performed by skilled user). These results will be examined in detail in Chapter 6. All tests were implemented on a Pentium 4 PC with the configuration of 1.8 GHz and 1G Ram on Windows XP OS.
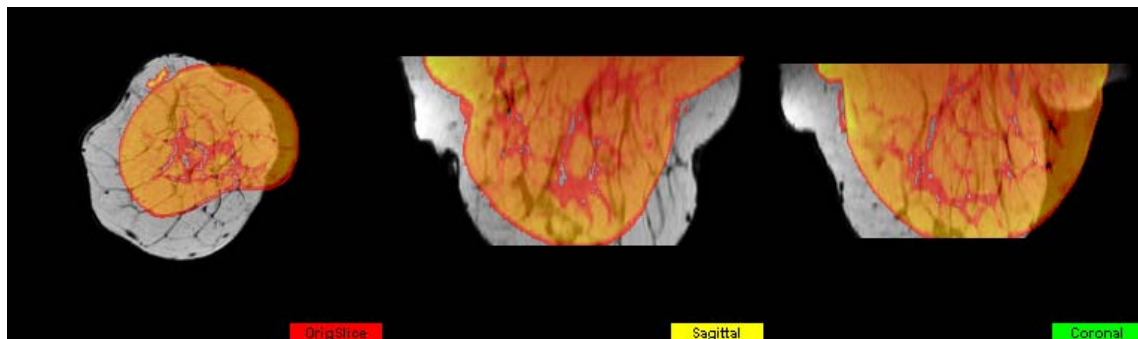
a) Original alignment
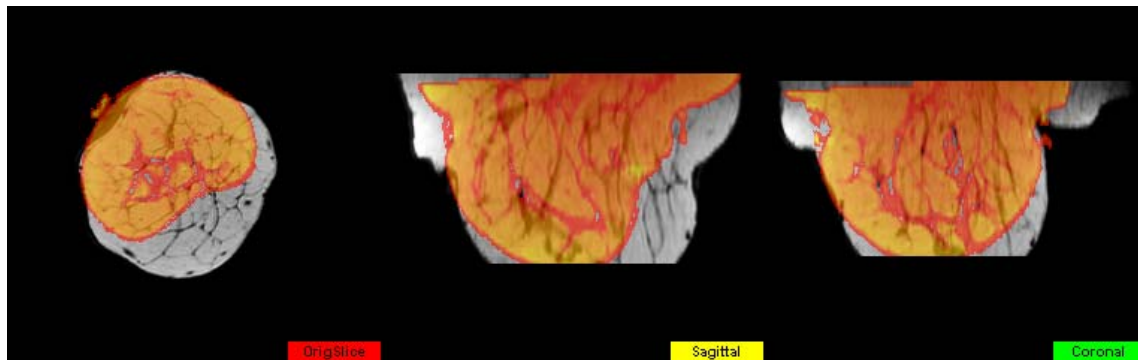
b) Alignment by GA

Figure 3-8   GA registration applied on breast images

Two 256×256 slices (Figure 3-9a) were registered by the GA registration. The whole registration process is achieved in an average of 15 seconds. Three chromosomes applied are translations in x and y direction and rotation about z. GA parameter constraints were automatically set as [-40 40] pixels for translation in both directions and [-30 30] degrees for rotation. The result was compared with that of AIR (Automated Image Registration) package, as shown in Figures 3-9(b)(c). The alignment differences were graphically indistinguishable.

a) original misalignment   b) AIR registered   c) GA registered
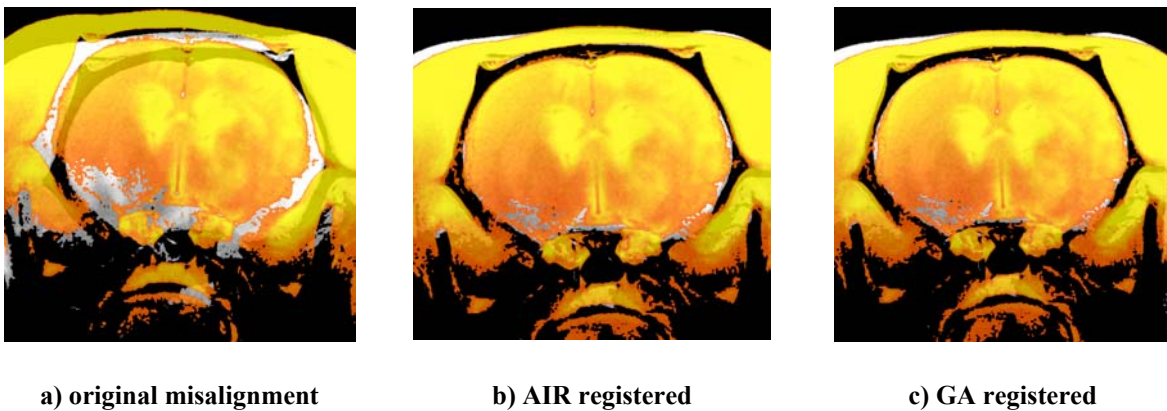
Figure 3-9   Initial misalignment, AIR registration and GA registration

(Grayscale image is the reference, colored the subject)

3.4.1   Simultaneous 3D non-rigid body registration

A simultaneous 3D non-rigid body registration was executed on two volumes of $256 \times 256 \times 12$. GA parameter constraints were based upon the volume dimensions: [-40 40] pixels for in-plane translation, [-2 2] slices for axial translation, [-30 30] degrees for in-plane rotation and [-2.5 2.5] degrees in rotation in the sagittal and coronal views (Figure 3-10).
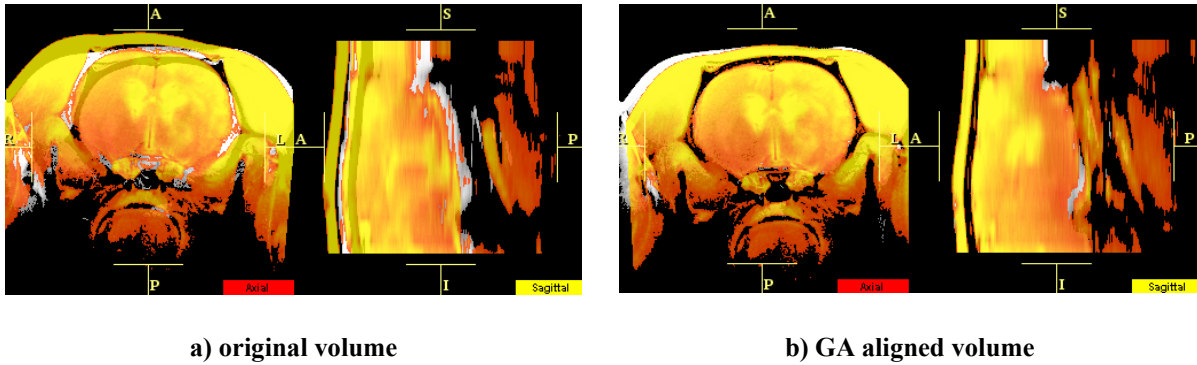
a) original volume   b) GA aligned volume

Figure 3-10   Initial misalignment of 3D MRI and volumes registered by simultaneous GA

(Grayscale volume is the reference, and colored the subject)

3.4.2   Sequential 3D non-rigid body registration

This GA registration approach was also applied on two MRI volumes with dimensions $256 \times 256 \times 12$. GA parameter constraints were automatically based upon the volume resolution and intensity. The parameter constraints used for our particular examples were: [-40 40] pixels for in-plane translation, [-2 2] slices for axial translation, [-30 30] degrees for rotation about z and [-2.5 2.5] degrees about x and y. The secondary scaling range was [0 2] for in-plane adjustments. Figure 3-11 displays the initial misalignment and the registered subject using GA techniques. Pre-cropping technique was applied here too (Figure 3-11a). The alignment was again compared with the result of AIR. Although AIR performed the registration with speeds up to twice as fast, it required pre-threshold settings to get results comparable to our GA system. Additionally numerous test examples failed to converge using AIR whereas the GA approach attained in average 96% agreement with the gold standard registration (manual registration) for all test cases. Table 3-2 shows the registration results based on intensity errors (SAD) compared with the gold standard (GS). The GA registration method has an average accuracy of 96.5%

relative to the gold standard, and the sequential GA can fasten the simultaneous GA by 30% in average.

a) original volumes   b) GA aligned volumes
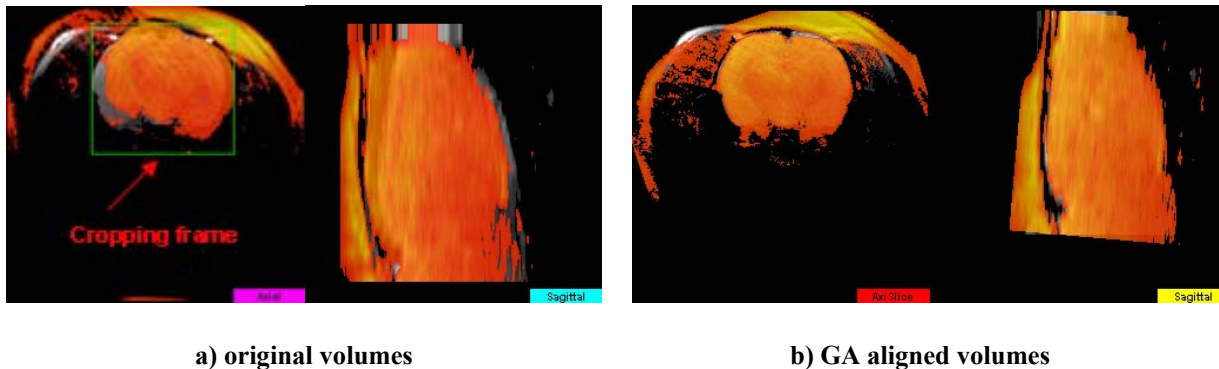
Figure 3-11   Initial misalignment of volumes and volumes registered by sequential GA

(Grayscale: reference   Colored: subject)

3.5 Discussion

One of the greatest benefits of GA algorithm is the lack of a required quality start location. However, if a certain region of the image is of more interest, then an image pre-cropping can enhance the registration accuracy (Figure 3-4). We cropped some MRI volumes of the brain and comparison showed the GA provided excellent alignments with quantified error values less than those recorded for manual registration.   The process is independent of user experience and interruption.

The advances of our GA approach include: a) retention of high ranked parents in the natural selection process; b) incorporating a mutation avenue that prevents cloning; c) introduction of sequential GA routine to mimic those sequences of skilled manual alignments to save computing time.

Table 3-2   Comparison of GA registration with other registration methods

$$\text{(Time: minutes   Accuracy:} \frac{(orig - reg)}{(orig - GS)} \times 100\%)$$

		R-A	R-B	R-C	R-D	R-E	H-A	H-B
GS	**CPU time**	8	5	5	4	5	10	8
	Accuracy	100%	100%	100%	100%	100%	100%	100%
Manual	**CPU time**	30	22	25	25	28	35	25
	Accuracy	99.8%	100%	99.7%	98%	97%	97%	99.2%
AIR	**CPU time**	30	25	27	Failed	33	Failed	45
	Accuracy	97.4%	98%	96.7%	N/A	98.6%	N/A	91%
GA1	**CPU time**	8	5	5	5	7	10	24
	Accuracy	97.4%	97.7%	96%	93.5%	95.4%	92%	92.7%
GA2	**CPU time**	350	280	290	360	350	500	540
	Accuracy	97.4%	97.7%	96%	93.5%	95.4%	92%	92.7%
GA3	**CPU time**	150	100	135	105	130	295	225
	Accuracy	97.4%	97.7%	96%	93.5%	95.4%	92%	92.7%
GA4	**CPU time**	70	45	60	45	50	130	118
	Accuracy	97.7%	97.7%	96.5%	94%	96.7%	94.5%	95%

GS – gold standard, performed by skilled user in registration

Manual – performed by technically qualified user, but not an expert at registration

AIR – performed by AIR package (Automated Image Registration)

GA1 – in-plane rigid body Genetic Algorithm with 3 chromosomes on one slice, applied to all slices

GA2 – in-plane rigid body Genetic Algorithm applied on each slice with 3 chromosomes followed by two scaling factors, N transformation matrices applied individually on each of the N slices

GA3 – affine transformation with 8 chromosomes applied simultaneously to the whole volume set

GA4 – Genetic algorithm, 8 chromosomes applied sequentially

4 LINEAR ELASTIC MODEL

4.1 Introduction

In order to make reliable analyses and diagnoses for longitudinal studies or composite studies of multiple image subjects, alignment of subjects to a reference is required. Numerous medical image registration strategies have been developed [2][5]. Rigid body or affine registration produces a 4x4 homogeneous transformation matrix to align two or more images. However, this strategy does not allow for non-uniform or differential deformations within the image domain. A finite element representation of the image set offers numerous opportunities for alternative alignments [63][44][45]. In this chapter we present a method that performs cropping [81], finite element mesh deployment [87][116], application of a plane-strain elastic formulation [82][83] to align subject slices to reference slices. The process is automatic, reliable and does not require user intervention.

4.2 Deformable transformation

Unlike rigid body or affine transformations that alters the shape of a subject with a 4x4 uniform transformation matrix; deformable transformation (Figure 4-1) does not have a uniform transformation matrix. With deformable transformation, pixels in the same image can be moved in various directions in different scales (Figure 4-2). Therefore, the shape of a subject can be changed to account for localized soft tissue deformation (such as female breasts and human lungs), sampling process or imaging techniques.
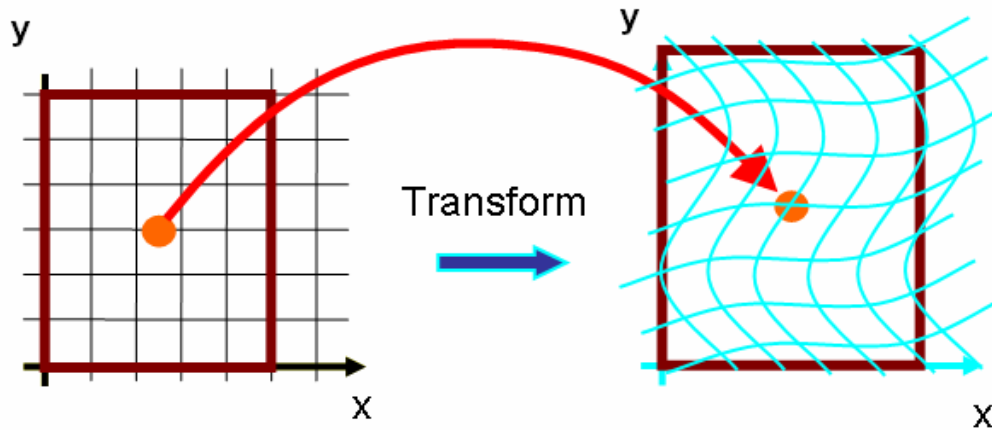
Figure 4-1   Schematic of a possible deformable transform

Source: http://www.itk.org   ITK Insight-DeformableRegistration-Demons.ppt
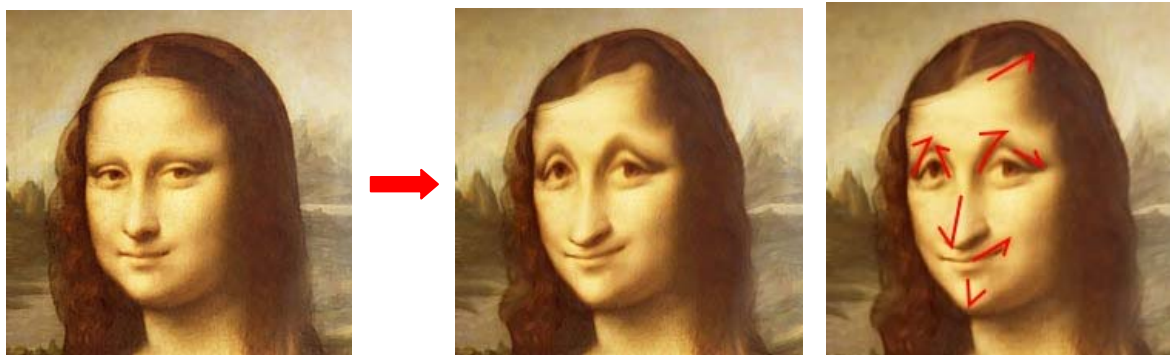
Figure 4-2   Deformed image

Source: Web source

4.2.1   Deformable models

Deformable object modeling has been studied in computer graphics for more than thirty years [117], across a range of applications.   In computer-aided design and computer drawing applications, deformable models are used to create and edit complex curves, surfaces, and solids. Computer aided apparel design uses deformable models to simulate fabric draping and folding

[169]. In image analysis, deformable models have been used to segment images and to fit curved surfaces to noisy image data [170][171][172]. Deformable models have been used in animation and computer graphics, particularly for the animation of clothing, facial expression, and human or animal characters. Finally, surgical simulation and training systems demand both real-time and physically realistic modeling of complex, non-linear, deformable tissues [118].

Deformable models can be classified as: non-physical and physical models [117]. Non-physical models are purely geometric techniques particularly used in design. Physical models use some sort of physical principles to compute the shapes or motions of deformable objects.

4.2.1.1 Non-physical models

One type of non-physical model is splines and patches. In order to numerically describe curves and surfaces, designers use a small vector of numbers (or control points) such as B-splines (Figure 4-3) and β-splines [119] to represent planar and 3D curves and use related 2D patches 0 for specifying surfaces. In these representations, the curve or surface is represented by the set of control points.
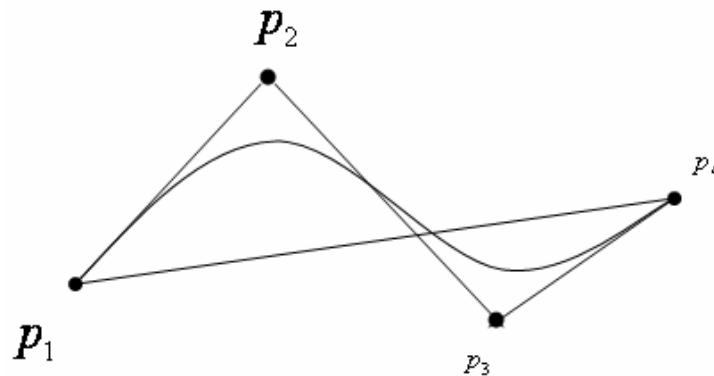
Figure 4-3   A cubic B-spline curve based on control points p_1, p_2, p_3 and p_4

Another type of non-physical model is the free-form deformation (FFD) 0. Instead of changing

the shape of an object by adjusting individual control points, FFD changes the shape by

deforming the space in which the object lies, through a mapping function f: $\Re^3 \to \Re^3$. [123][124]

Non-physical methods (purely geometric) for modeling deformation are limited by the expertise

and patience of the user. Deformations must be explicitly specified and the system has no

knowledge about the nature of the objects being manipulated. Although these methods have

some advantages, the increased computing power and graphics capabilities have steered the

designers to use physically based methods for modeling.

4.2.1.2   Physical models

4.2.1.2.1 Mass-spring models

Mass-spring systems are one technique that has been used widely for modeling deformable

objects [125][126]. An object is modeled as a collection of point masses connected by springs in

a lattice structure (Figure 4-4). The spring forces can be linear or nonlinear for tissues such as

human skin that exhibit inelastic behavior. The equations of motion for the entire system are

assembled from the motions of all the mass points in the lattice:

$$M\ddot{x} + C\dot{x} + Kx = f$$

Where M, C, K are the $3N \times 3N$ mass, damping, and stiffness matrices, and vector f is a 3N

dimensional vector representing the total external forces on the mass points.
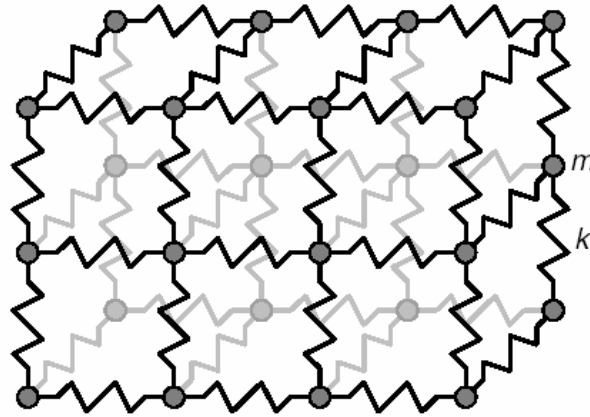
Figure 4-4   A portion of a mass-spring model

Springs connecting point masses exert forces on neighboring points when a mass is displaced from its rest

positions [117]

Mass-spring systems are a simple model with well understood dynamics. They are easy to construct, and can be animated at fast rates [117]. However, mass-spring models have some drawbacks [127]. The discrete model is a significant approximation of the true physics that occurs in a continuous body. Certain constraints are not naturally expressed in the model. Also, sometimes large spring constants are used to model objects that are nearly rigid and have poor stability, requiring the numerical integrator to take small time steps, which tremendously slows down the computing process [128].

4.2.1.2.2 Continuum models and finite element methods (FEM)

Mass-spring models start with a discrete object model, while more accurate physical models treat deformable objects as a continuum: solid bodies with mass and energies distributed throughout. The full continuum model of a deformable object considers the equilibrium of a general body

acted on by external forces. The object deformation is a function of these acting forces and the object's material properties. The object reaches equilibrium when its potential energy is at a minimum.

It should be pointed out here that deformable models can be discrete or continuous but the computational methods used for solving the models in computer simulations are ultimately discrete. Finite element method (FEM) is the most popular method [130][131][132][133] used to find an approximation for a continuous function that satisfies some system equilibrium [134]. In FEM, the continuous object is divided into elements joined at discrete node points. A function that solves the equilibrium equation is found for each element. The solution is subject to constraints at the node points and the element boundaries so that continuity between the elements is achieved [117]. The following paragraphs illustrate how a FEM is used to solve a typical 2D plane strain linear elasticity problem, where the strain in the z direction is assumed to be zero.

4.2.1.2.3 Theory of 2D plane strain linear elasticity [131]
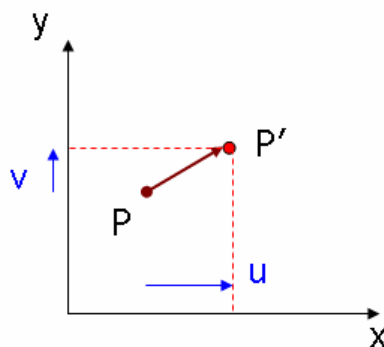
Figure 4-5   Displacement of P to P' by displacement subvectors u and v

First, define a 2D displacement field (u,v), where u is the displacement in x direction and v the displacement in y, as shown in Figure 4-5.

Consider zero external force, the system equilibrium equation is:

$$\sum F = 0$$

Based on this system equilibrium, normal stress σ_x, σ_y and shear stress τ_{xy} have the following equilibrium:

$$\frac{\partial \sigma_x}{\partial x} + \frac{\partial \tau_{xy}}{\partial y} = 0$$

$$\frac{\partial \tau_{xy}}{\partial x} + \frac{\partial \sigma_y}{\partial y} = 0$$

Eq. 4-1

Meanwhile, we have normal and shear strains:

$$\varepsilon_x = \frac{\partial u}{\partial x} \qquad \varepsilon_y = \frac{\partial v}{\partial y} \qquad \gamma_{xy} = \gamma_{yx} = \frac{\partial u}{\partial y} + \frac{\partial v}{\partial x}$$

According to Hooke's law,

$$\sigma_x = E\varepsilon_x + v\sigma_y \qquad\qquad \text{Eq. 4-2}$$

$$\sigma_y = E\varepsilon_y + v\sigma_x \qquad\qquad \text{Eq. 4-3}$$

Where E is the material's Young's modulus and v its Poisson's ratio. Substitute Eq. 4-2 into Eq. 4-3:

$$\sigma_y = E\varepsilon_y + v(E\varepsilon_x + v\sigma_y)$$

After reorganizing we get:

$$\sigma_y = \frac{E}{1-v^2}(\varepsilon_y + v\varepsilon_x) \qquad\qquad \text{Eq. 4-4}$$

Similarly

$$\sigma_x = \frac{E}{1-v^2}(\varepsilon_x + v\varepsilon_y)$$ **Eq. 4-5**

Note that

$$\tau_{xy} = G\gamma_{xy}$$

$$E = 2G(1+v)$$

Where G is the shear modulus.

Assume plane strain: $\varepsilon_z = \gamma_{yz} = \gamma_{xz} = 0$,

Substitute Eq. 4-4 and 4-5 into Eq. 4-1, we get

$$\frac{E}{1-v^2}(\frac{\partial^2 u}{\partial x^2} + v\frac{\partial v^2}{\partial x \partial y}) + G(\frac{\partial^2 u}{\partial y^2} + \frac{\partial v^2}{\partial x \partial y}) = 0$$

$$G(\frac{\partial^2 u}{\partial x \partial y} + \frac{\partial v^2}{\partial x^2}) + \frac{E}{1-v^2}(v\frac{\partial^2 u}{\partial x \partial y} + \frac{\partial^2 v}{\partial y^2}) = 0$$

Simplify these two equations we get the elastic equilibrium equations in terms of displacement:

$$\frac{\partial^2 u}{\partial x^2} + v\frac{\partial^2 v}{\partial x \partial y} + \frac{1-v}{2}(\frac{\partial^2 u}{\partial y^2} + \frac{\partial^2 v}{\partial x \partial y}) = 0$$

$$\frac{\partial^2 v}{\partial y^2} + v\frac{\partial^2 u}{\partial x \partial y} + \frac{1-v}{2}(\frac{\partial^2 u}{\partial x \partial y} + \frac{\partial^2 v}{\partial x^2}) = 0$$

Eq. 4-6

4.2.1.2.4 Solve elastic equations using FEM

In order to solve *u* and *v* in Eq. 4-6, triangular finite elements are built within the object.

1) Develop a FEM sequence for a two degree of freedom problem with an unspecified trial function into governing equation, i.e.

$$u \cong \hat{U} = \sum_{j=1}^{n} U_j N_j$$

$$v \cong \hat{V} = \sum_{j=1}^{n} V_j N_j$$

$$j=1, 2, \ldots, n$$

Where

n – Number of nodes in system (or, locally, in element)

U_j – Unknown coefficients to be determined, which are not a function of space

N_j – User specified basis function, which are a function of space, but not a function of time

2) Substitute for u and v of Eq. 4-6 the approximations defined in step 1 and multiply them by a weight function $W = \sum_{i=1}^{n} W_i$ then integrate over the domain and force it to zero:

$$\left\langle \frac{\partial^2 N_j}{\partial x^2} W_i \right\rangle U_j + v \left\langle \frac{\partial^2 N_j}{\partial x \partial y} W_i \right\rangle V_j + \frac{1-v}{2} \left\langle (\frac{\partial^2 N_j}{\partial y^2}) W_i \right\rangle U_j + \frac{1-v}{2} \left\langle (\frac{\partial^2 N_j}{\partial x \partial y}) W_i \right\rangle V_j = 0$$

$$\left\langle \frac{\partial^2 N_j}{\partial y^2} W_i \right\rangle V_j + v \left\langle \frac{\partial^2 N_j}{\partial x \partial y} W_i \right\rangle U_j + \frac{1-v}{2} \left\langle (\frac{\partial^2 N_j}{\partial x^2}) W_i \right\rangle V_j + \frac{1-v}{2} \left\langle (\frac{\partial^2 N_j}{\partial x \partial y}) W_i \right\rangle U_j = 0$$

3) Integrate by parts, and apply boundary condition – zero forces in x and y

$$\left\langle \frac{dN_j}{dx} \frac{dW_i}{dx} \right\rangle U_j + v \left\langle \frac{dN_j}{dy} \frac{dW_i}{dx} \right\rangle V_j + \frac{1-v}{2} \left\langle \frac{dN_j}{dy} \frac{dW_i}{dy} \right\rangle U_j + \frac{1-v}{2} \left\langle \frac{dN_j}{dx} \frac{dW_i}{dy} \right\rangle V_j = \int F_{x-bdy} ds = 0$$

$$\left\langle \frac{dN_j}{dy} \frac{dW_i}{dy} \right\rangle V_j + v \left\langle \frac{dN_j}{dx} \frac{dW_i}{dy} \right\rangle U_j + \frac{1-v}{2} \left\langle \frac{dN_j}{dx} \frac{dW_i}{dx} \right\rangle V_j + \frac{1-v}{2} \left\langle \frac{dN_j}{dy} \frac{dW_i}{dx} \right\rangle U_j = \int F_{y-bdy} ds = 0$$

Where s is the boundary. Note that F_{x-bdy} and F_{y-bdy} are only applied on boundary nodes, not on the whole domain.

4) Assemble matrices

The formed equation should look like:

$$[A]\left\{ {U_j \atop V_j} \right\} = \{Rhs_j\}$$

Where A is a banded matrix of dimension DOF*NN, DOF is degree of freedom, and NN is number of nodes. Assigning in(L,i) the global node number information of local node number i of element L, the pseudo code for assembling the banded matrix is as follows:

```
for i = 1:3
        Ix = 2*in(L,i) − 1;                        % global matrix locations: x-row
        Iy = Ix + 1;                               % y-row
        for j = 1:3
                Jy = 2*in(L,j);
                Jx = Jy − 1;
                JB = Diag + (Jy - Iy);             % Diag = halfbandwidth +1;
                % x row equation                   % A is area of triangle
                e(JB,Ix) = e(JB,Ix) + dy(j)*dy(i)/(4*A) + (1-nu)*dx(j)*dx(i)/(8*A);
                e(JB+1,Ix) = e(JB+1,Ix) - nu*dx(j)*dy(i)/(4*A) - (1-nu)*dy(j)*dx(i)/(8*A);
                % y-row equation
                e(JB-1,Iy) = e(JB-1,Iy) - nu*dy(j)*dx(i)/(4*A) - (1-nu)*dx(j)*dy(i)/(8*A);
                e(JB,Iy) = e(JB,Iy) + dx(j)*dx(i)/(4*A) + (1-nu)*dy(j)*dy(i)/(8*A);
        end
    end
```

5) Apply boundary conditions and solve equilibrium equation

Typically there are two types of boundary conditions: Dirichlet boundary condition and Neumann boundary condition [131][134].

A Dirichlet boundary condition, often referred to as a type I boundary condition, specifies the values a solution is to take on the boundary of the domain. That is, for a partial differential equation on a domain $\Omega \subset \Re^n$, on the boundary,

$$\frac{\partial U}{\partial x} = 0$$

A Neumann boundary condition specifies the values that the derivative of a solution is to take on the boundary of the domain. That is, for a partial differential equation on a domain $\Omega \subset \Re^n$, on the boundary,

$$\frac{\partial U}{\partial x} = f(x) \qquad \forall x \in \partial\Omega$$

Type I boundary condition is an exact satisfactory which does not use differential equation, while Neumann boundary condition requires differential equation and boundary.

6) Solve the problem

Use the node displacements and the interpolation functions of a particular element to calculate displacements for points within the element.

4.2.1.2.5 Other deformable models

There are other deformable models such as snakes [135][136] [137], hybrid models [138][139][140], and low degree of freedom models [141][142]. These are all approximate models that solve the problem approximately but are computationally faster compared to FEM [117].

4.2.2 Methodology

This dissertation focuses on the registration of medical images, especially rat brains, human breasts and human brain images. These subjects are all soft tissues and often prone to deformations beyond the traditional 4x4 matrix alignment strategies. We present an automatic non-rigid body registration using a linear elastic finite element formulation based on contour matching. The whole process does not require manual interruption, and offers good registration accuracy with some constraints, such as the images to be registered should be in the same 3D orientation, etc.

4.3 Implementation

This section presents an automatic non-rigid body registration using a linear elastic finite element formulation. A subject MRI volume set is passed through a Pulse Coupled Neural Network (PCNN)[81][163][164][165] which automatically segments the images [166] and creates a binary mask of the desired area (e.g., the brain, Figure 4-6). Details of this process will be explained in section 4.3.1. A slice series is defined as the ratio of slice contour perimeter to its contained area. An example of such is plotted as a function of slice number in Figure 4-10. A similar mask of the reference and its slice series is already created. With the given image header information, a slice alignment based on matching the two slice series of reference and subject is applied. Section 4.3.2 illuminates this process. Then for each matched pair of reference and subject slices, the subject perimeter contour is orientated to match the reference contour based on a least-squared error analysis of the total Euclidean distance from contour points to the geometric centroid. This process is discussed further in section 4.3.3. A 2D finite element mesh is

67

automatically created on the subject image slice [83][84][116]. The linear elastic formulation for plane strain is applied to the finite element mesh [82][131]. Iterative incremental displacements are applied on the boundary with the finite element formulation dictating the domain alignment. The process terminates once the subject perimeter is tagged to the atlas perimeter. The method was successfully tested on magnetic resonance images (MRI) of rat brains and human breasts.
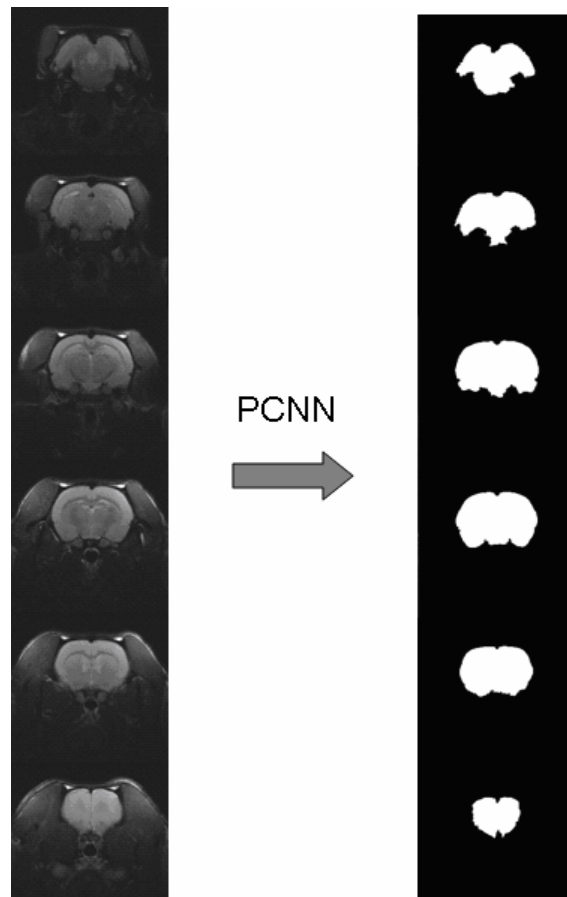
Figure 4-6   Binary masks created by PCNN from a grayscale volume set
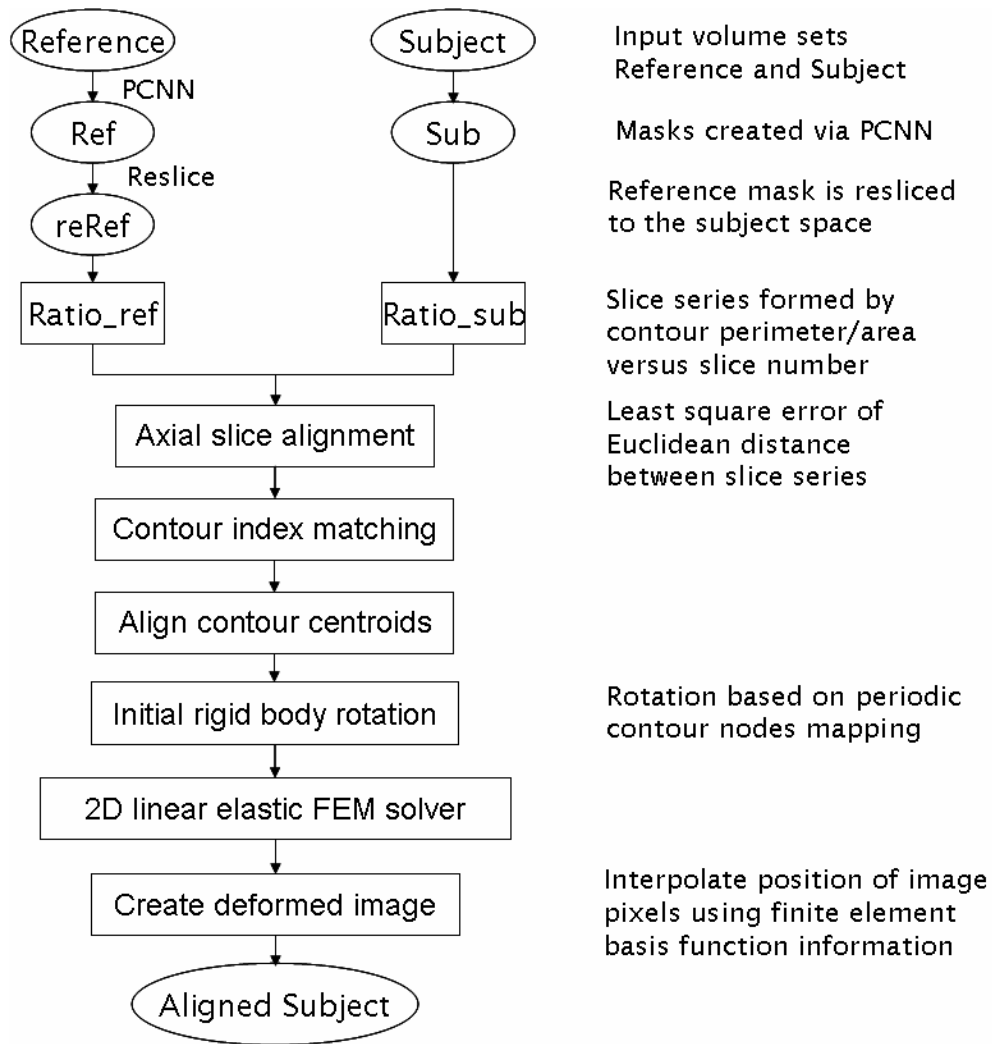
Figure 4-7   Linear elastic registration using FEM formulation

Figure 4-7 shows the scheme of this model-based elastic registration applied on rat brains. It does not require manually created landmarks.

4.3.1   Mask creation and image cropping

The registration process begins with image cropping. The reference and subject MRI images (Figure 4-8) are sent through a Pulse-Coupled Neural Network (PCNN) [81], an automatic image

cropping process [164][165]. Proposed by modeling a cat's visual cortex, PCNN iteratively produces binary images of increasing area as the intensity spectrum is increased. We use it to separate the tissue of interest (the brain, for example, which has overall lighter shades of gray) from the surrounding structures. The output is a set of binary masks [134]. By applying binary masks produced by PCNN to the original image, cropped grayscale images are created which contains only the desired area (brain) (Figure 4-9).
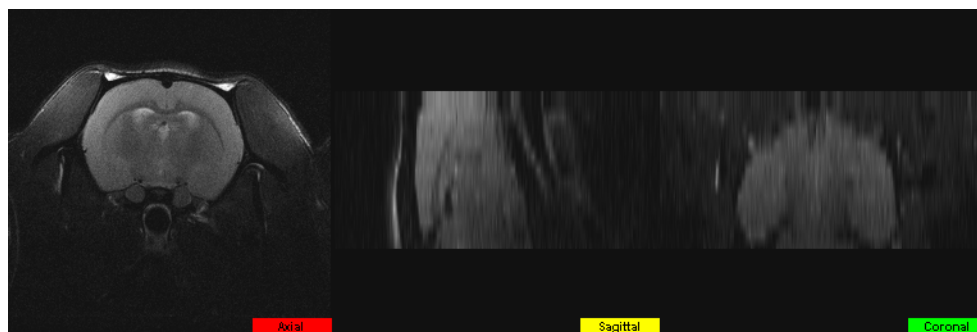
Reference
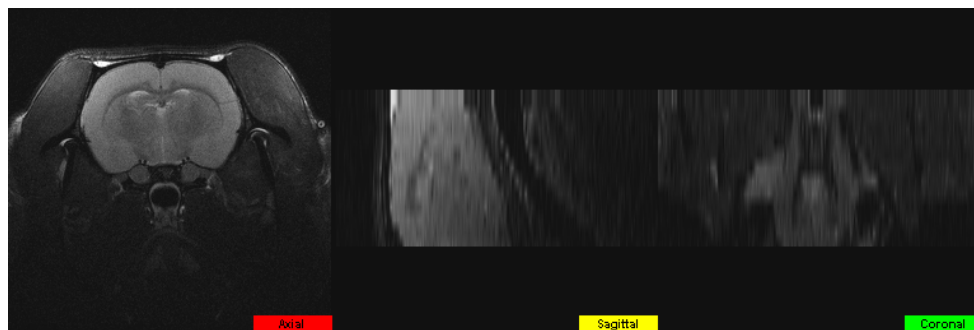
Subject

Figure 4-8   Original images

Original image　　　　**Binary mask**　　　　**Cropped area**
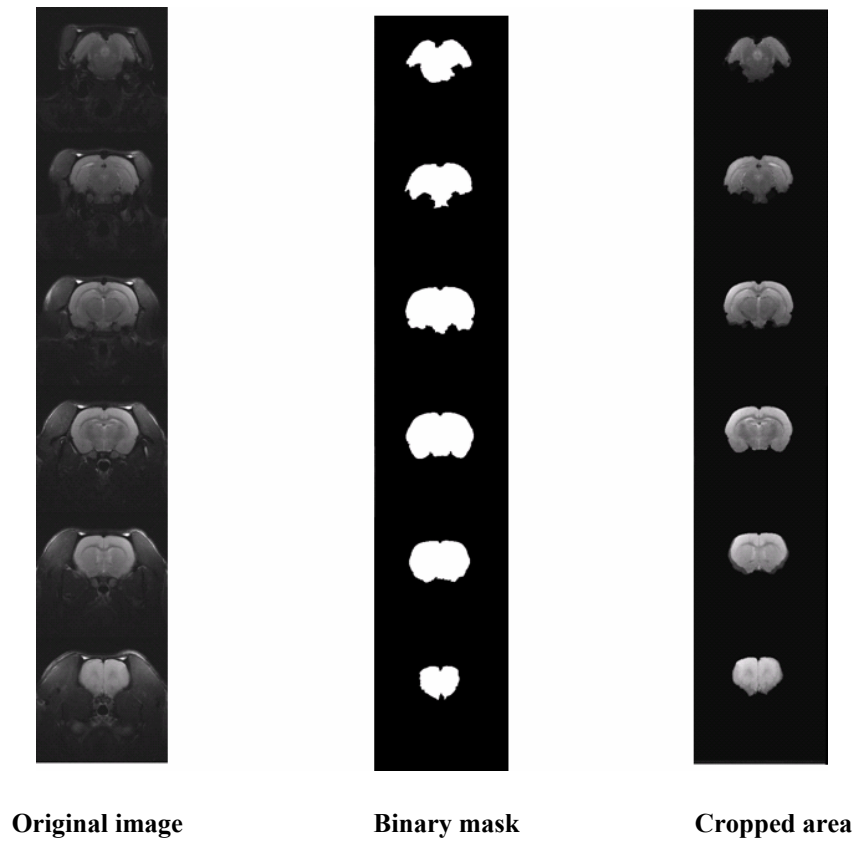
Figure 4-9　Original image, binary mask and its cropped image

4.3.2　Slice alignment

With the binary mask sets, ratio of contour perimeter and area is calculated. A curve (slice series) of perimeter/area as a function of slice position can be created. Based on empirical observation, all curves of rat brain slice series tend to be bell-shaped, as shown in Figure 4-10. Since all rat brain mask slice series have this shape similarity, a slice alignment strategy was developed based on maximizing shape similarity.
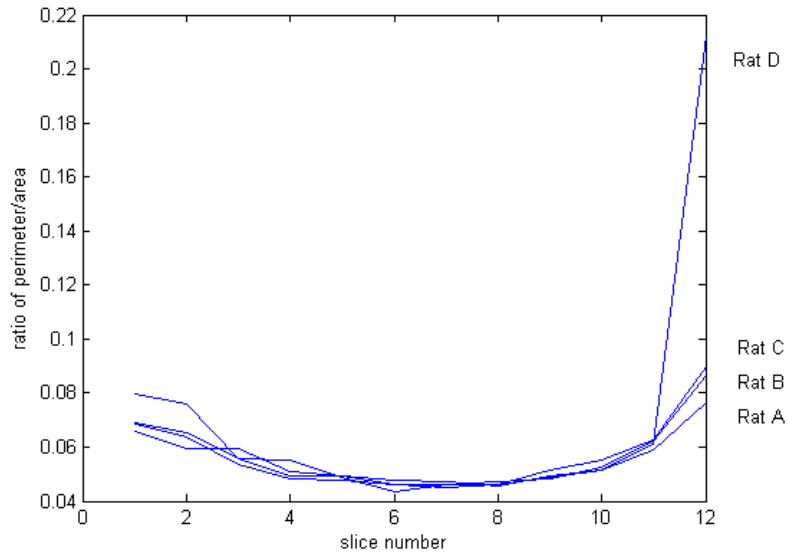
Figure 4-10   Slice series based on contour perimeter/area ratio

4.3.2.1   Form time series

The perimeter (P) of each slice mask (Figure 4-11) and its interior area (A) are calculated. Slice series of the ratio P/A as a function of slice number are graphed (Figure 4-12a) for reference and subject, respectively.
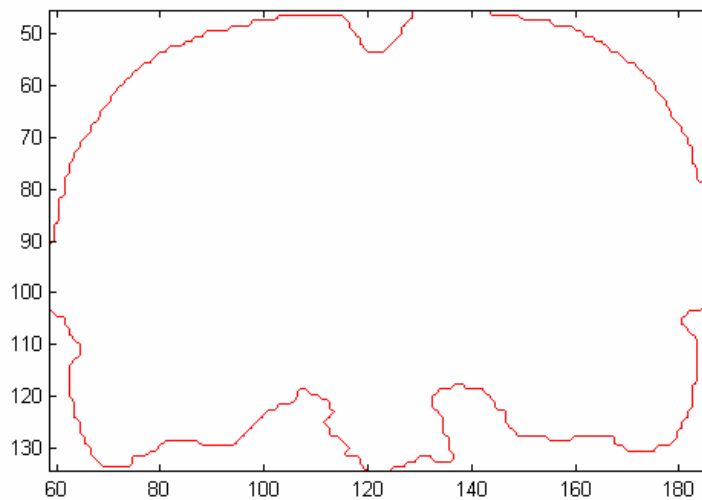
Figure 4-11   A contour of brain mask
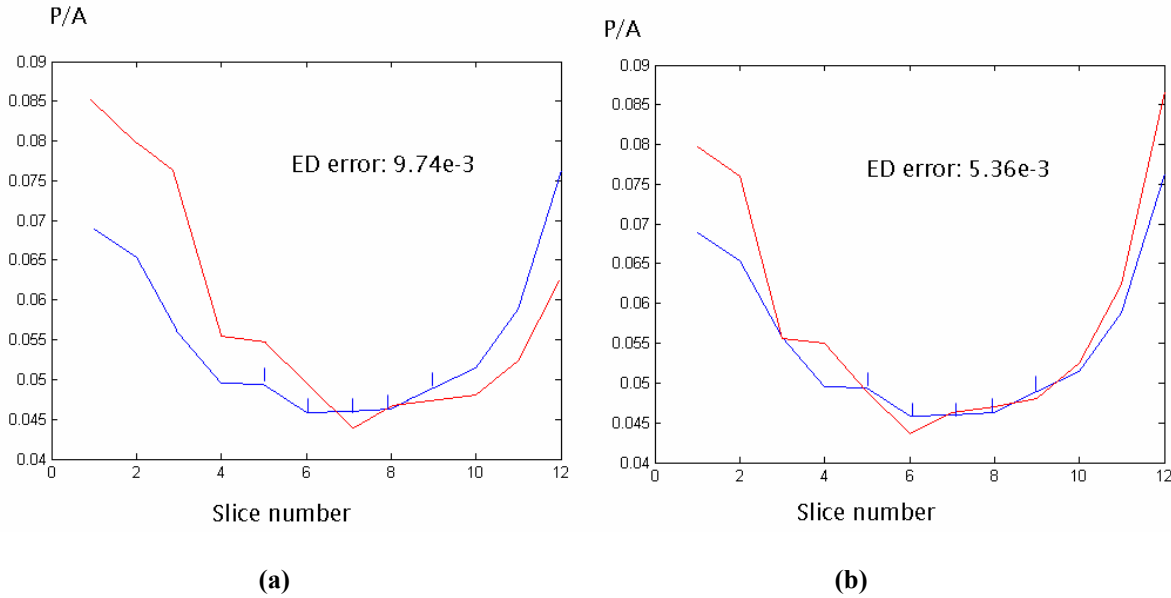
Figure 4-12   Slice series based on P/A

Red: reference   Blue: subject

4.3.2.2   Match slice series

The reference slice series remains fixed while the subject series is incrementally indexed along it. A subset of the slice series S of subject (e.g. the middle third of the slices) is used to quantify the quality of alignment. Based on a least square distance error, find the best matching continuous subset R in reference for subset S (Figure 4-12, marked by vertical lines). Given the number of steps N that the subject needs to move in the slice direction, and the reference and subject slice intervals from their header information Δz_R and Δz_S, the shift and scaling in z direction can be decided as follows:

shift: $Tz = N * \Delta z_S$;

scaling: $Sz = \dfrac{\Delta z_R}{\Delta z_S}$

where Tz is the translation in the z direction (slice direction); Sz is the scaling factor; N is the shifting number of subject slice series; Δz_R is the z interval of reference image, and Δz_S is the z interval of subject image.

4.3.2.3   Reslice

In order to align slices in the next steps, the reference mask set is resliced to the subject space so that it has the same number of slices as the subject. Generally, the reference volume has greater detail via higher resolution and number of slices than subject volume sets.

4.3.3   2D Contour matching

After the z-slice alignment, the translated and z-scaled (if necessary) subject mask and cropped image is sent into the 2D deformable registration process with the reference mask. A perimeter contour of each mask is established using a fixed set of uniform boundary line segments, as shown in Figure 4-13(a), (b). These two contour shapes are converted to "time series" using the Euclidean distance from the boundary line points to the centroid (Figure 4-14) [30][101]. By comparing subject time series to the reference time series, the subject segment index is permutated to minimize the least-square error of the two perimeters (Figure 4-13c).
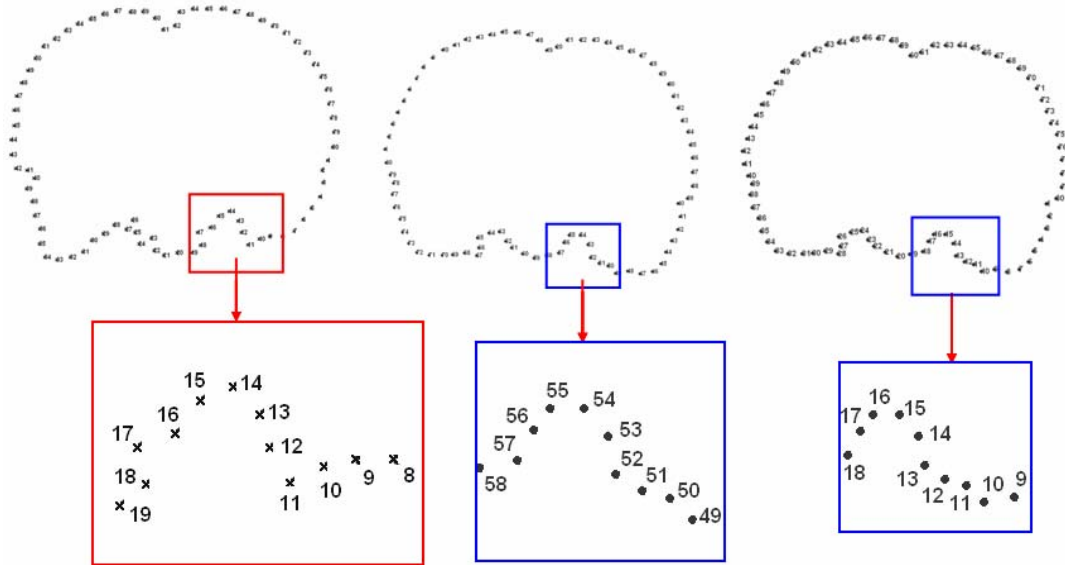
a) Reference contour **b) Subject contour** **c) Subject contour reindexed**

Figure 4-13   Image contours
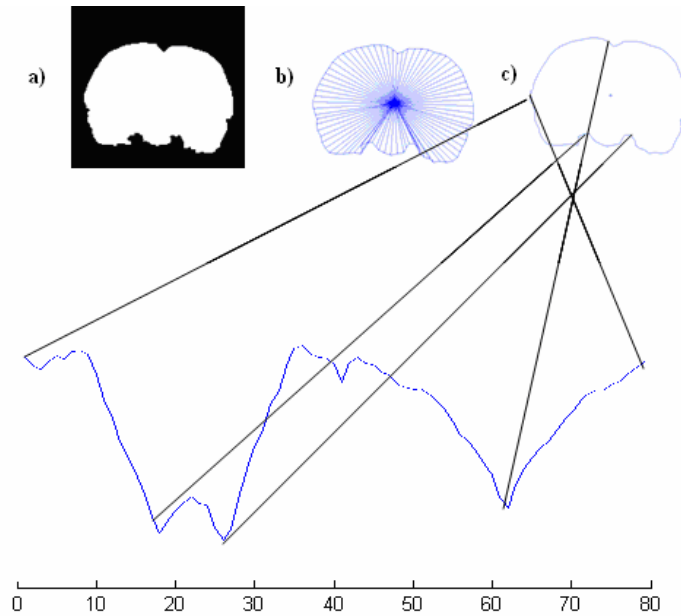
Figure 4-14   Shape of a contour is converted to time series

a) White-black mask image of a rat brain; b) Euclidean distance from every point on the contour to the geometric centroid is measured and treated as the Y-axis of a time series c) of length n=80

Figure 4-15 shows the two time series before and after contour matching. Construct reference time series Q and subject series C of the same length n, which were extracted from contour shapes by Euclidean distance [134]:

$$Q = q_1, q_2, \ldots, q_i, \ldots, q_n$$

$$C = c_1, c_2, \ldots, c_j, \ldots, c_n$$
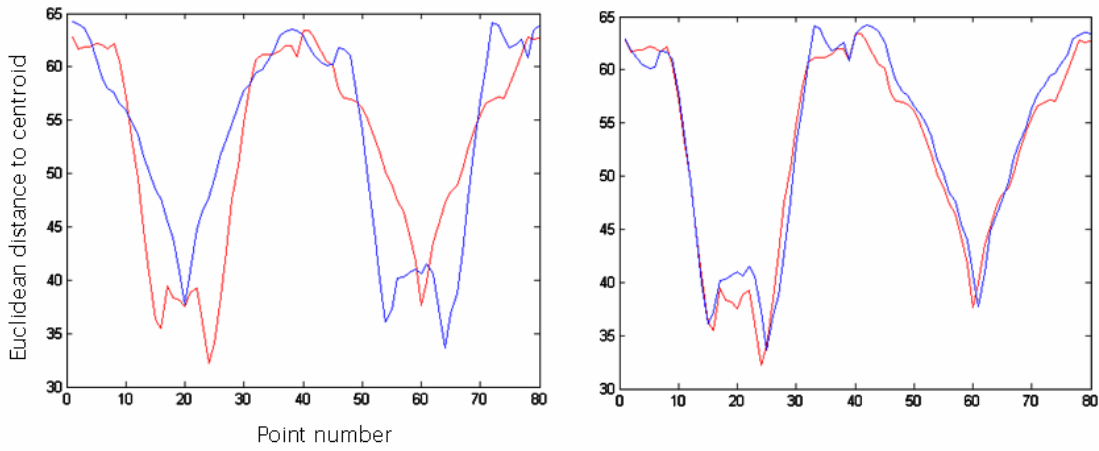
Figure 4-15   Time series before and after reindexing to minimize Euclidean distance error

Red: reference contour time series;   Blue: subject contour time series

The Euclidean distance between two 2D points $P(p_x, p_y)$ and $Q(q_x, q_y)$ is defined as:

$$ED = \sqrt{(p_x - q_x)^2 + (p_y - q_y)^2}$$

In order to match the two contour shapes, with reference shape held fixed, rotate the subject, and record the minimum distance of all possible rotations. We achieve this by expanding times series C into a new series with the length of 2n-1:

$$C' = c_1, c_2, \ldots, c_j, \ldots, c_n, c_1, c_2, \ldots, c_{n-1}$$

In order to compare the two time series, we use the ubiquitous Euclidean distance to evaluate error [30]:

$$Err(Q,C) \equiv \sqrt{\sum_{i=1}^{n}(q_i - c_i)^2}$$

In each trial of error calculation increase the first index of series C by 1. Below is the pseudo code to calculate this:

```
Algorithm: [bestSoFar] = Test_All_Rotations(Q,C')

bestSoFar = Inf;

for j=1:n
    distance = EA_Euclidean_Dist(Q, C'(j), bestSoFar)
                                    //C'(j) is a subseries of C' of length n C'(j:j+n)
    if distance < bestSoFar
        bestSoFar = distance;
        bestmatch = C'(j);
    end;
end;
return [bestSoFar];
```

Once the best matched contour time series, the subject contour indexing is rotated so it has the minimum Euclidean distance error with the reference, shown in Figure 4-13(c).

Based on numerous testing of rat brain and human brain image sets, this Euclidean distance error minimization provided good contour indexing matching for shapes that have a major axis [30][101]. However, for breast images or circular objects that do not have a dominant major axis, the time series curve appears to be more flat and the centroid is not a reliable local origin for calculating Euclidean distance (Figure 4-16).

(a) rat brain　　　　　**(b) human brain**　　　　　**(c) human breast**
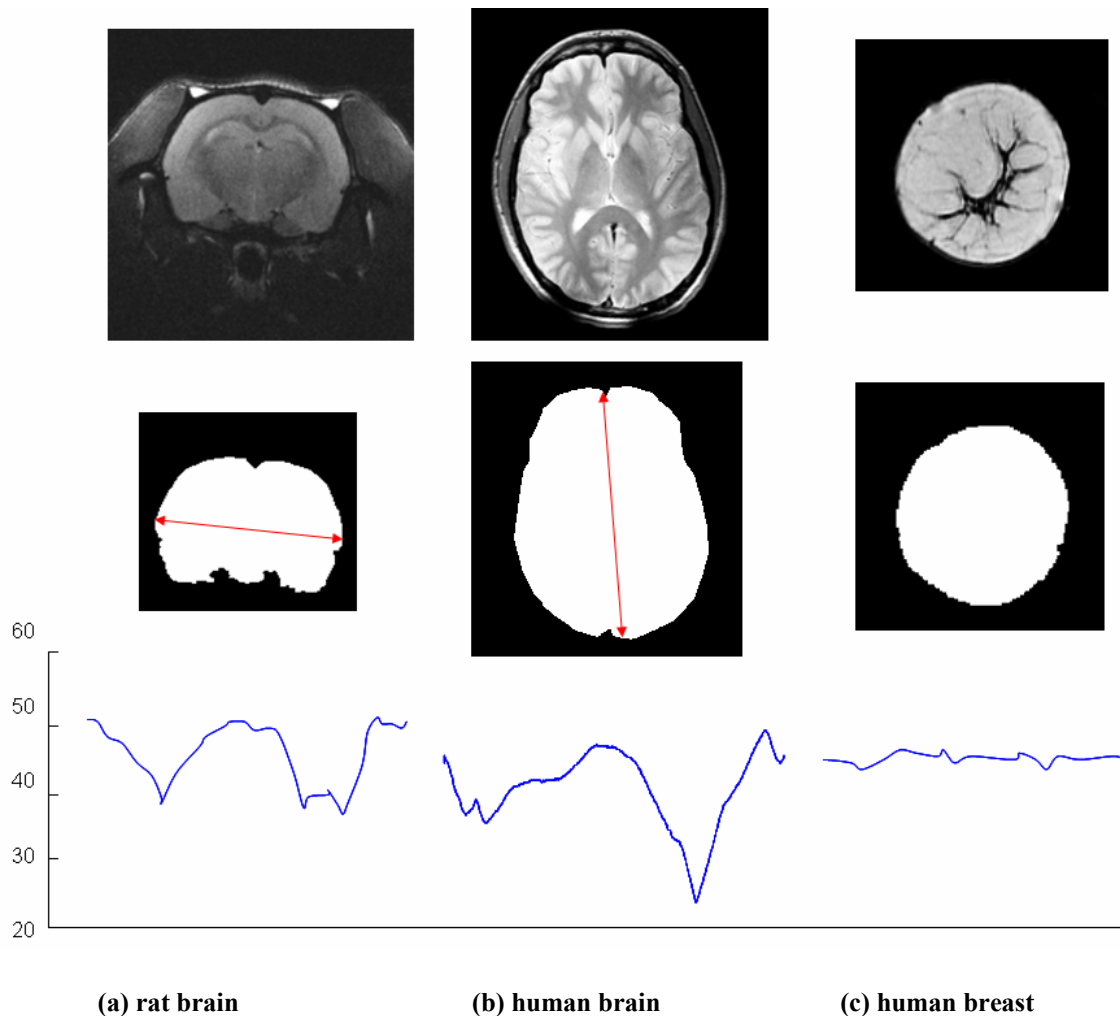
Figure 4-16   Major axis of rat brain and human brain, and unapparent axis in human breasts

4.3.4   Initial alignment and rigid body rotation

It has been shown that a rigid body transformation is of fundamental importance in image registration. Even when soft tissue deformation is involved, a rigid body transformation is critical [178][179][180]. Therefore, before applying the elastic FEM formulation, an initial rigid body slice alignment is applied. The subject slice is translated such that subject and reference centroids align, shown in Figure 4-17. Then based on the perimeter matching information, an average initial rotation angle about the centroid is calculated. N points (e.g. 10% contour points)

on subject contour are randomly selected. The average angle is calculated between these points to the centroid and their matching points on the reference to the centroid (Figure 4-18):

$$\alpha = \frac{1}{N} \sum_{i=1}^{N} \alpha_i$$

(a) Contours and centroids of reference and subject   (b) Centroids aligned
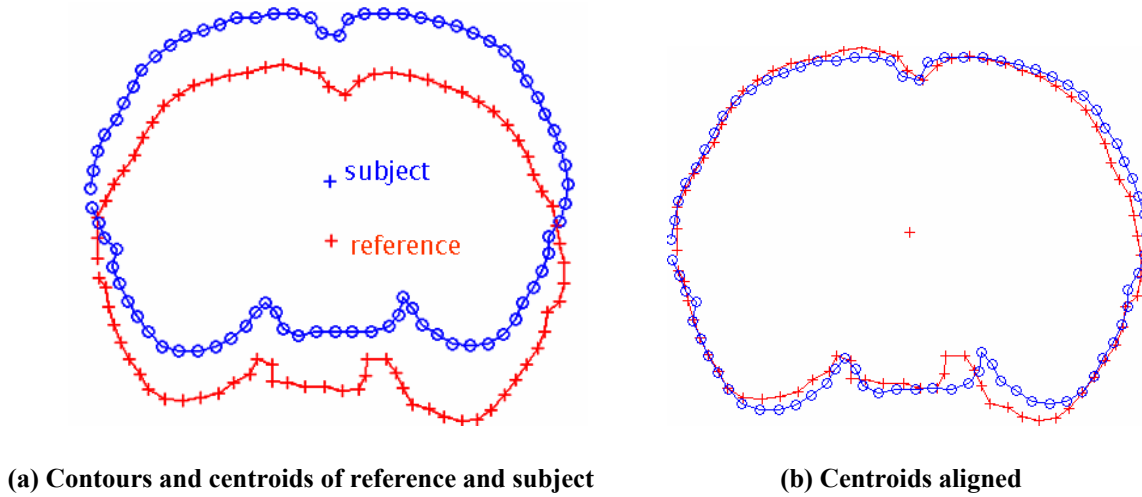
Figure 4-17   Centroid alignment
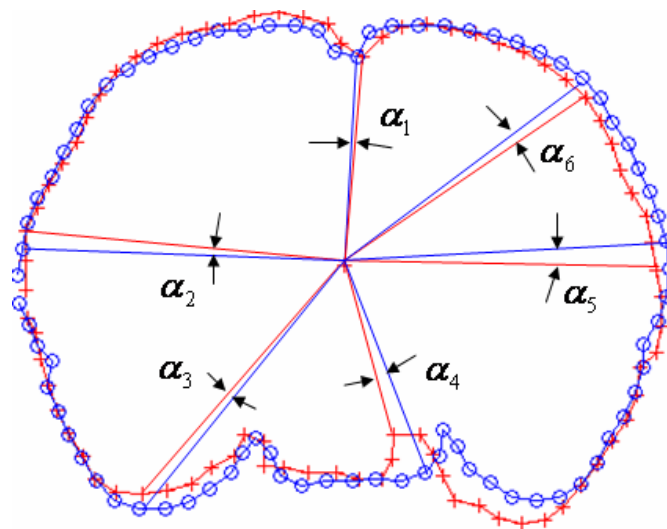
Figure 4-18   Initial rigid body rotation angle

4.3.5 2D triangular mesh generation

Once the two contour indices are matched and the subject is initially translated and rotated, soft-tissue distortions can be localized to appropriate regions of the reference. One is ready to create a mesh on the subject and use the reference contour as the target destination for the subject boundary. A Delaunay triangulation of the subject domain is automatically created [82][83][84], preserving the permutated perimeter order for application of the boundary conditions. Figure 4-19 shows a 2D finite element mesh created based on the contour.

| (a) Contour | (b) Triangular mesh |
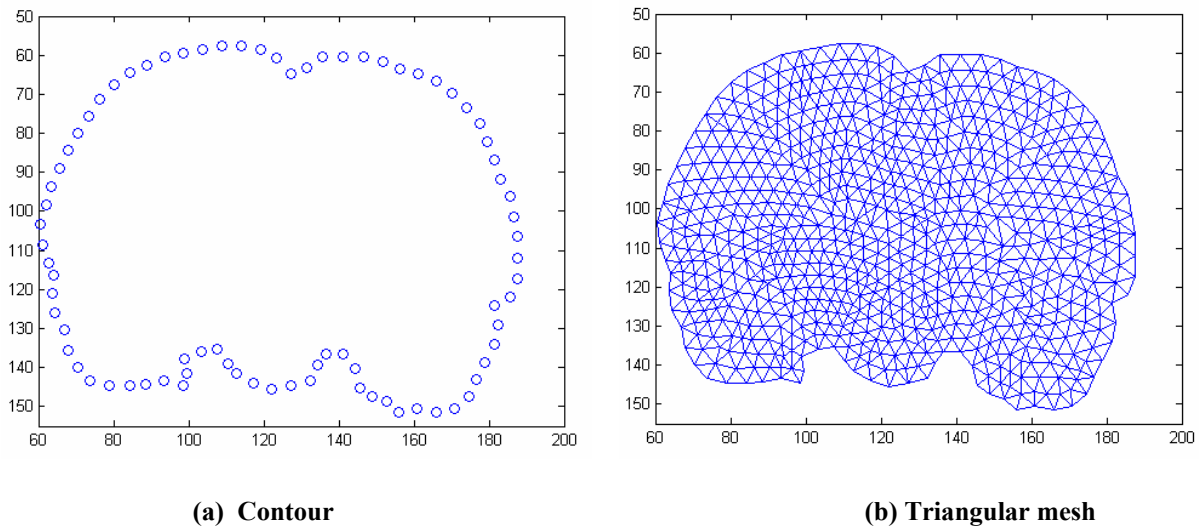
Figure 4-19   2D Delaunay finite element triangulation

4.3.6 Linear elastic transform

After the triangular mesh is created, a linear-elastic finite element formulation is applied to the domain with Type-I displacements boundary conditions, as described in section 4.2.1.2.4. According to documentations, Poisson's ratio is set to 0.5 [183][184]. Figure 4-20 shows an initial boundary alignment.
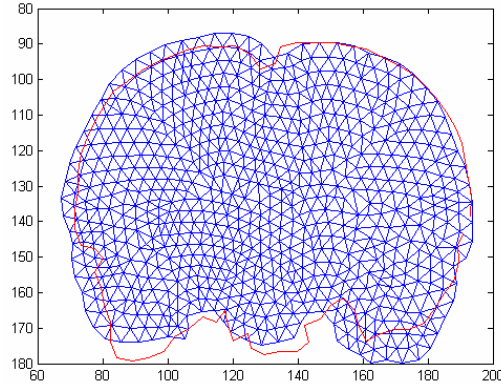
Red: reference boundary   Blue: Subject triangular mesh

Figure 4-20   Initial contour alignment

Generally, the displacement vectors exceed the linear elastic range. Therefore, the displacements are applied incrementally which requires reformulation of the elastic stiffness matrix (Figure 4-21):

1) Calculate the largest displacement vector;

2) Calculate the smallest element;

3) Target a small amount in element deformation at one time, (0.5% was used);

4) Calculate the number of required iterations of incremental deformation.

5) Incrementally apply boundary conditions of displacements in iterations.

The mesh topology remains constant and the process is completely automatic.

(a) ¼ total iteration

(b) ½ total iteration

(c) ¾ total iteration

(d) Final alignment
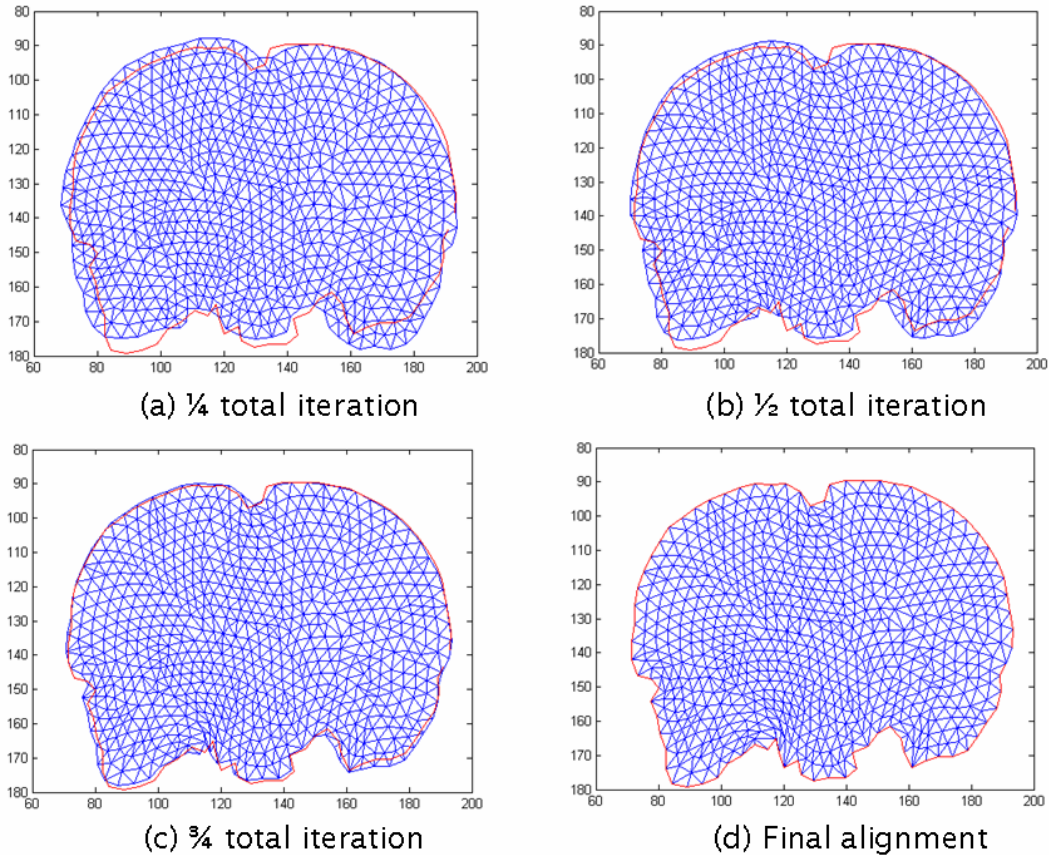
Figure 4-21   Linear elastic transform in a FEM application of 30 iterations

4.3.7   Transform image based on the FE basis function

When the finite element mesh motion terminates, each element node has a displacement as the result so that the mesh is reoriented in the mask space. Figure 4-22 illustrates how the grayscale image gets reoriented based upon the information of mesh deformation. In the undisturbed space of the subject mesh, every grayscale image pixel is associated with a given triangular element and each pixel has a specific position within that element. Every position within the element has a unique set of finite element basis functions, N_1, N_2, and N_3. The three basis function values for each pixel within the element are calculated and stored. After the mesh is deformed to fit the reference space, those same basis function values dictate the new location of the pixel (Figure 4-

23). Suppose the coordinates of the three nodes of element number K are $[x_i, y_i]$, where i=1,2,3, and their elastic displacements in x and y directions are dx_i and dy_i for i=1,2,3. According to the finite element result, the displacement dx and dy of pixel $[x, y]$ that is located in this element should meet the following planar basis function:
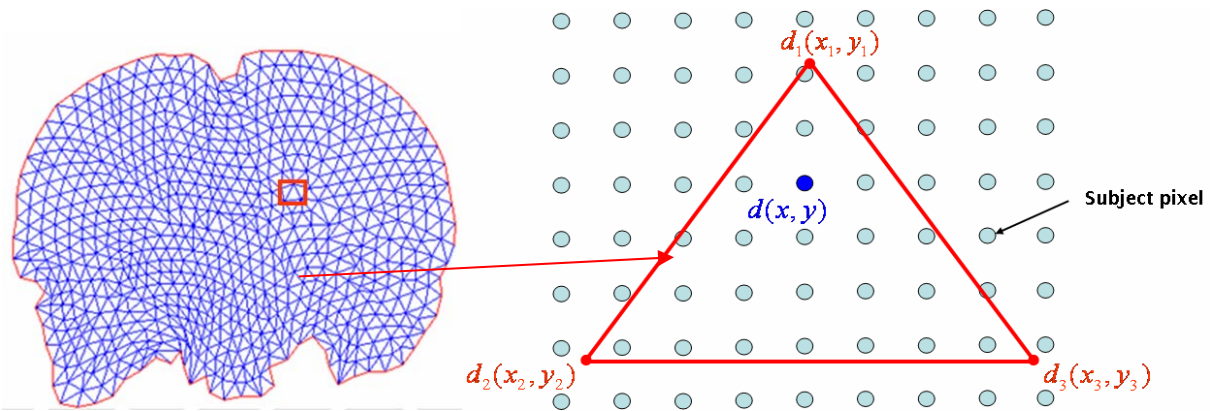
Figure 4-22   Relocate subject image pixels in reference mask space
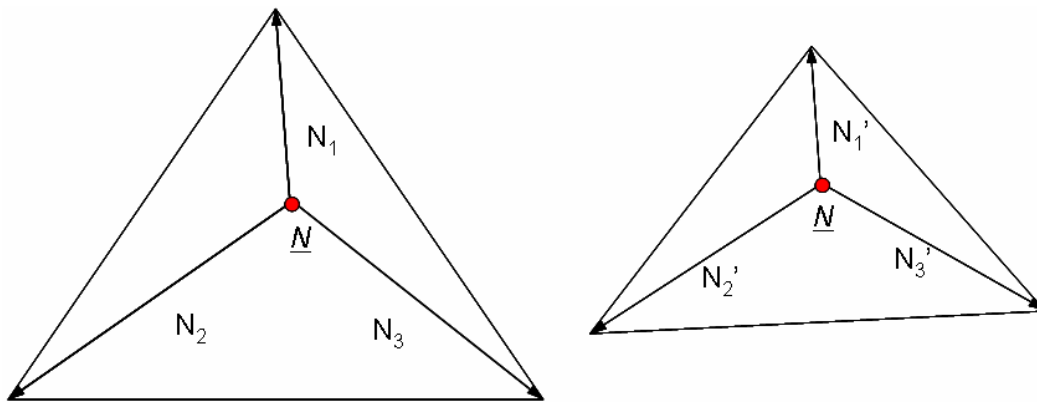
a) **Before deformation**   b) **After deformation**

$\underline{N}$=(N$_1$ N$_2$ N$_3$); N$_1$=N$_1$'=0.22, N$_2$=N$_2$'=0.4, N$_3$=N$_3$'=0.38

Figure 4-23   Basis functions stay the same after FEM deformation

$$\begin{vmatrix} y_2 - y_1 & dx_2 - dx_1 \\ y_3 - y_1 & dx_3 - dx_1 \end{vmatrix}(x - x_1) + \begin{vmatrix} dx_2 - dx_1 & x_2 - x_1 \\ dx_3 - dx_1 & x_3 - x_1 \end{vmatrix}(y - y_1) + \begin{vmatrix} x_2 - x_1 & y_2 - y_1 \\ x_3 - x_1 & y_3 - y_1 \end{vmatrix}(dx - dx_1) = 0$$

$$\begin{vmatrix} y_2 - y_1 & dy_2 - dy_1 \\ y_3 - y_1 & dy_3 - dy_1 \end{vmatrix}(x - x_1) + \begin{vmatrix} dy_2 - dy_1 & x_2 - x_1 \\ dy_3 - dy_1 & x_3 - x_1 \end{vmatrix}(y - y_1) + \begin{vmatrix} x_2 - x_1 & y_2 - y_1 \\ x_3 - x_1 & y_3 - y_1 \end{vmatrix}(dy - dy_1) = 0$$

The new coordinates $[x_n, y_n]$ for image pixel $[x, y]$ can be then decided by dx and dy :

$$x_n = x + dx$$

$$y_n = y + dy$$

(a)　　　　　　　　　　　(b)　　　　　　　　　　　(c)

(d)　　　　　　　　　　　(e)　　　　　　　　　　　(f)
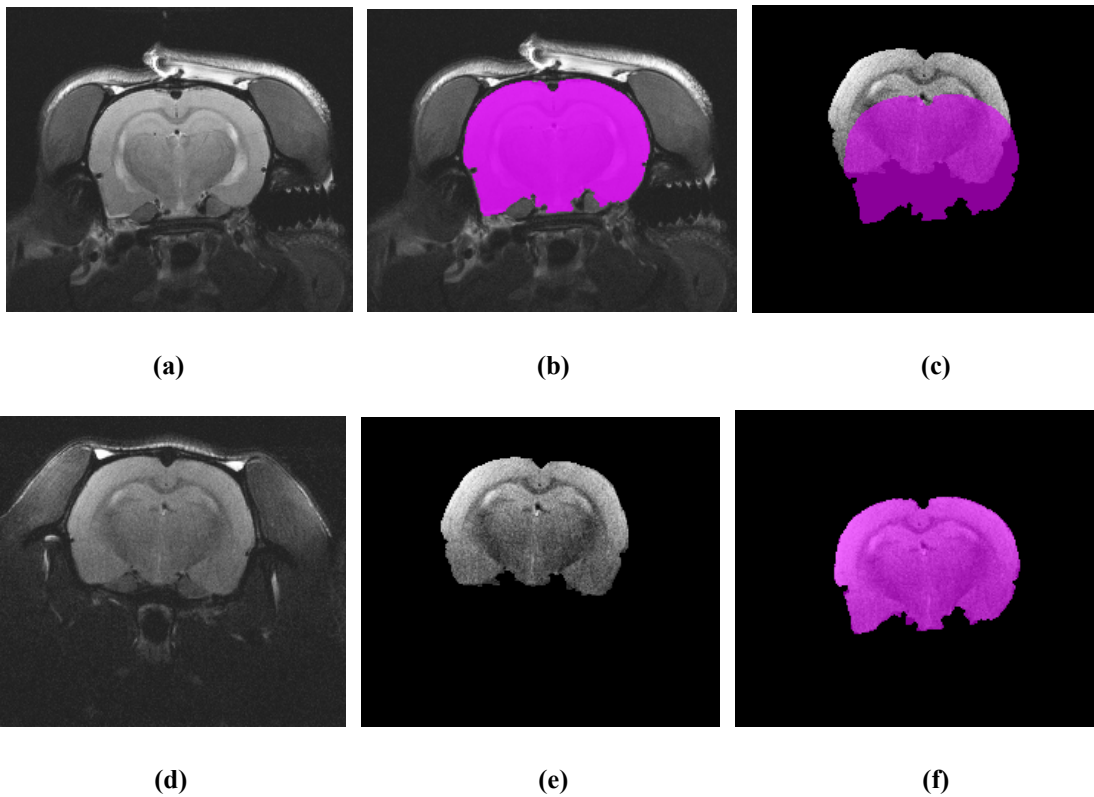
Figure 4-24　Elastic registration

(a) reference;　(b) reference mask (colored);　(c) initial misalignment;　(d) subject;　(e) cropped subject;

(f) cropped subject aligned to reference mask using linear elastic transform

Hereto each pixel within the cropped subject space has a one-to-one mapping within the reference mask space. Figure 4-24(f) shows the reoriented cropped subject image overlapped under the reference mask. Figure 4-25 shows the difference image [69][134] before and after elastic registration.

(a)   (b)
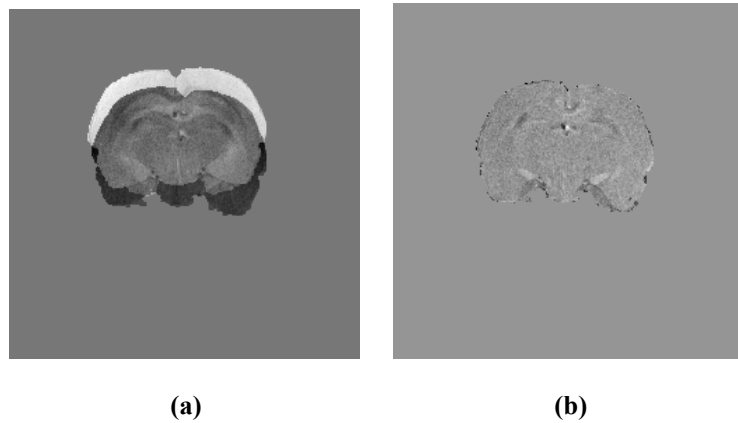
Figure 4-25   Difference image

(a) before elastic transform   (b) after elastic transform

4.4   A sample result

This elastic registration method using a finite element geometric model was tested on 8 intramodality MR image volumes of rat brains and 4 human brains. Table 4-1 shows the registration quality calculated by the sum of absolute pixel distance error (SAD) *Err*, compared to that of manual registration by a skilled user (gold standard) Err_{GS}. The alignment in the slice direction is performed by a time series matching, and the in-plane registration process is performed on a slice by slice basis via the finite element elasticity implementation. Figure 4-26 shows the registration result of two rat brains. On the left is the cropped subject volume set. The

middle column shows the initial misalignment of a cropped subject and the colored reference mask. On the right the representative cropped subject is aligned to the colored reference mask.

Table 4-1   Quality of linear elastic registration compared to gold standard (GS) and manual registration on nine rat brains and two human brains

Objects: R – rat brains; H – human brains;   Quality: in percents.

Objects	R-A	R- B	R-C	R-D	R-E	R-F	R-G	R-H	R-I	H-A	H-B
GS	100	100	100	100	100	100	100	100	100	100	100
Manual	99.8	100	99.7	98	97	96.7	95	99	100	100	97
FEM $\dfrac{Err}{Err_{GS}} \times 100\%$	98.2	100.3	97.6	96.9	98.3	98.3	98.0	99.2	94.5	99.1	99.3
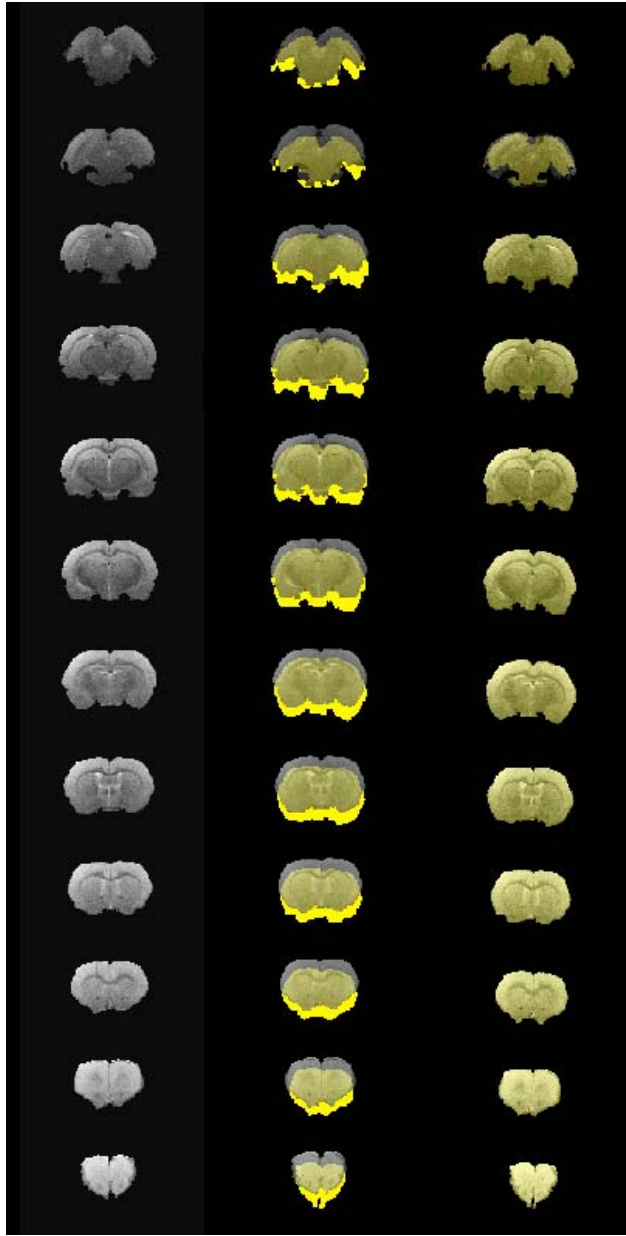
Figure 4-26　Elastic registration result based on finite element model

The results verified that mapping outline indices is a reliable approach for finding FEM boundary conditions. It does not require user defined landmarks. The drawback of this method is the accuracy of registration results is directly related to the accuracy of the image cropping.

5   VOLUME ALIGNMENT

The registration methods discussed in Chapter 3 and 4 were used to align numerous grayscale volume sets. These volume sets were generally cropped first by some strategy such as PCNN [19][81][91][165][167]. Subsequently, the volume geometry was created using a marching cube volume reconstruction strategy [85][86][92][175].

5.1   Volume reconstruction

5.1.1   Marching cubes algorithm

We use the marching cubes algorithm to build a surface mesh from a segmented 3D dataset. Marching cubes is a computer graphics algorithm that was first published in 1987 by Lorensen and Cline [175]. The algorithm proceeds through the voxels, taking eight neighbor locations at a time (thus forming an imaginary cube), then determining the polygon(s) needed to represent the part of the isosurface that passes through this cube. The individual polygons are then fused into the desired surface [134].

5.1.2   Removal of stair steps – linearization

Marching cubes algorithm has been widely used for three-dimensional boundary surface reconstruction from two-dimensional medical images. In 2001 Wu et al [173][174] developed a multiple material marching cubes algorithm (M3C) which extracts multiple material 3D surfaces within one sweep of 2D images. This robust tool eliminates numerous problems that are associated with lending single material image reconstructions into a unified model. However, it

too creates stair stepped geometries due to the common marching cubes interpolation mechanism [175]. Numerous post-processing smoothing efforts have been made but they either cause volume shrinkage, geometry alterations or are computationally expensive [3][78][120][3]. In 2003 we provided an efficient linearization strategy to remove the stair-steps that marching cubes algorithm generates [85][92]. This algorithm was applied on segmented rat brains [85][176], human breasts [176], human brains and other tissues [173]. It increased the accuracy of the model by an order of magnitude while preserving the volume and geometry integrity.
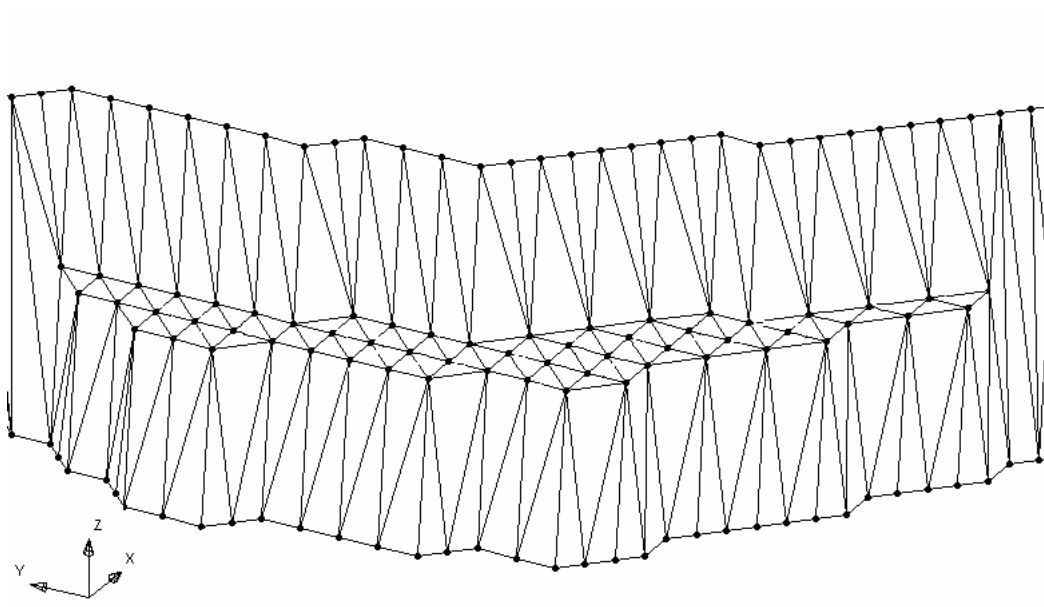
Figure 5-1   Triangles created between two layers from Marching Cubes algorithm

All marching cubes routines process a single layer between two medical image slices completely before moving to the next layer. Consequently, the linearization algorithm was built into the marching cubes and work within this layer processing level. At each level a unique set of triangles connects the two slices forming a belt or collar within the layer (Figure 5-1). Only edges exist directly on each slice. In the M3C case each triangle has the two materials it

separates identified. For the single material code, the triangle separates the desired material from any other material. A single sweep through the triangles created within the layer identifies a finite number of triangles that establish the surface separating a specific material combination. This subset of triangles can form an open or closed loop situation. This contiguous subset of triangles has termination edges on both slices (Slices A and B), no triangles exist on either slice.
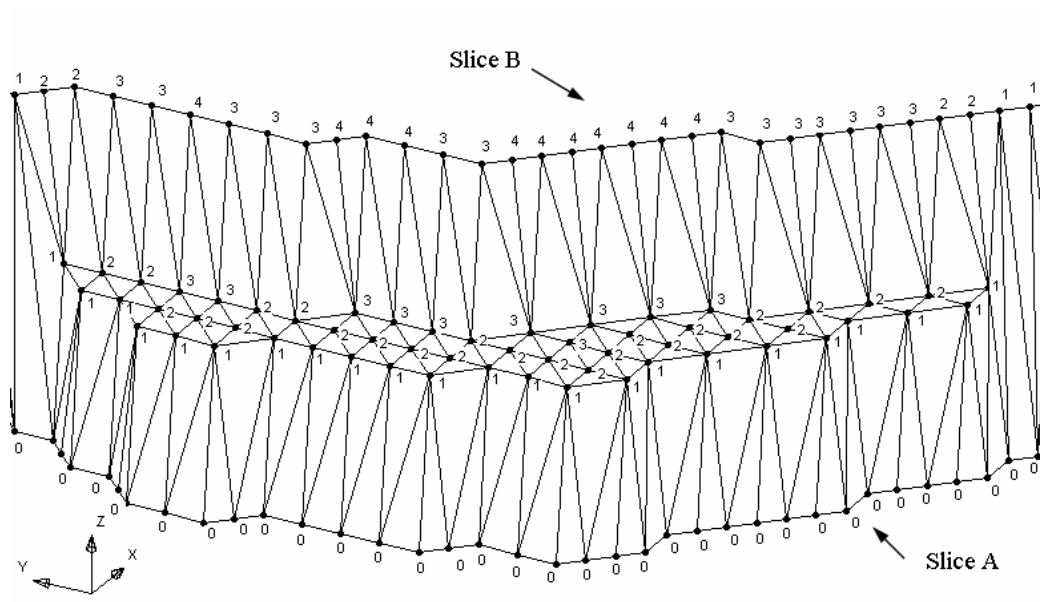
Figure 5-2   Each node within the mesh is numbered associated with the edge path from slice A to B

Beginning at the edges on slice A (by default) each node in the contiguous subset of triangles is tagged with two attributes M and N. N is the minimum number of steps required to reach slice B in an edge path containing the node, and M is the step location for this node on that path (Figure 5-2). With this information, the new z-coordinate (direction from slice to slice) of each node can be calculated by

$$z = (1 - \frac{M}{N})z_A + \frac{M}{N}z_B$$

where z_A and z_B are the z coordinates of level A and B, respectively. This edge-path creation strategy eliminates a variety of problems associated with other mathematical strategies; problems such as indeterminate path directions, multi-valued functions, and capping situations whenever a specific material is not encountered within an adjacent slice. This linearization algorithm is applied to the z direction only so each triangular facet retains its integrity.

This linearization strategy is fast, robust and it retains the surrounded volume of geometry well. Figure 5-3 shows a sphere created by marching cubes. The right half of the sphere is generated by conventional marching cubes and the left half is generated with linearization strategy. Figure 5-4 shows a segmented rat brain created by M3C with and without linearization.
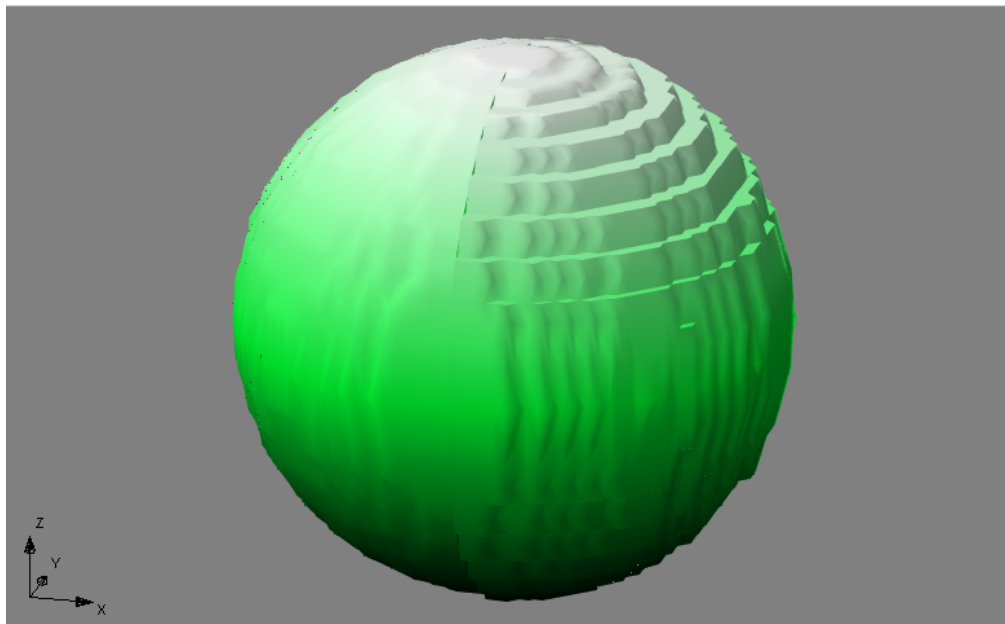
Figure 5-3   Sphere created by Marching Cubes with and without linearization
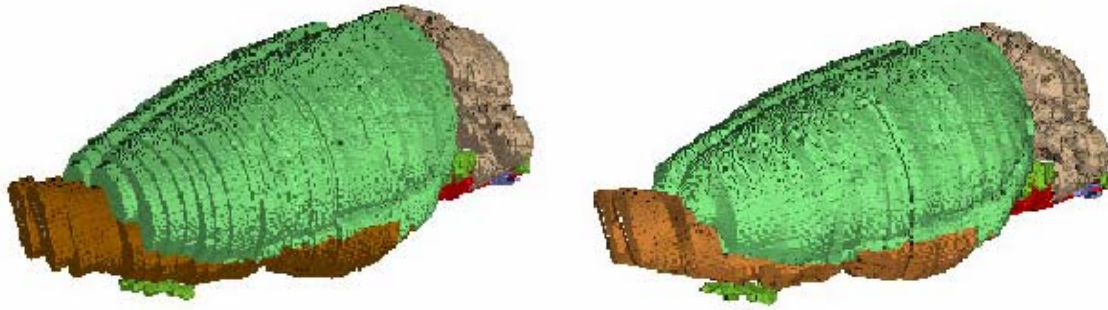
a) Stair-stepped geometry without linearization   b) Linearized geometry with stair steps removed

Figure 5-4   A segmented rat brain created by M3C with linearization

5.1.3   Volume reconstruction

Using the marching cubes algorithm with linearization option, 3D surfaces of the tissue of interest can be created.   Figure 5-5 shows a human brain surface mesh created from a $256 \times 256 \times 12$ MRI volume by the marching cubes algorithm.
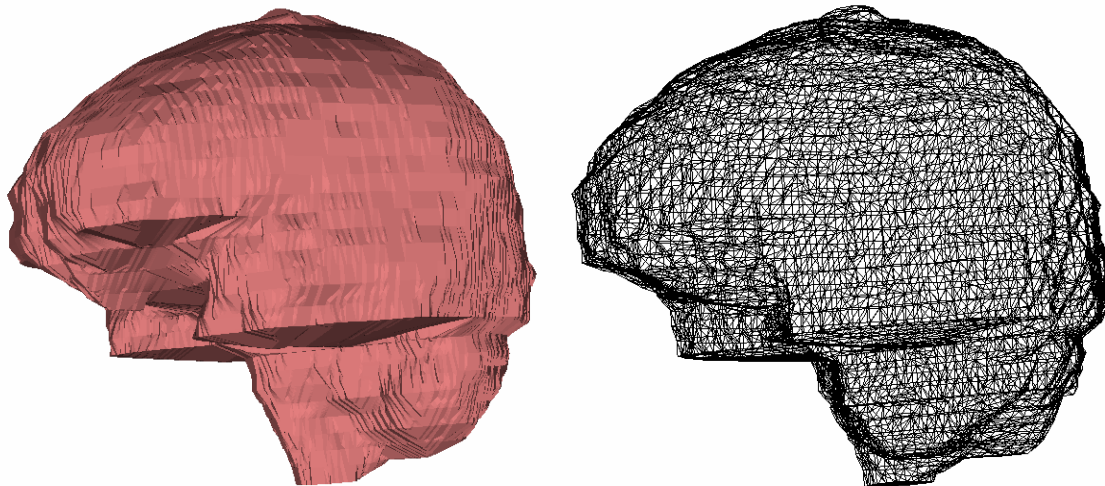
a) Surface   b) Mesh

Figure 5-5   Female human brain surface mesh created from MRI by marching cubes with linearization

5.2   Volume registration

In chapter 3 and 4 we presented two registration strategies that used affine and elastic transform methodologies, respectively.   Both strategies can be applied on segmented images.   Once each slice of an image set is fully segmented, the marching cubes algorithm can be used to create the registered volume of the subject, thus providing a 3D volume alignment.

The framework of this process is shown in Figure 5-6.   Figure 5-7 shows a rat brain surface created before and after its MR image set is registered to the reference.
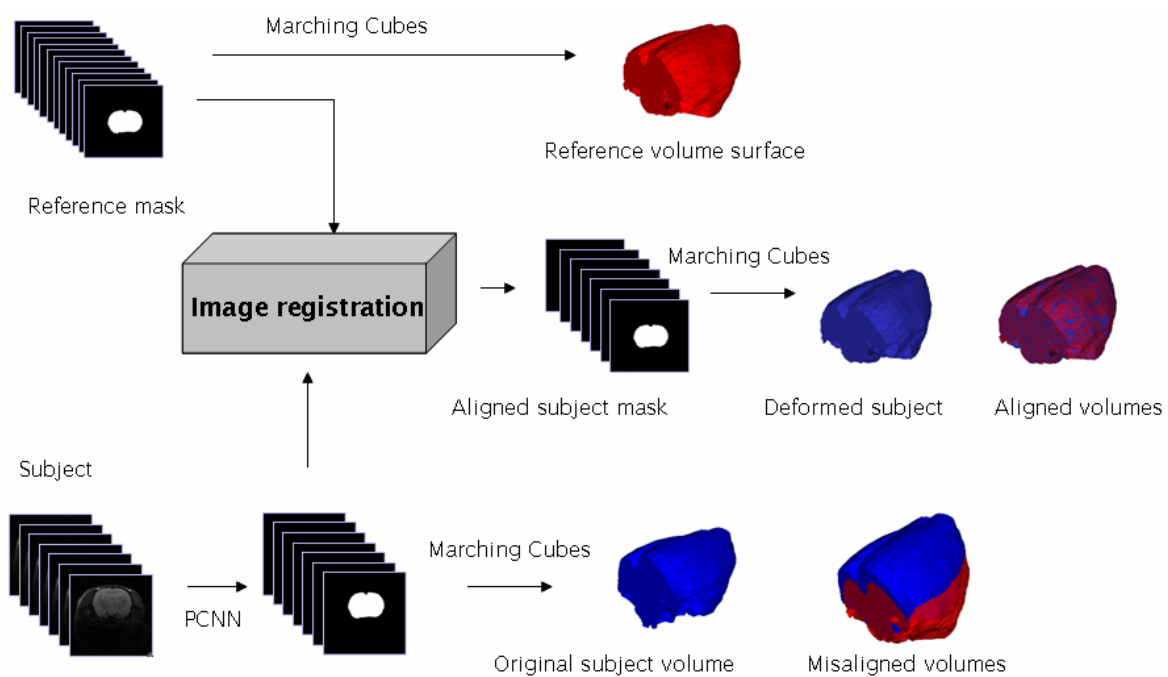
Figure 5-6   Framework of volume alignment
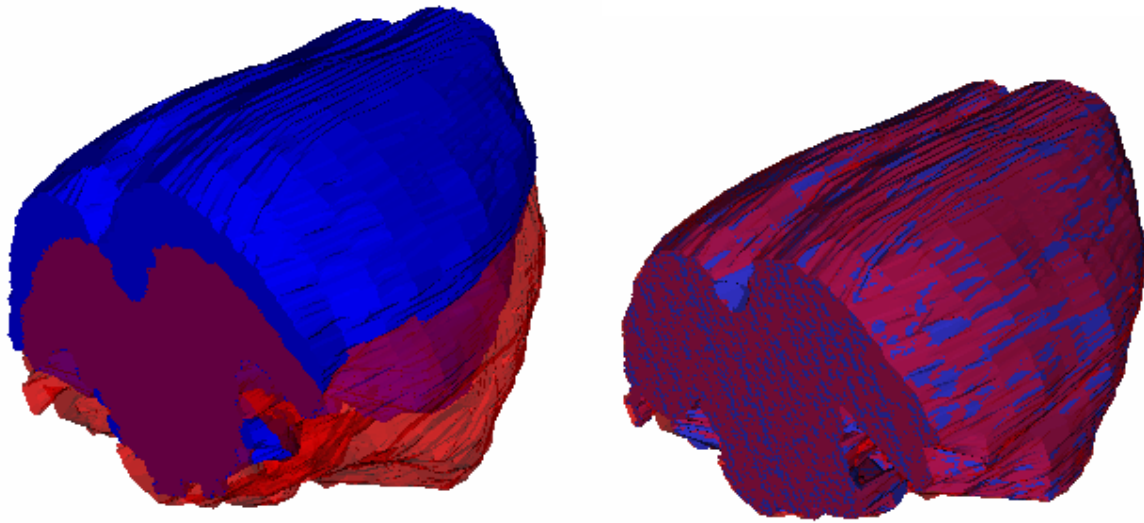
Red: reference   **Blue: subject**

(a) Subject volume created from unregistered image   **(b) Subject volume created from registered image**

Figure 5-7   Rat brain volume alignment

6   RESULTS

The previous chapters described the theory and implementation details of different strategies of affine registration using Genetic algorithm and the linear elastic model based on finite element model. In this chapter numerous registration results are presented for a broad range of MR images: a) rat brain images using a fast-spin echo on a 4.7T Bruker magnet system from the University of Massachusetts Medical School, b) breast images using a 1.5T GE Magnet and c) human brain images from Insight MRI. Intensity error and computing time is used to evaluate the registration results. In addition to the methods that are presented in this dissertation, manual registration and AIR package (Automated Image Registration) [95] are used for comparison.

6.1   Summary of terms

GS – gold standard, performed by skilled user in registration

Manual – performed by technically qualified user, but not an expert at registration

AIR – performed by AIR package

GA1 – one slice in-plane rigid body Genetic Algorithm with 3 chromosomes, applied to all slices

GA2 – in-plane rigid body Genetic Algorithm applied on each slice with 3 chromosomes followed by two scaling factors, N transformation matrices applied individually on each of the N slices

GA3 – affine transformation with 8 chromosomes applied simultaneously to the whole volume set

GA4 – Sequential Genetic algorithm registration, 8 chromosomes applied sequentially

FEM1 – 2D linear elastic transform based on FEM model

FEM2 – individual application of linear elastic transform based on FEM model on each pair of slices matched by slice alignment method

Accuracy – the quality of a registration compared to the gold standard (GS), calculated in pixel intensities by: $\frac{(orig - reg)}{(orig - GS)} \times 100\%$

R-A, R-B, … R-I – rat brain subjects A, B, … I

R-R – rat brain reference image

B-A, B-B, B-C – breast images A, B, C

B-R – breast reference image

H-A, H-B, H-C – human brain subjects A, B, C

H-R1 – human brain reference image acquired in sagittal orientation

H-R2 – human brain reference image acquired in axial orientation

6.2   Genetic algorithm

Different GA registration heuristics were tested on numerous images of rat brains (abbr. R), breasts (abbr. B) and human brains (abbr. H), illustrated in chapter 3. Source image information is listed in Table 6-1. Computing time and registration quality compared to other strategies is listed in Table 6-2. The operation time of AIR listed in Table 6-2 does not include the time for pre-threshold settings. Additionally, AIR failed to converge on a few examples. Although sometimes our registration algorithms present slightly lower quality than other manual or semi-automatic methods, our algorithms do not require any user interruption.

Table 6-1   Source image information

Image	Orientation	Dimension	FOV (mm)	Data Type	Endian
R-R	Axial	256x256x12	30x30x14.4	16 bit	Little
R-A	Axial	256x256x12	30x30x14.4	16 bit	Little
R-B	Axial	256x256x12	30x30x14.4	16 bit	Little
R-C	Axial	256x256x12	30x30x14.4	16 bit	Little
R-D	Axial	256x256x12	30x30x14.4	16 bit	Little
R-E	Axial	256x256x12	30x30x14.4	16 bit	Little
R-F	Axial	256x256x12	30x30x14.4	16 bit	Little
R-G	Axial	256x256x18	30x30x18	16 bit	Big
R-H	Axial	256x256x18	30x30x18	16 bit	Big
R-I	Axial	256x256x14	30x30x16.8	16 bit	Little
B-R	Axial	256x256x84	180x180x126	16 bit	Little
B-A	Axial	256x256x42	180x180x84	16 bit	Little
B-B	Axial	256x256x39	200x200x78	16 bit	Little
B-C	Axial	256x256x78	220x220x117	16 bit	Little
H-R1	Sagittal	256x256x124	256x256x186	16 bit	Little
H-R2	Axial	256x256x78	220x220x117	16 bit	Little
H-A	Sagittal	256x256x20	340x340x120	16 bit	Little
H-B	Axial	256x256x20	192.5x220x120	16 bit	Little
H-C	Axial	256x256x20	220x220x120	16 bit	Little

Table 6-2   Comparison among different registration methods

$$(\text{Time: minutes} \quad \text{Accuracy:} \frac{(orig - reg)}{(orig - GS)} \times 100\%)$$

		GS	Manual	AIR	GA1	GA2	GA3	GA4	FEM1	FEM2
R-A	**CPU time**	8	30	30	8	350	150	70	15	210
	Accuracy	100%	99.8%	97.4%	97.4%	97.4%	97.4%	97.7%	97%	96.7%
R-B	**CPU time**	5	22	25	5	280	100	45	10	140
	Accuracy	100%	100%	98%	97.7%	97.7%	97.7%	97.7%	99.1%	97.1%
R-C	**CPU time**	5	25	27	5	290	135	60	11	160
	Accuracy	100%	99.7%	96.7%	96%	96%	96%	96.5%	98.7%	98.7%
R-D	**CPU time**	4	25	Failed	5	360	105	45	12	180
	Accuracy	100%	98%	N/A	93.5%	93.5%	93.5%	94%	99.4%	99.4%
R-E	**CPU time**	5	28	33	7	350	130	50	16	200
	Accuracy	100%	97%	98.6%	95.4%	95.4%	95.4%	96.7%	97.6%	97.6%
R-F	**CPU time**	7	35	Failed	10	320	140	55	18	220
	Accuracy	100%	96.7%	N/A	93%	96%	95%	94.5%	95%	96.8%
R-G	**CPU time**	5	30	25	7	280	105	46	15	195
	Accuracy	100%	95%	97.5%	94.7%	95%	97.5%	93.6%	95%	95.5%
R-H	**CPU time**	5	32	25	6	280	100	45	17	230
	Accuracy	100%	99%	97.7%	93.5%	93.6%	94%	93%	93.5%	93.5%
R-I	**CPU time**	5	35	32	4	250	120	50	15	200
	Accuracy	100%	100%	92%	95%	97.2%	89.9%	91%	93%	97%
H-A	**CPU time**	10	35	Failed	10	500	295	130	13	320
	Accuracy	100%	100%	N/A	90%	92%	92.2%	91%	95%	93%
H-B	**CPU time**	8	25	45	24	540	225	118	10	280
	Accuracy	100%	97%	90%	92%	92%	92%	94.5%	95%	95%
H-C	**CPU time**	8	30	40	20	480	250	120	10	300
	Accuracy	100%	99.2%	91%	92.7%	92.7%	92.7%	95%	97.5%	95%

6.2.1   In-plane rigid body transformation of one slice applied to all slices

Pick one slice (usually the middle slice in subject image), perform in-plane rigid body Genetic Algorithm with 3 chromosomes, and apply the registration matrix to all slices. The result of a rat brain alignment is shown in Figure 6-1. Figure 6-2 shows Sagittal human brain image registered to the VHP (NIH, Visible Human Project [181]) image cropped by a sub window.

6.2.2   In-plane affine transformation of one slice applied to all slices

In-plane rigid body registration is applied by Genetic Algorithm on each slice followed by two scaling factors. N transformation matrices are applied individually on each of the N slices. Figure 6-3 shows the registration of a rat brain and Figure 6-4 shows a human brain alignment with an axial orientation.

(a) initial misalignment   (b) registered by GA1
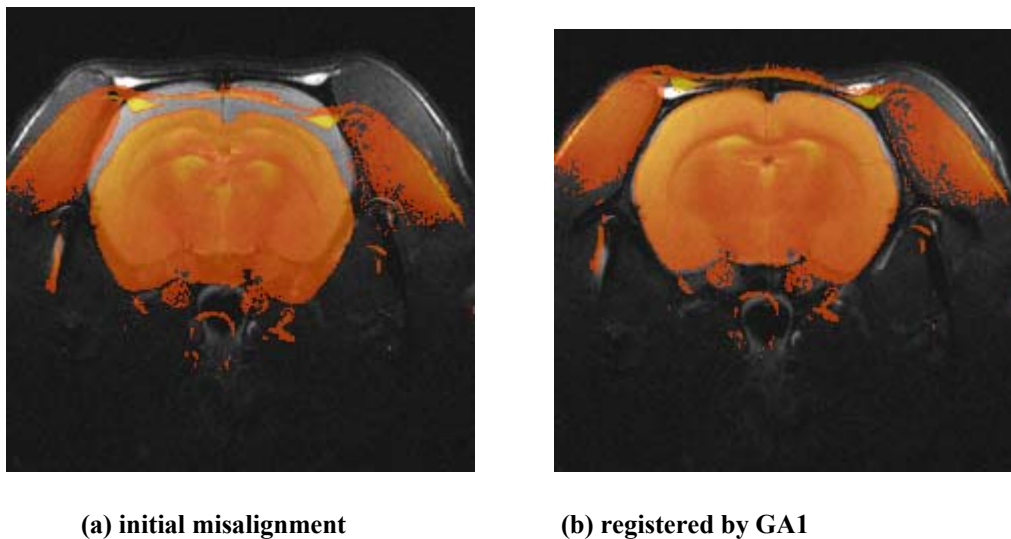
Figure 6-1   Rat brain R-A registered to R-R by GA1
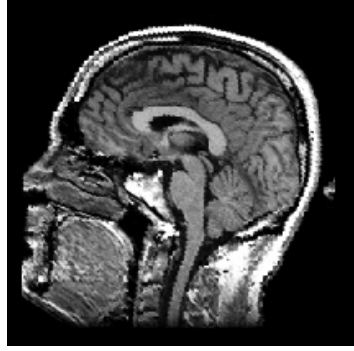
(a) Reference
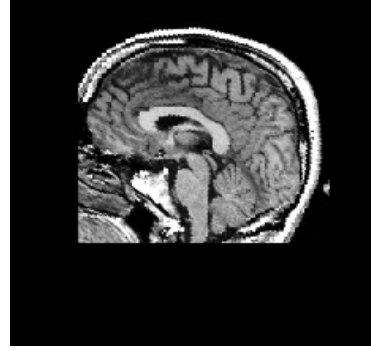
(b) Cropped reference
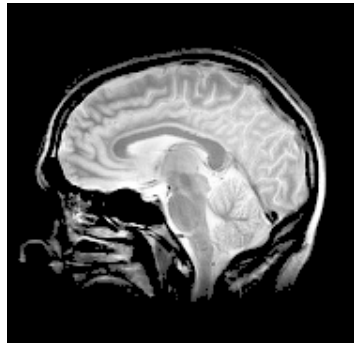
(c) Subject
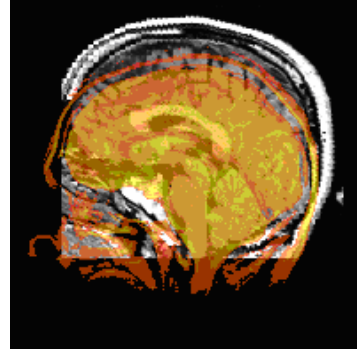
(d) Initial misalignment
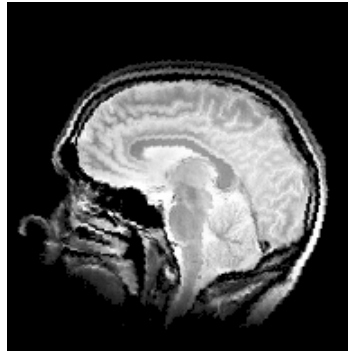
(e) Transformed subject
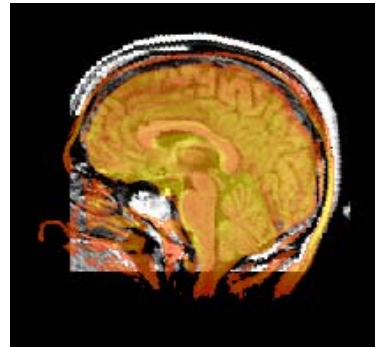
(f) Subject aligned to reference

Figure 6-2   Human brain H-A registered to H-R1
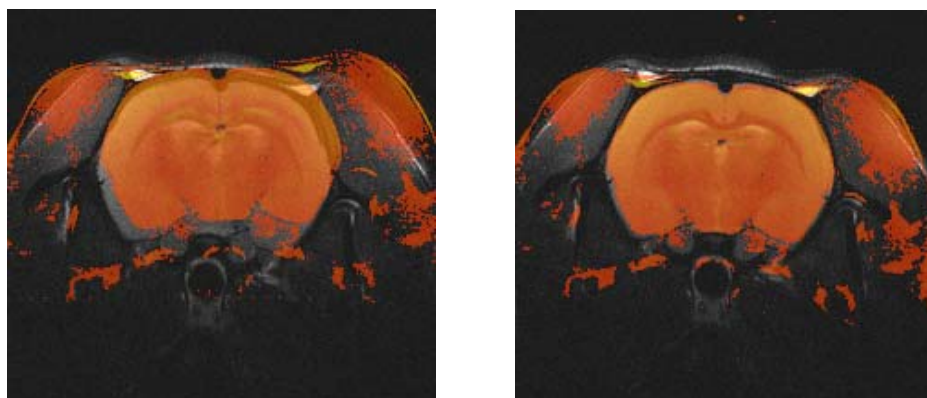
| (a) Initial misalignment | (b) Registered by GA2 |

Figure 6-3   Rat brain R-B registered to R-R by GA2
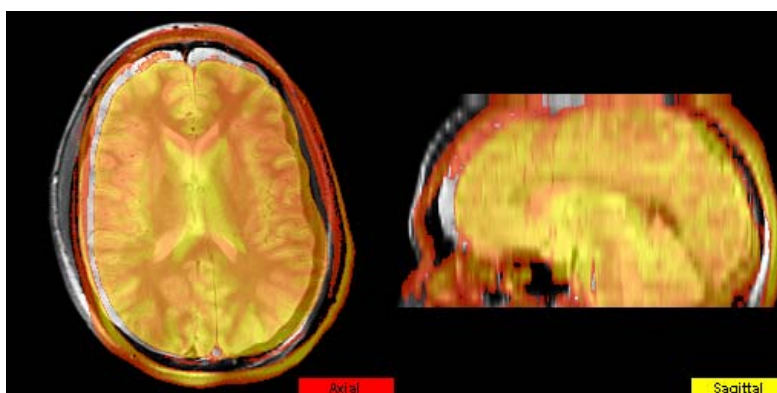
(a) Initial misalignment
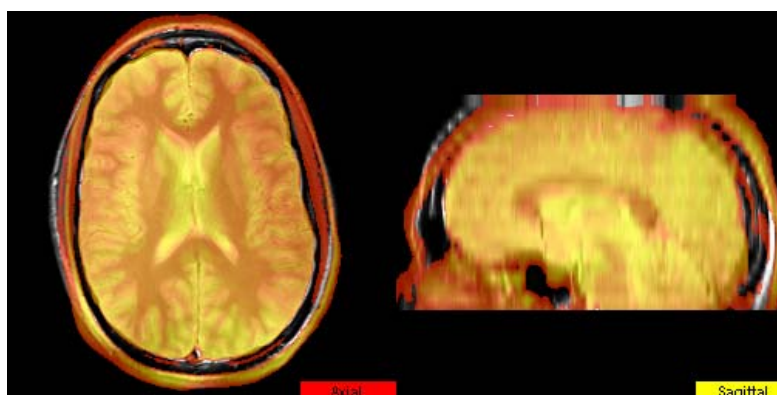
(b) Subject aligned to reference

Figure 6-4   Human brain H-B registered to H-R2 by GA2

6.2.3　Simultaneous GA affine registration GA

The affine transformation matrix is obtained by 8 GA chromosomes applied simultaneously. This transformation matrix is applied to the whole volume set. Figure 6-5 and 6-6 show the results of this GA registration applied on a rat brain and a human brain, respectively.
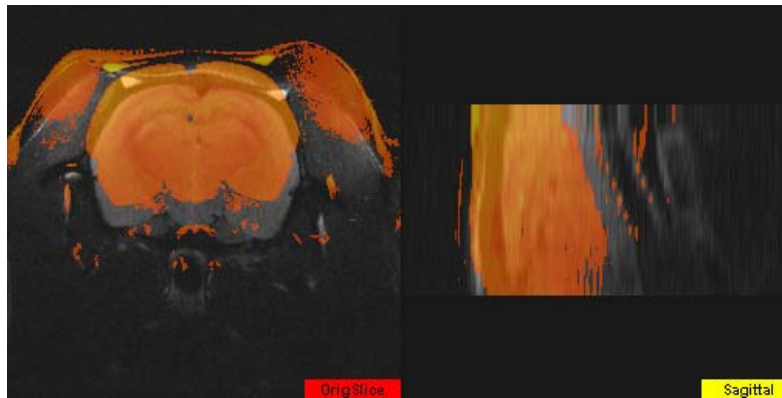
(a) Initial misalignment
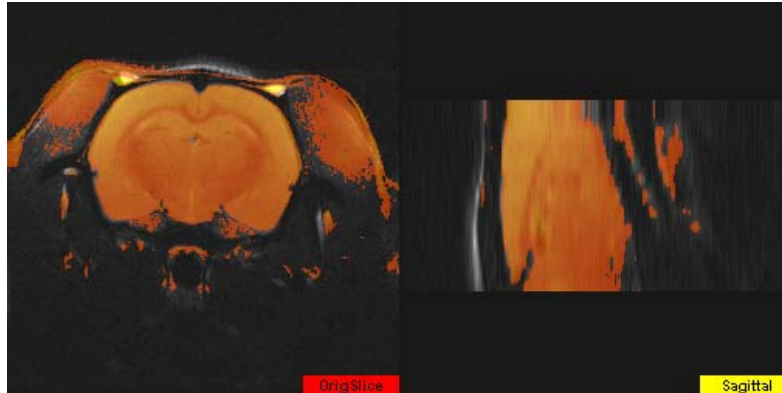
(b) Registered by GA3

Figure 6-5　　Rat brain R-C registered to R-R by GA3
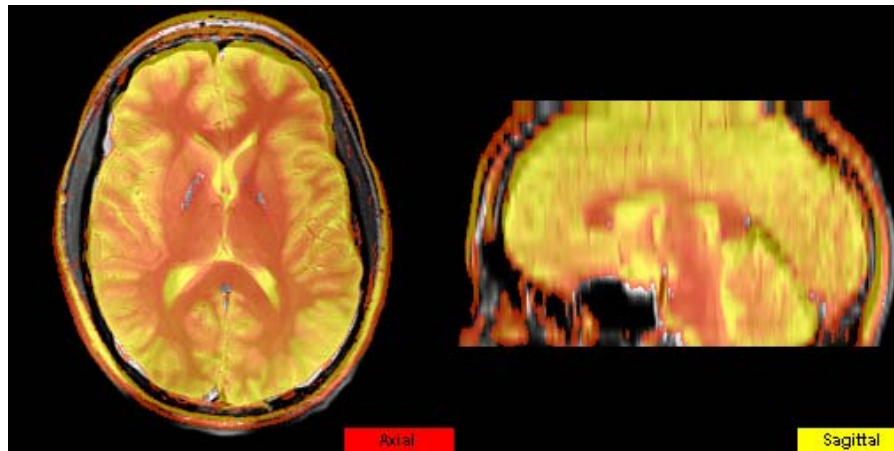
(a) Initial misalignment
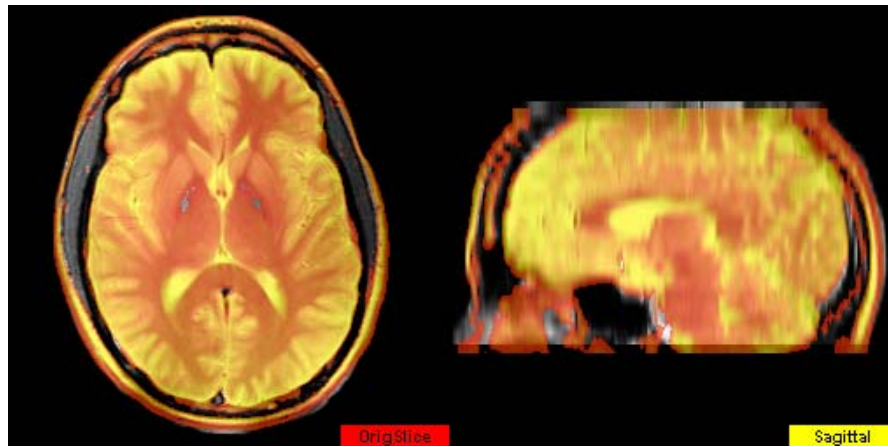
(b) Subject aligned to reference

Figure 6-6   Human brain H-C registered to H-R2 by GA3

6.2.4   Sequential GA

User picks up a subject slice (usually a middle slice), and applies an in-plane translation and rotation. Subsequently, in-plane scaling is performed if necessary. Then a translation in the slice direction is applied to match the sagittal orientation. Finally, if necessary, the subject is rotated

about the anterior-posterior and left-right axes. Some results of sequential GA registration are shown in Figure 6-7 and 6-8.
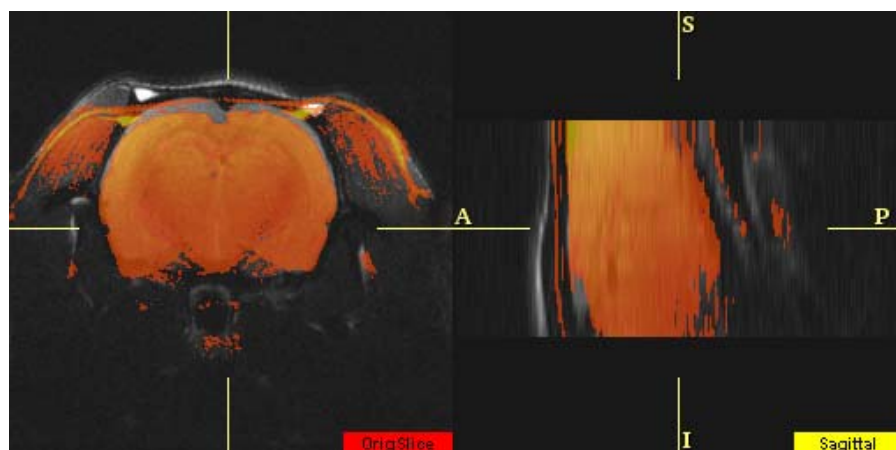
(a) Initial misalignment
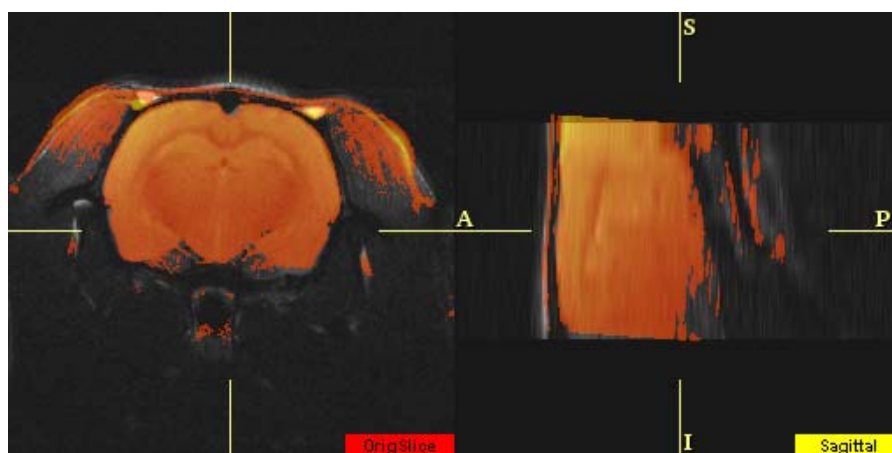
(b) Registered by GA4

Figure 6-7   Rat brain R-E registered to R-R by GA4
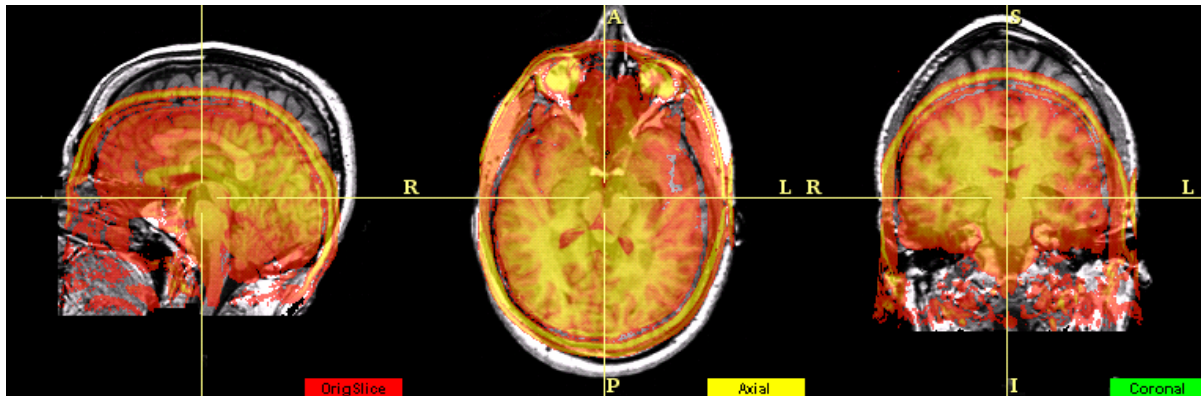
(a) Initial misalignment
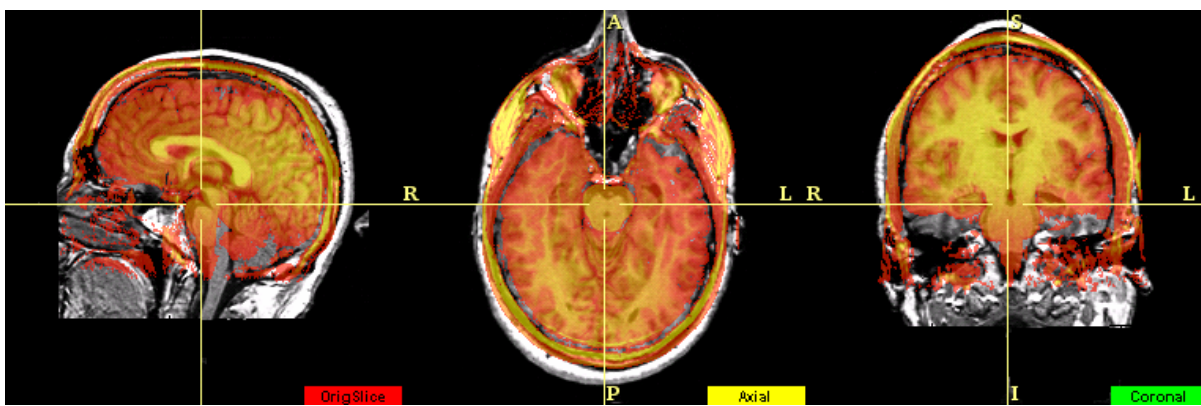
(b) subject registered to reference

Figure 6-8   Human brain H-A registered to VHP image by GA4

6.2.5   Failures

Although GA registration works well for most of our test images, it showed poor registration quality on breast images, e.g. Figure 6-9. The reason is breast images vary significantly from each other and the deformation of breast tissue does not follow an affine mode.
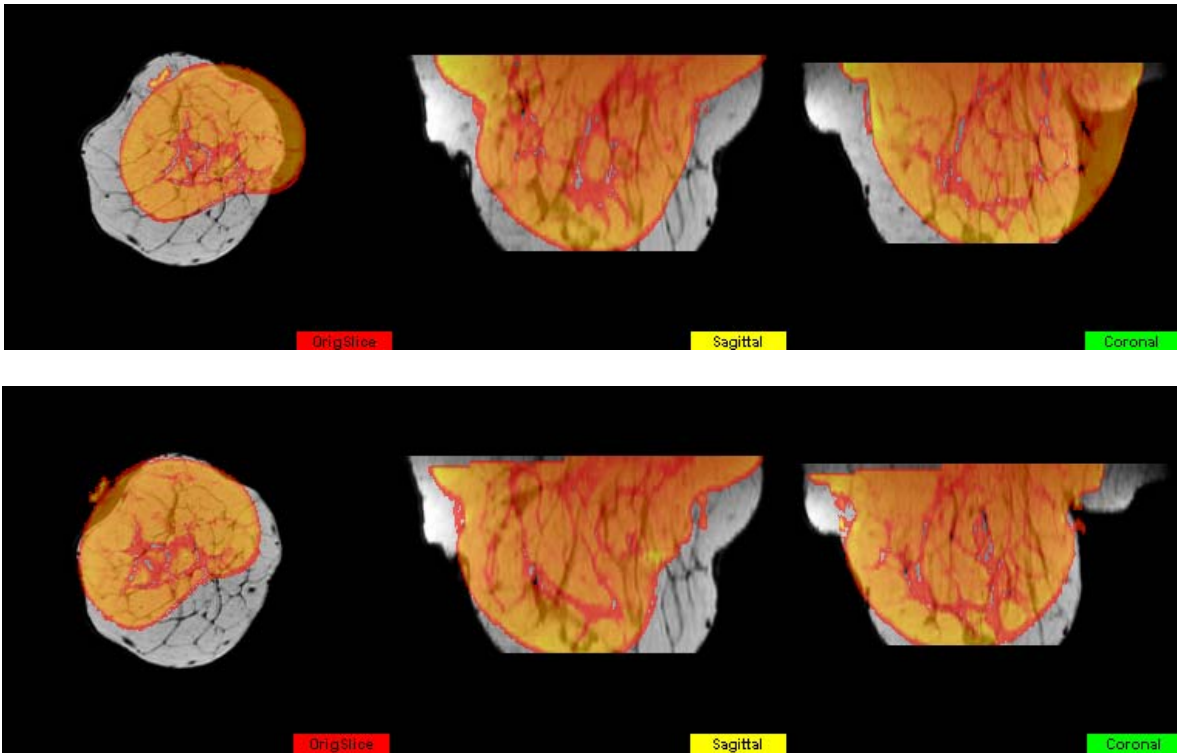
Figure 6-9   GA fails to register breast images

6.3   Elastic model

Numerous examples were used to test the elastic model using a finite element formulation. The FEM registration results of images listed in Table 6-1 are shown in Table 6-2 (items 2D FEM and 3D FEM). The registration error was calculated based on the cropped grayscale images of both reference and subject. Note that some registration qualities are better than the gold standard. This is because the manual registration we performed here for the gold standard is based on an affine transformation and no elastic deformation is applied. Also, when user is performing registration, the error is completely based on user's visual judgment, which can be inaccurate. The result demonstrated that an elastic transformation worked well for these soft tissues such as brains and breasts and provides an overall better alignment.

6.3.1 Implementation on rat brains

Figure 6-10 presents the elastic registration results on a rat brain. The bright colored region is the mask of the reference, and the grayscale is the copped subject.
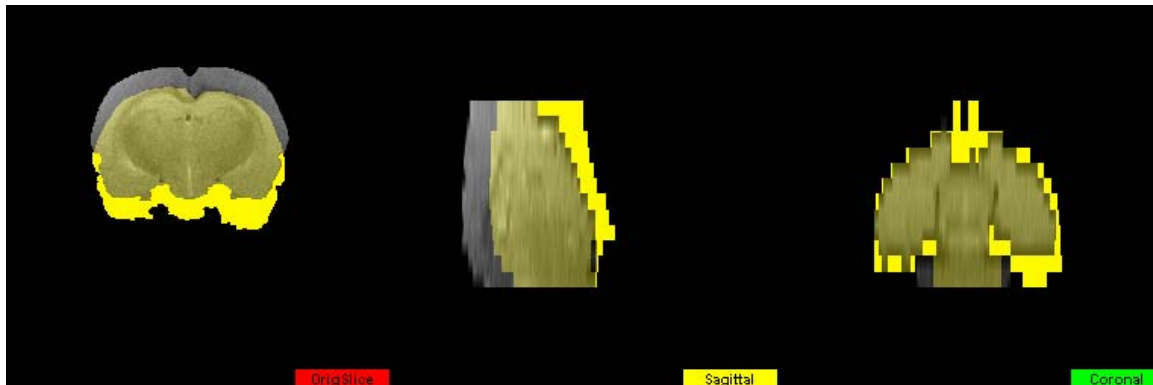
(a) Initial misalignment of reference mask and cropped subject volume
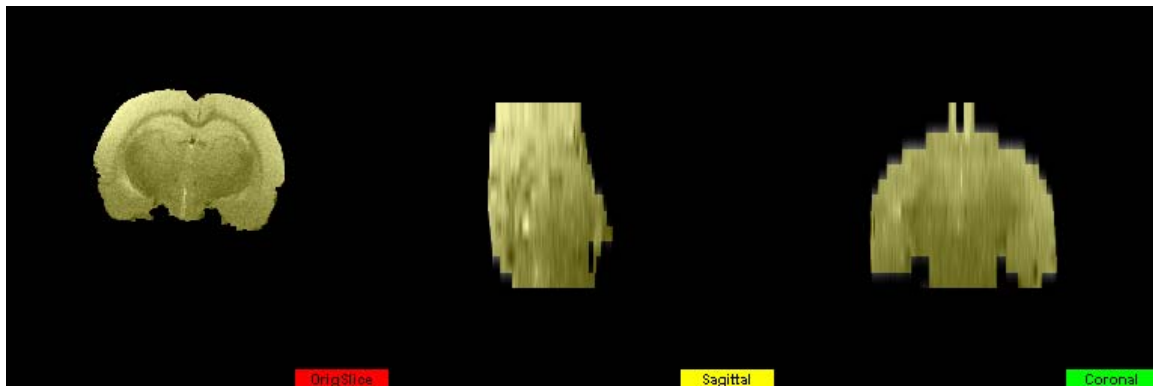
(b) Subject R-C registered to reference R-R mask

Figure 6-10   3D FEM registration applied on rat brain images

6.3.2 Implementation on human brains

Figure 6-11 presents the cropped volume of a female human brain aligned to the mask of a male brain using the FEM linear elastic model.
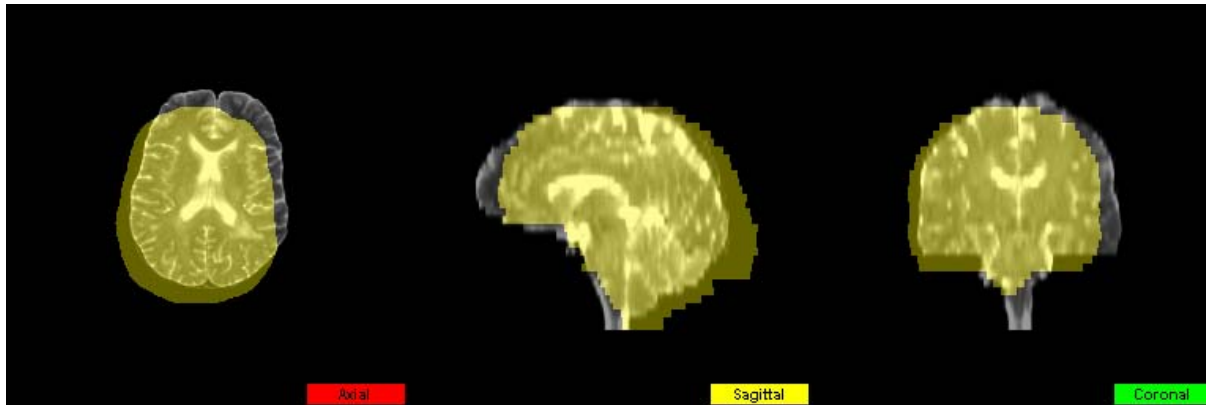
(a) Initial misalignment of reference mask of a male and cropped subject volume of a female
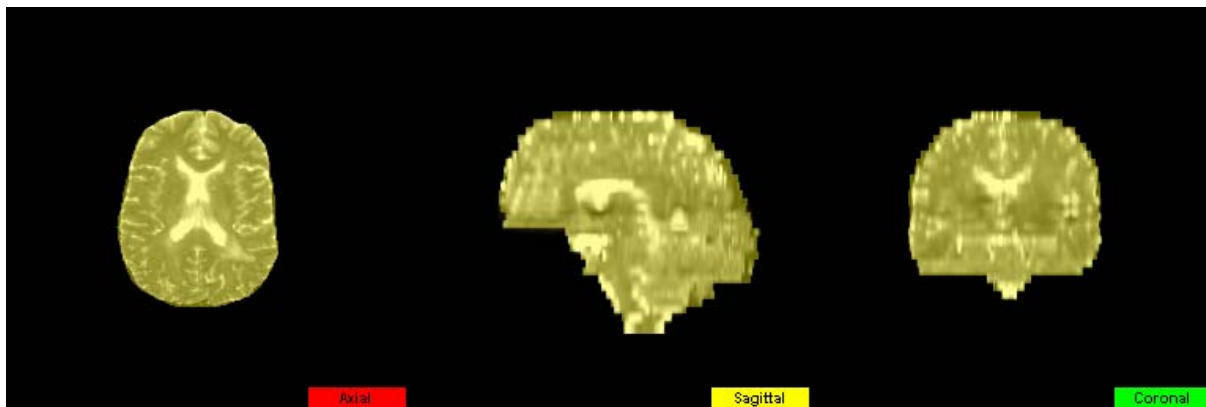
(b) Cropped female volume registered to the male's mask

Figure 6-11   3D FEM registration applied on human brain images (a female aligned to a male)

6.3.3   Failures

The linear elastic registration is based on a contour perimeter mapping. Section 4.3.3 illustrated how two contours are matched to provide a boundary mapping for the elastic model. Since the breast image examples we used are in the axial orientation and the circular shape is not rotation invariant, it is hard to map two axial breast contours (Figure 4-16). Therefore, elastic model did not work for axial breast images. Currently manual registration is the only successful way to align axial breast images.

6.4 Co-registration

The registration strategies were for intra-modality alignments. Once a subject is aligned to a standard or reference volume set of the same imaging modality, an inter-modality alignment is still required to overlay a color-coded atlas. A sequential registration strategy was developed to overcome this problem [182] in the software MIVA (Medical Image Visualization and Analysis) [32][96]. Once an intra-registration method (GA or FEM) is applied to N subjects, a predetermined transformation matrix that originally aligned the atlas and reference volume can be applied to the transformed individual subjects. a MRI reference atlas (intra registration), which is aligned to a segmented reference atlas (inter registration). Details will be discussed in section 6.4.1 and 6.4.2. Consequently, the N subjects are aligned to the segmented atlas. All regions of the N subjects are segmented and a full functional MRI (fMRI) analysis is possible [32][182]. Details about fMRI are shown in Appendix I.

6.4.1 Intra modality registration

The goal of intra registration is to align multiple subjects to the standard subject (Figure 6-12). One of N subjects is designated as the standard and all the other (N-1) are aligned to this standard via one of our registration strategies.

$$\{Standard\} = [T_{Subject\text{-}to\text{-}Standard}]_j \{Subject\}_j$$

where j=1 to N-1.
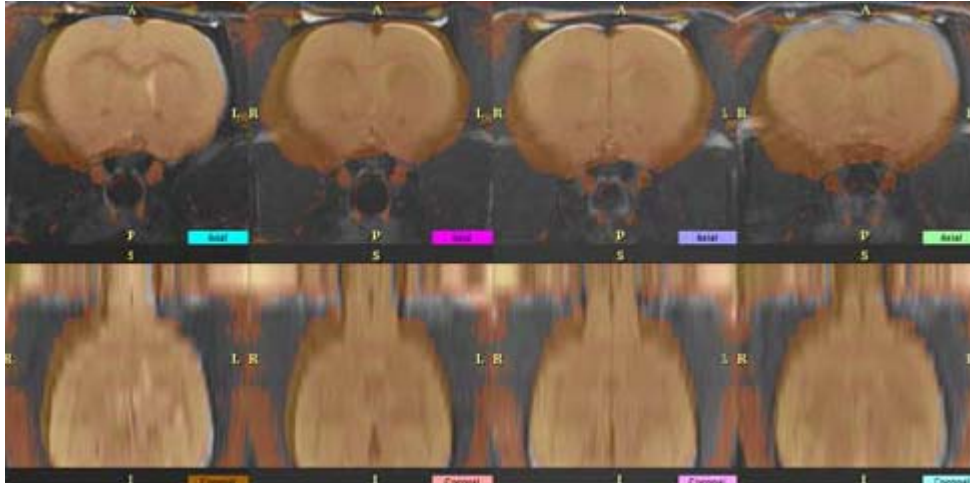
Subjects before registration
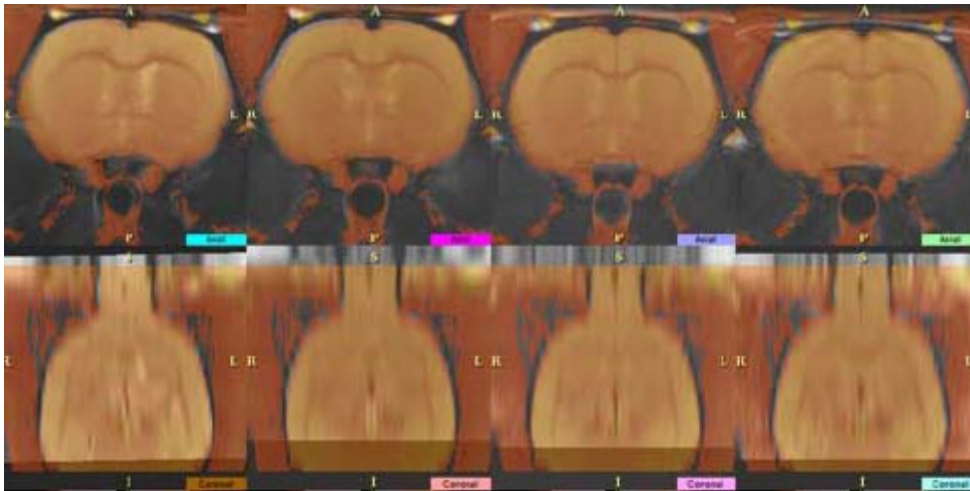
Subjects after registration

Figure 6-12   Intra modality registration – four subjects are alignment to the standard subject [182]

6.4.2   Inter modality registration

After the intra registration, the standard subject is aligned to segmented atlas (Figure 6-13). This step is generally performed manually or via some semi-automatic methods such as Landmarks [33][34].

$$\{\text{Atlas}\} = [\text{T}_{\text{Standard-to-Atlas}}]\{\text{Standard}\}$$

By multiplying $T_{\text{Subject-to-Standard}}$ and $T_{\text{Standard-to-Atlas}}$ (Merge registration), the N subjects are registered to the segmented atlas.

$$\{\text{Atlas}\} = [T_{\text{Subject-to-Atlas}}]_j \{\text{Subject}\}_j$$

$$[T_{\text{Subject-to-Atlas}}]_j = [T_{\text{Standard-to-Atlas}}][T_{\text{Subject-to-Standard}}]_j$$

where j=1 to N.
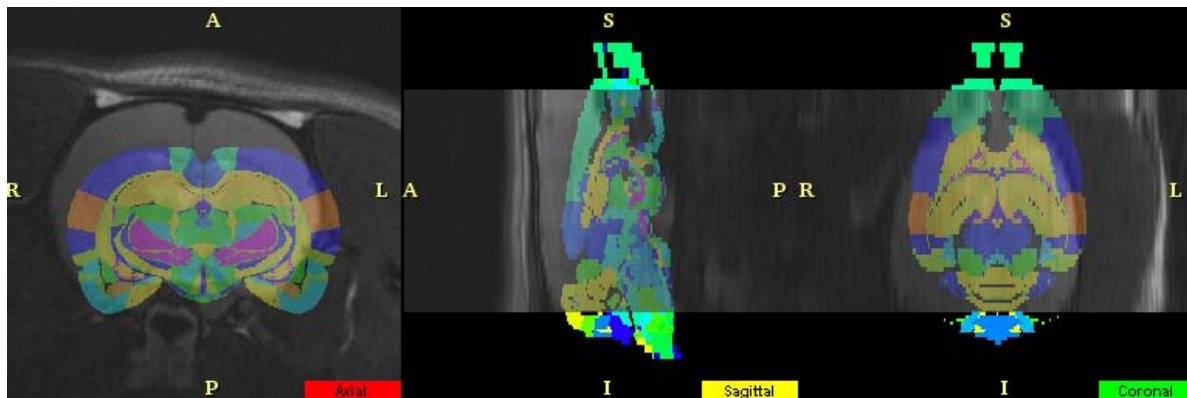
Before registration
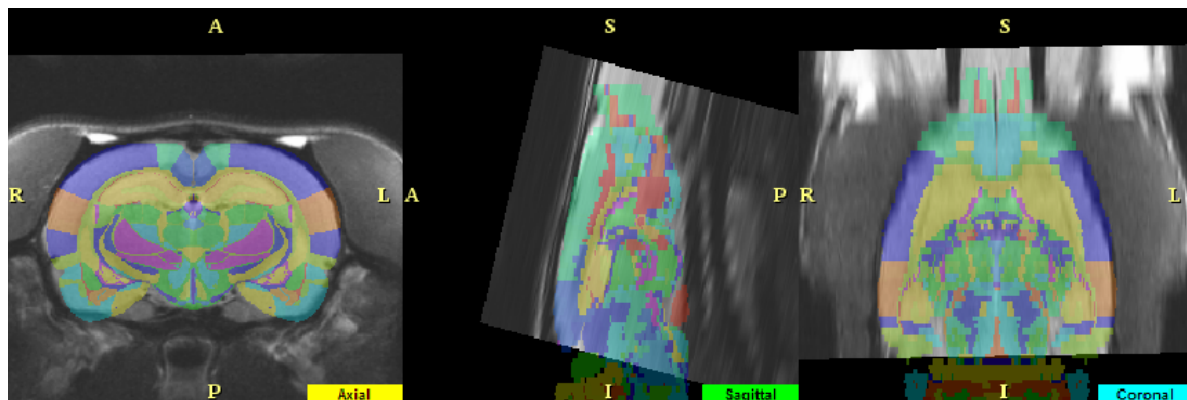
After registration

Figure 6-13   Inter modality registration – standard subject is aligned to atlas

7   CONCLUSIONS

This dissertation work developed automated affine and deformable registration methods for medical images. Numerous MRI examples were used to test the performance of the registration algorithms. Three groups of volumes were studied: rat brains, human brains, and human breasts. The breast tissue was highly erratic with substantial differences from one subject to another. Consequently, the registration strategies presented did not succeed. Manual registration is currently the only successful alignment methodology in use today. The brain volumes had significantly more internal structures within them that were consistent from one subject to another. In these situations the automated registration routines performed well.

7.1   Genetic algorithm

One of the approaches developed was the automatic affine registration based on Genetic Algorithm (GA). Advances of our GA approach included: a) retention of high ranked parents; b) incorporating a mutation avenue that prevents cloning; c) introduction of sequential GA routine to mimic those sequences of skilled manual alignments. Numerous experiments demonstrated these strategies. Significant improvements in actual time were realized with these advanced GA implementations.

A key advantage of the GA approach for image registration is that it does not require any pre-alignment. It starts with a random result and does not require a user-specified start location.

However, if a certain area of the image is more of interest, then an image pre-cropping can enhance the registration accuracy.

The disadvantage of GA is that it is very time consuming in nature. We provided a sequential genetic algorithm which mimics the path an expert manually aligns images by sequentially solving the GA parameters in groups due to their significance in the transformation matrix. Experiments showed this strategy can speed up the registration process by 30% in average.

7.2   Linear elastic model

For alignments of soft tissues beyond the typical homogeneous 4x4 transformation matrix an elastic model was formulated and solved by the finite element formulation. Using the binary mask information automatically provided by a PCNN code, cropped images were created and sent to the elastic model. Slice alignment was implemented by matching slice series based on the header information of input images.

For each matched pair of reference and subject slices, the subject perimeter is oriented to match the reference based on a least-squared error analysis. The linear elastic formulation for plane strain is applied to the automatically created 2D Delaunay finite element mesh. Incremental displacements are applied as the boundary condition until the subject perimeter is tagged to the reference perimeter.

The elastic model is automatic and does not require user intervention. Results showed the method of mapping perimeters is an ideal and reliable approach to deciding boundary conditions for soft tissues with a rotation invariant shape that has a major axis such as brains. For circular shapes like breasts in the axial view, the subject perimeter cannot be orientated accurately to match the reference perimeter. Therefore this elastic model is not a good choice for aligning breast images.

Since an automatic segmentation PCNN extracts the region of interest from the original image before applying the elastic model, this registration approach eliminates the potential error caused by other regions and most noises in the image, therefore provides a more accurate elastic transformation. The perimeter mapping is completely automatic and does not require any use defined landmarks.

7.3   Future work

Some methods can be used in the future to increase the efficiency of GA algorithm such as parallel computing [27] or improved fitness function, etc.

Future work on the elastic model includes finding a valid approach to match circular perimeters, and considering more tissue properties and other types of finite element boundary conditions. Fluid deformation may also be applied.

REFERENCES

[1] Knesaurek, K. Ivanovic, M. Machac, J. Weber, D.A. (2000). Medical Image Registration. Europhysics News, 31(4), 5-8

[2] Antoine Maintz, J.B., Viergever, M.A. (1998). A Survey of Medical Image Registration. Medical Image Analysis, 2(1), 1-37

[3] Taubin, G. (1995). A Signal Processing Approach to Fair Surface Design. Proceedings of the 22nd annual conference on Computer graphics and interactive techniques, 351-358

[4] Zitova, B. and Flusser, J. (2003). Image Registration Methods: a Survey. Image and Vision Computing, 21(11), 977-1000

[5] Hill, D.L.G., Batchelor, P.G., Holden M. and Hawkes, D. J. (2001). Medical Image Registration. Physics in Medicine and Biology, 46(3), 1-45

[6] Woods, R.P., Mazziotta, J.C., Cherry, S.R. (1993). MRI-PET Registration with Automated Algorithm. Computer Assisted Tomography, 17(4), 536-546

[7] West, J., Fitzpatrick, J.M., Wang, M.Y., Dawant, B.M., et al. (1997). Comparison and Evaluation of Retrospective Intermodality Brain Image Registration Techniques. Journal of Comuter Assisted Tomography, 21(4), 554-566

[8] Goldberg, D.E. (1989). Genetic Algorithm in Search, Optimization and Machine Learning. Boston, MA, USA: Addison-Wesley Longman Publishing Co., Inc.

[9] Mitchell, M. (1996). An Introduction to Genetic Algorithms. MIT Press, Cambridge, MA

[10]   Rouet, J.M., Jacq, J.J. & Roux, C. (2000). Genetic Algorithms for a Robust 3-D MR-CT Registration. IEEE Transactions on Information Technology in Biomedicine, 4(2), 126-136

[11]   Rueckert, D., Sonoda, L.I., Hayes, C., Hill, D.L.G., Leach, M.O., Hawkes, D.J. (1999). Nonrigid Registration Using Free-form Deformation: Application to Breast MR Images. IEEE Transactions on Medical Imaging, 18(8), 712-721

[12]   Lin, K., Huang, S., Yu, D., Melega, W. Barrio, J.R. & Phelps, M.E. (1996). Automated image registration for FDOPA PET studies. Physics in Medicine and Biology, 41(12), 2775-2788

[13]   Fei, B., Wheaton, A., Lee, Z., Duerk J.L. & Wilson, D.L. (2002). Automatic MR volume registration and its Evaluation for the pelvis and prostate. Physics in Medicine and Biology, 47(5), 823-838

[14]   Whitley, L.D. (1993). Foundations of Genetic Algorithms 2. ISBN: 1558602631

[15]   Vose, M. D. (1999). the Simple Genetic Algorithm: Foundation and Theory. MIT Press, Cambridge, MA

[16]   Swanson, L.W. (1998). Brain Maps: Structure of the Rat Brain. (Second Edition). Amsterdam, the Netherlands: Elsevier Science B.V.

[17]   Paxinos, G. Watson, C. (1998). The Rat Brain in Sterotaxic Coordinates. Academic Press

[18]   Chow, C.K., Tsui, H.T. Lee, T. & Lau, T.K. (2001). Medical Image Registration and Model Construction Using Genetic Algorithms. Proceedings of International Workshop on Medical Imaging and Augmented Reality, 174-179

[19]   Atkins, M.S., Maskiewich, B.T. (1998). Fully Automatic Segmentation of the
Brain in MRI. IEEE Transactions on Medical Imaging, 17(1), 98-107

[20]   Brummer, M.E., Mersereau, R.M., Eisner, R.L., Lewine, R.R. (1993). Automatic
Detection of Brain Contours in MRI Data Sets. IEEE Transactions on Medical Imaging,
12(2), 153-166

[21]   Insight MRI (2007). Retrieved April 17, 2007, http://www.insightmri.com/

[22]   Metz, H., McElhaney, J. & Ommaya, A.K. (1970). A comparison of the elasticity
of live, dead, and fixed brain tissue. Journal of biomechanics, 3(4), 453–458

[23]   Kyriacou, S.K., Davatzikos, C., Zinreich, S.J., Bryan, R.N. (1999). Nonlinear
Elastic Registration of Brain Images with Tumor Pathology Using a Biomechanical Model.
IEEE Transactions on Medical Imaging, 18(7), 580-592

[24]   Gefen, A., Levchakov, A., Linder-Ganz, E., Margulies, S.S., Raghupathi, R.
(2005). Strain Distribution in Brain Tissue of Rats Subjected to Closed Head Injury is Age-
Dependent.

http://www.eng.tau.ac.il/~msbm/list_of_publications/Refereed_Conference_Proceeding/b00
35381.pdf

[25]   Mortenson, M.E. (1985). Geometric Modeling. John Wiley & Sons, Inc.

[26]   Gonzalez, R.C., Woods, R.E. (2002). Digital Image Processing (Second Edition).
Pearson Education Inc.

[27]   Fan, Y., Jiang, T., Evans, D.J. (2002). Medical Image Registration Using Parallel
Genetic Algorithms. Proceedings of Applications of Evolutionary Computing
EvoWorkshops 2002, 304-314

[28]   Maslov, I.V., Gertner, I. (2001). Gradient-Based Genetic Algorithms in Image Registration. Student Projects at City University of New York, 2001

[29]   Maslov, I.V., Bruno, B., Fogel, D.B., Bezdek, J.C. (2003). Using Local Response Analysis to Reduce the computational Cost of Image Registration with the Hybrid Genetic Algorithm. SPIE Proceedings 2003, 125-132

[30]   Keogh, E. Wei, L., Xi, X., Lee, S., Vlachos, M. (2006). LB_Keogh Supports Exact Indexing of Shapes under Rotation Invariance with Arbitrary Representations and Distance Measures. Proceedings of the 32nd international conference on Very Large Data Bases, Vol. 32, 882-293

[31]   Tao, Y., Ioerger, T.R., Tang, Y.Y. (2001). Extraction of Rotation Invariant Signature Based on Fractal Geometry. Image Processing, IEEE Vol.1, 1090-1093

[32]   Sullivan, J.M., Zhang, J.Q. (2004). MIVA User Manual, Version 2.0. Retrieved April 17, 2007, http://ccni.wpi.edu/cwb-doc

[33]   Johnson, H.J., Christensen, G.E.(2002). Consistent landmark and intensity-based image registration. IEEE transactions on Medical Imaging 2002, 21(5), 450-461

[34]   Rohr, K., Stiehl, H.S., Sprengel, R., Buzug, T.M., Weese, J., Kuhn, M.H. (2001). Landmark-based elastic registration using approximating thin-platesplines. IEEE Transactions on Medical Imaging 2001, 20(6), 526-534

[35]   Hellier, P., Barillot, C. (2003). Coupling dense and landmark-based approaches for nonrigid registration. IEEE Transactions on Medical Imaging 2003, 22(2), 217-227

[36]   Collins, D.L., Neelin, P., Peters, T.M., Evans, A.C. (1994). Automatic 3D intersubject registration of MR volumetric data in standardized Talairach space. Journal of Computer Assisted Tomography, 18, 192-205

[37]   Evans, A.C., Marrett, S., Collins, L., Peters, T.M. (1989). Anatomical-functional correlative analysis of the human brain using three dimensional imaging systems. Medical Imaging: image processing, Bellingham, WA: SPIE press, Vol. 1092, 264-274

[38]   Hill, D.L.G., Hawkes, D.J., Crossman, J.E., Gleeson, M.J., Cox, T.C., Barcey, E.E., Strong, A.J., Graves P. (1991). Registration of MR and CT images for skull base surgery using pointlike anatomical features. British Journal of Radiology, 64(767), 1030-1035

[39]   Hill, D.L.G., Hawkes, D.J., Hardingham, C.R. (1991). The use of Anatomical Knowledge to register 3D blood vessel data derived from DSA with MR images. Medical imaging: image processing, Bellingham, WA. SPIE press, Vol. 1445, 348-357

[40]   Peters, T., Davey, B., Munger, P., Comeau, R., Evans, A., Olivier, A. (1996). Three-dimensional Multimodal Image-guidance for Neurosurgery. IEEE Transactions on Medical Imaging, 15(2), 121-128

[41]   Chen, C., Pelizzari, C.A., Chen, G.T.Y., Cooper, M.D., Levin, D.N. (1987). Image Analysis of PET data with the aid of CT and MR Images. Information Processing in Medical Imaging, 601-611

[42]   Levin, D.N., Pelizzari, C.A., Chen, G.T.Y., Chen, C.T., Cooper, M.D. (1988). Retrospective Geometric Correlation of MR, CT, and PET Images. Radiology, 169(3), 817-823

[43]   Pelizzari, C.A., Chen, G.T.Y., Spelbring, D.R., Weichselbaum, R.R., Chen, C.T. (1989). Accurate Three-dimensional Registration of CT, PET and/or MR Images of the Brain. Computer Assisted Tomography, 13(1), 20-26

[44]   Bharatha, A., Hirose, M., Hata, N., Warfield, S.K., Ferrant, M., Zou, K.H. (2001). Evaluation of Three-dimensional Finite Element-based Deformable Registration of Pre- and Intraoperative Prostate Imaging. Medical Physics, 28(12), 2551-2560

[45]   Ferrant, M., Nabavi, A., Macq, B., Jolesz, F.A., Kikinis, R., Warfield, S.K. (2001). Registration of 3-d intraoperative MR images of the brain using a finite-element biomechanical model. IEEE Transactions on Medical Imaging, 20(12), 1384-1397

[46]   Vaillant, M., Davatzikos, C. (1999). Hierarchical Matching of Cortical Features for Deformable Brain Image Registration. Proc. Information Processing in Medical Imaging: 16th International Conference, Retrieved April 17, 2007, from the website of Scientific Literature Digital Library: http://citeseer.ist.psu.edu/vaillant99hierarchical.html

[47]   Penney, G.P., Weese, J., Little, J.A., Desmedt, P., Hill, D.L.G., Hawkes, D.J. (1998).   Similarity Measures for Use in 2-D-3-D Medical Image Registration. IEEE Transactions on Medical Imaging, 17(4), 586-595

[48]   Rueckert, D., Sonoda, L.I., Hayes, C., Hill, D.L.G., Leach, M.O., Hawkes, D.J. (1999). Nonrigid Registration Using Free-form Deformations: Application to Breast MR Images. IEEE Transactions on Medical Imaging, 18(8), 712-721

[49]   Holden, M., Hill, D.L.G., Denton, E.R.E., Jarosz, J.M., Cox, T.C.S., Rohlfing, T., Goodey, J., Hawkes, D.J. (2000). Voxel Similarity Measures for 3-D Serial MR Brain Image Registration. IEEE Transactions on Medical Imaging, 19(2), 94-102

[50]   Pluim, J.P.W., Maintz, J.B.A., Viergever, M.A. (2003). Mutual-information-based Registration of Medical Images: a Survey. IEEE Transactions on Medical Imaging, 22(8), 986-1004

[51]   Zhang, J.Q., Sullivan, J.M., Kulkarni, P.P., Brevard, M., Benz, U., Yu, H.L. (2003). Intermodality Registration via Interactive Graphics Coupled with A.I.R. Intramodality Registration. Proc. 11th ISMRM, No. 3430

[52]   Yu, H.L., Sullivan, J.M., Ghadyani, H.R., Zhang, J.Q. (2005). Image Registration by Global Maximization of Mutual Information Based on a Genetic Algorithm. Proc. 13th ISMRM, No. 1567

[53]   Huang, W., Sullivan, J.M. (2006). An Automated Image Registration Methodology Using a Hybrid Genetic Algorithm Strategy. Proc. 14th ISMRM, No. 2006

[54]   Huang, W., Sullivan, J. M., Kulkarni, P.P., Murugavel, M. (2006). 3D Image Registration Using Voxel Similarity Measurements Based on a Genetic Algorithm, S.P.I.E. Medical Imaging Conferences, 6144-106

[55]   Periaswamy, S. (2003). General-purpose Medical Image Registration. a PhD dissertation in Computer Science at Dartmouth College

[56]   Noblet, V., Heinrich, C., Heitz, F., Armspach, J.P. (2005). 3-D Deformable Image Registration: A Topology Preservation Scheme Based on Hierarchical Deformation Models and Interval Analysis Optimization. IEEE Transactions on Image Processing, 14(5), 553-566

[57]   Woods, R.P., Grafton, S.T., Holmes, C.J., Cherry, S.R., Mazziotta, J.C. (1998). Automated Image Registration: I. General Methods and Intrasubject, Intramodality Validation. Journal of Computer Assisted Tomography. 22(1), 139-152

[58]   Woods, R.P., Grafton, S.T., Watson, J.D.G., Sicotte, N.L., Mazziotta, J.C. (1998). Automated Image Registration: II. Intersubject Validation of Linear and Nonlinear Models. Journal of Computer Assisted Tomography. 22(1), 153-165

[59]   Little, J.A., Hill, D.L.G., Hawkes, D.J. (1997). Deformations Incorporating Rigid Structures. Computer Vision Image Understanding, 66(2), 223-32

[60]   Xie, Z., Farin, G.E. (2004). Image Registration Using Hierarchical B-Splines. IEEE Transactions on Visualization and Computer Graphics, 10(1), 85-94

[61]   Pluim, J.P.W., Maintz, J.B.A., Viergever, M.A. (2003). Mutual Information Based Registration of Medical Images: A Survey. IEEE Transactions on Medical Imaging, 22(8), 986-1004

[62]   Maes, F., Collignon, A., Vandermeulen, D., Marchal, G., Suetens, P. (1997). Multimodality Image Registration by Maximization of Mutual Information. IEEE Transactions on Medical Imaging, 16(2), 187-198

[63]   Zienkiewicz, O.C., Taylor, R.L. & Zhu, J.Z. (2005). The Finite Element Method: Its Basis and Fundamentals. (Sixth Edition). Butterworth-Heinemann

[64]   Krol, A., Coman, I.L., Mandel, J.A., Baum, K., Luo, M., Feiglin, D.H., Lipson, E.D., Beaumont, J. (2003). Inter-Modality Non-Rigid Breast Image Registration Using Finite-Element Method. IEEE Nuclear Science Symposium Conference Record, Vol. 3, 1958-1961

[65]   Xuan, J., Wang, Y., Freedman, M.T., Adali, T., Shields, P. (2006). Nonrigid Medical Image Registration by Finite-Element Deformable Sheet-Curve Models. International Journal of Biomedical Imaging, 2006(2006), 1-9

[66]   Lemieux, L., Wieshmann, U.C., Moran, N.F. Fish, D.R., Shorvon, S.D. (1998). The Detection and Significance of Subtle Changes in Mixed-signal Brain Lesions by Serial MRI Scan Matching and Spatial Normalization. Medical Image Analysis, 2(3)**,** 227–242

[67]   Woods, R.P., Cherry, S.R., Mazziotta, J.C. (1992). Rapid automated algorithm for aligning and reslicing PET images. Journal of Computer Assisted Tomography. 16(4), 620–633

[68]   Barber, D.C. (1992). Registration of Low Resolution Medical Images. Physics in Medicine and Biology, 37(7), 1485-1498

[69]   Zubal, I.G., Spencer, S.S., Imam, K., Seibyl, J., Smith, E.O., Wisniewski, G., Hoffer, P.B. (1995). Difference images calculated from ictal and interictal technetium-99m-HMPAO SPECT scans of epilepsy. Journal of Nuclear Medicine, 36(4), 684-689

[70]   Shen, D. (2007). Image registration by local histogram matching. Pattern Recognition, 40(4), 1161-1172

[71]   Knops, Z.F., Maintz, J.B.A., Viergever, M.A., Pluim, J.P.W. (2003). Normalized mutual information-based registration using K-means clustering-based histogram binning. Proc. SPIE Medical Imaging, Vol. 5032, 1072-1080

[72]   Hill, D.L.G. (1993). Combination of 3D Medical Images from Multiple Modalities. Ph.D. Thesis, University of London

[73]   Hill, D.L.G., Hawkes, D.J. (1994). Medical Image Registration Using Voxel Similarity Measures. In Applications of Computer Vision in Medical Image Processing, AAAI spring symposium series, 34–37

[74]   Lehmann, T., Goerke, C., Schmitt, W., Kaupp, A., Repges, R. (1996). A Rotation-extended Cepstrum Technique Optimized by Systematic Analysis of Various Sets of X-ray Images. In Loew, M. H. and Hanson, K. M. (eds), SPIE Medical Imaging: Image processing, Vol. 2710, 390–401

[75]   Chen, H., Varshney, P.K. (2003). Mutual Information-based CT-MR Brain Image Registration Using Generalized Partial Volume Joint Histogram Estimation, IEEE transactions on medical imaging, Vol. 22, 1111-1119

[76]   Chen, H., Lin, T., Hsieh, C. (2006). An overlap-invariant mutual information estimation method for image registration, Proc. SPIE Applications of Digital Image Processing, 6312, 631207

[77]   ITK Mutual Information (2005). Retrieved April 17, 2007, from the website of ITK: NLM Insight Segmentation & Registration Toolkit:

http://www.itk.org/Wiki/ITK_Mutual_Information

[78]   Ohtake, Y., Belyaev, A.G., Bogaevski, I.A. (2000). Polyhedral Surface Smoothing with Simultaneous Mesh Regularization. IEEE Geometric Modeling and Processing 2000, theory and applications, 229-237

[79]   Lomonosov, E., Chetverikov, D., Ekart, A. (2006). Pre-registration of Arbitrarily Oriented 3D Surfaces Using a Genetic Algorithm. Pattern Recognition Letters, 27(11), 1201-1208

[80]   Chow, C.K., Tsui, H.T., Lee, T. (2004). Surface Registration Using a Dynamic Genetic Algorithm. Pattern Recognition, 37(1), 105-117(13)

[81]   Swathanthira-Kumar, M., Sullivan, J.M. (2007). Automatic Brain Cropping and Atlas Slice Matching Using a PCNN and Generalized Invariant Hough Transform Process. SPIE Medical Imaging Conferences, #6512-24

[82]   Sullivan, J.M., Zhang, Q.Y. (1997). Adaptive Mesh Generation Using a Normal Offsetting Technique. Finite Elements in Analysis and Design, 25(2), 275-295

[83]   Huang, W., Sullivan, J.M., Ghadyani, H., Murugavel, M. (2007). Automated Image Registration Based Upon an Elastic Finite Element Formulation, Joint Annual Meeting ISMRM-ESMRMB 2007, #5209

[84]   Zhang, J.Q., Sullivan, J.M., Ghadyani, H. (2005). MRI Guided 3D Mesh Generation and Registration for Biological Modeling. Journal of Computing and Information Science in Engineering 2005, 5(4), 283-290

[85]   Huang, W., Sullivan, J.M., Ludwig, R., Kulkarni, P., Zhang, J.Q. & King, J.A. (2004). Stair-Stepped Removal via Automatic Linearization for Marching Cubes Formulations. Proc. 12th ISMRM. 2004, No. 756

[86]   Wu, Z., Sullivan, J.M. (2003). Multiple Material Marching Cubes Algorithm. International Journal for Numerical Methods in Engineering, 58(2), 189–207

[87]   Zhang, J.Q., Sullivan, J.M., Ghadyani, H.R., Benz, U., Wu, Z. & Meyer D.M. (2004). MR Image Guided 3D Registration and Mesh Generation for Brain Vasculature Model. Proceedings of the 12th ISMRM, No. 2244

[88]   Nielsen, L.K. (2003). Elastic Registration of Medical MR Images, Cand. Scient. Thesis in Computational Science. Retrieved April 17, 2007, from Matematisk Institute website: http://www.mi.uib.no/~tai/thesis/nielsen.pdf

[89]   Wang, Y., Staib, L.H. (1998). Elastic Model Based Non-rigid Registration Incorporation Statistical Shape Information, Proc. the First International Conference on Medical Image Computing and Computer-Assisted Intervention, Vol. 1496, 1162-1173

[90]   Zhang, J., Sullivan, J. M., Wu, Z., Huang W. & Kinkar S. (2005). A Framework for Multi-Modality Imaging Registration and Visualization, Proc. 8th US National Congress on Computational Mechanics, 2005

[91]   Kulkarni, P.P., Sullivan, J.M., Ghadyani, H.R., Huang, W., Wu, Z. & King, J.A. (2003). Automatic Segmentation of a Rat Brain Atlas via a Multiple-Material Marching-Cube Strategy, Proc. 11th ISMRM, 2003

[92]   Sullivan, J.M., Huang, W., Zhang J. & Wu, Z. (2003). Automatic Linearization During Multiple-Material Surface Mesh Generation, Proc. 7th US National Congress on Computational Mechanics, 2003

[93]   Brain Voyager: http://www.brainvoyager.de

[94]   Stimulate: http://www.cmrr.umn.edu/stimulate

[95]   AIR Registration Package: http://bishopw.loni.ucla.edu/AIR5/

[96]   MIVA: http://ccni.wpi.edu/cwbench/cwbench-tiles.jsp

[97]   Wu, Z., Sullivan, J.M. (2002). Multiple Material Marching Cubes Algorithm, International Journal for Numerical Methods in Engineering, 58(2), 189-207

[98]   Matlab: http://www.mathworks.com

[99]   Burkardt, J. (2007). Geometric Calculations. Retrieved April 17, 2007, from John Burkardt's web page at Florida State University:

http://people.scs.fsu.edu/~burkardt/m_src/geometry/geometry.html

[100]	Saykol, E., Gudukbay, U., Ulusoy, O. (2002). A Histogram-based Approach for Object-based Query-byshape-and-color in Image and Video Databases. Image and Vision Computing, 23(2005), 1170-1180

[101]	Keogh, E., Ratanamahatana, C.A. (2005). Exact Indexing of Dynamic Time Warping. Knowledge and Information Systems, 7(3),358-386

[102]	Brock, K.K., Sharpe, M.B., Dawson, L.A., Kim, S.M., Jaffray, D.A. (2005). Accuracy of Finite Element Model-based Multi-organ Deformable Image Registration. Medical Physics 2005, 32(6), 1647-1659

[103]	Alterovitz, R., Goldberg, K., Pouliot, J., Hsu, I.J., Kim, Y., Noworolski, SM., & Kurhanewicz, J. (2006). Registration of MR Prostate Images with Biomechanical Modeling and Nonlinear Parameter Estimation. Medical Physics, 33(2), 446-454

[104]	Huang, C., Lee, J., Huang, J. (2005). Registration of CT Image and Facial Surface Data Using Adaptive Genetic Algorithm. Biomedical Engineering Appl. Basis. & Comm., Vol. 17, 201-206

[105]	Zhou, Y. (2006). Study on Genetic Algorithm Improvement and Application. a Thesis for the Degree of Master of Science, submitted to Worcester Polytechnic Institute

[106]	Park, J., Lee, C., Han, M. (1993). Robust and Efficient Genetic Crossover Operator: Homologous Recombination, Proc. of 1993 International Joint Conference on Neural Networks, 2975-2978

[107]	Sywerda, G. (1989). Uniform Crossover in Genetic Algorithms, Proc. of the third international conference on Genetic Algorithms, 2-9

[108]   Srinivas, M., Patnaik, L.M. (1994). Genetic Algorithms: a survey. Computer, Vol. 27(6), 17-26

[109]   GNU Free Documentation License. Retrieved April 17, 2007, from Wikipedia web site: http://en.wikipedia.org/wiki/GNU_Free_Documentation_License

[110]   Hu, Q., Wu, H., Chen, Q., Chen, Y. (2006). Study on a New Heuristic Crossover for the Traveling Salesman Problem. Chinese Control Conference 2006, 1442-1447

[111]   Chu, C., Tsai, C. (2001). A Heuristic Genetic Algorithm for Grouping Manufacturing Cells. IEEE Proceedings of the 2001 congress on evolutionary computation, Vol. 1, 310-317

[112]   Herrera, F., Lozano, M., Sanchez, A.M. (2005). Hybrid Crossover Operators for Real-coded Genetic Algorithms: an Experimental Study. Soft Computing, 9(4), 280-298

[113]   Herrera F., Lozano M., Sanchez, A.M. (2003). A taxonomy for the crossover operator for real-coded genetic algorithms. An experimental study. International Journal of Intelligent Systems, 18(3), 309–338

[114]   Genetic Server and Genetic Library (2006). Retrieved April 17, 2007, from NeuroDimension Website: http://www.nd.com/genetic/

[115]   ITK: NLM Insight Segmentation & Registration Toolkit: http://www.itk.org/

[116]   Ghadyani, H.R., Sullivan, J.M. (2007). Improvement of tetrahedral meshes by optimizing the minimum local angle, SPIE. Medical Imaging Conferences 2007, #6509-91

[117]   Gibson, S.F.F., Mirtich, B. (1997). A Survey of Deformable Modeling in Computer Graphics. Mitsubishi Electric Information Technology Center America, 1997

[118]   McInerny, T. & Terzopoulos, D. (1996). Deformable Models in Medical Image Analysis: a Survey. Medical Image Analysis, 1(2), 91-108

[119]   Barsky, B.A. (1993). Rational Beta-splines for representing curves and surfaces. IEEE Computer Graphics and Applications, 13(6), 24-32

[120]   Desbrun, M., Meyer, M., Schroder, P., Barr, A.H. (1999). Implicit Fairing of Irregular Meshes Using Diffusion and Curvature Flow. Proceedings of the 26th annual conference on Computer graphics and interactive techniques, 317-324

[121]   Dodgson, N. (2000). B-Splines. Retrieved April 17, 2007, from Dr. Neil Dodgson's webpage at University of Cambridge:

http://www.cl.cam.ac.uk/teaching/2000/AGraphHCI/SMEG/node4.html

[122]   Suzanne, M., 3D Free-form Deformation. Retrieved April 17, 2007, from Matthew Ward's home page at Worcester Polytechnic Institute:

http://web.cs.wpi.edu/~matt/courses/cs563/talks/smartin/ffdeform.html

[123]   Sederberg, T.W., Parry, S.R. (1986). Free-form deformation of solid geometric models. Proc. of the 13th annual conference on Computer graphics and interactive techniques, 151-160

[124]   Feng, J., Peng, Q. (2000). B-Spline Free-Form Deformation of Polygonal Objects through Fast Functional Composition. Geometric Modeling and Processing 2000, 408-414

[125]   Wang, Y., Xiong, Y., Xu, K., Tan, K., Guo, G. (2006). A mass-spring model for surface mesh deformation based on shape matching. Proc. of the 4th international conference on Computer graphics and interactive techniques in Australasia and Southeast Asia, 375-380

[126]   Choi, Y., Hong, M., Choi, M., Kim, M. (2005). Adaptive surface-deformable model with shape-preserving spring: Research Articles, Computer Animation and Virtual Worlds, 16(1), 69-83

[127]   Bara D. & Witkin, A. (1992). Dynamic simulation of non-penetrating flexible bodies. Proceedings of the 19th annual conference on Computer graphics and interactive techniques, 303-308

[128]   Matuszewski, B.J., Shen, J.K., Shark, L.K. Elastic Image Matching with Embedded Rigid Structures Using Spring-mass System. IEEE Proceedings of 2003 International Conference on Image Processing, Vol. 2, 937-940

[129]   Singh, M., Information along contours. Retrieved April 17, 2007, from Manish Singh's web page at Rutgers University:

http://ruccs.rutgers.edu/~manish/demos/curveinfo.html

[130]   Lynch, D.R. (2005). Numerical Partial Differential Equations for Environmental Scientists and Engineers. Springer Verlag

[131]   Sullivan, J.M., Online Notes of Course "Computational Methods for PDEs in Engineering and Science" , Retrieved April 17, 2007, from Sullivan's website at Worcester Polytechnic Institute: http://users.wpi.edu/~sullivan/WebSite-ME515/ME515-Course.htm

[132]   Gao, C., Tay, F.E.H., Nowinski, W.L. (2005). A Finite Element Method Based Deformable Brain Atlas Suited for Surgery Simulation. IEEE-EMBS 27th Annual Conference of the Engineering in Medicine and Biology Society, 4337-4340

[133]   Delinguette, H. (1998). Toward Realistic Soft-tissue modeling in medical simulation. Proceedings of the IEEE 86 (3), 512-523

[134]   Wikipedia: http://en.wikipedia.org/wiki/

[135]   Lam, S.Y., Tong, C.S. (2006). Enhanced Snake algorithm by embedded domain transformation. Pattern Recognition, 39(9), 1566-1574

[136]   Bro-Nielsen, M. (1995). Modeling elasticity in solids using active cubes - application to simulated operations. Computer Vision, Virtual Reality and Robotics in Medecine, 535-541., 1995. Vol. 905 of Lecture Notes in Computer Science.

[137]   Kass, M., Witkin, A. & Terzopoulos, D. (1987). Snakes: active contour models. International J. Computer Vision, 1(4), 321-332

[138]   Montagnat, J., Delingette, H. (1997). A Hybrid Framework for Surface Registration and Deformable Models, Proc. of the 1997 Conference on Computer Vision and Pattern Recognition, 1041-1046

[139]   West, J.B., Maurer, C.R., Dooley, J.R. (2005). Hybrid point-and-intensity-based deformable registration for abdominal CT images. Medical Imaging 2005, Image Processing, Proc. of SPIE, Vol. 5747, 204-211

[140]   Metaxas, D. (1997). Physics-based Deformable Models: Applications to Computer Vision, Graphics, and Medical Imaging. Boston, MA, USA: Kluwer Academic Publishers

[141]   Bara D. & Witkin, A. (1992). Dynamic simulation of non-penetrating exible bodies. In Computer Graphics Proceedings, Annual Conference Series, Proceedings of SIGGRAPH 92, 303-308

[142]   Terzopoulos D. & Qin H. (1994). Dynamic nurbs with geometric constraints for interactive sculpting. ACM Transactions on Graphics, 13(3):103-136

[143]   Imaging Modalities. Retrieved April 17, 2007, from the website of University of Iowa: http://www.radiology.uiowa.edu/healthcare/imaging.html

[144]   Imaging Modalities. Retrieved April 17, 2007 , from web page: http://www.kfshrc.edu.sa/radiology/html/imaging_modalities.html

[145]   Medical Imaging Modalities. (1999). Retrieved April 17, 2007, from UCLA web page: http://laxmi.nuc.ucla.edu:8248/M248_99/intro/lec1_slides/sld003.htm

[146]   Gannot, I. (2007). Imaging modalities. Retrieved April 17, 2007, from Dr. Isreal Gannot's website: http://www.eng.tau.ac.il/~gannot/MI/Imaging.ppt

[147]   Carlson, C.A. (1999). Imaging Modalities in X-ray Computerized Tomography and in Selected Volume Tomography. Physics in Medicine and Biology, 44(3), 23-56

[148]   Riedel, E., Gibson, G., Faloutsos, C. (1998). Active Storage for Large-scale Data Mining and Multimedia. Proceedings of the 24th International Conference on Very Large Databases, 62-73

[149]   Morel, F., Rauch, C., Petit, E., Piton, A., Theret, N., Coles, B., Guillouzo, A. (2004). Gene and Protein Characterization of the Human Glutathione S-Transferase Kappa and Evidence for a Peroxisomal Localization. Journal of Biological Chemistry, 279(16), 16246-16253

[150]   Machado, A.M.C., Gee, J.C., Campos, M.F.M. (2000). A Factor Analytic Approach to Structural Characterization, Proceedings of IEEE Workshop on Mathematical Methods in Biomedical Image Analysis, 219-226

[151]   Staib, L.H., Jackowski, M., Papademetris, X. (2006). Brain Shape Characterization from Deformation. 3rd IEEE International Symposium on Biomedical Imaging, 1140-1143

[152]   Klette, G., Pan, M. (2005). Characterization of Curve-like Structures in 3D Medical Images. Proceedings of Image and Vision Computating, 357-362

[153]   Geometric Operations. Retrieved April 17, 2007, from web site of Image Processing Learning Resources: http://homepages.inf.ed.ac.uk/rbf/HIPR2/geomops.htm

[154]   Yu, H. (2005). Automatic Rigid and Deformable Medical Image Registration. a dissertation submitted to the faculty of the Worcester Polytechnic Institute

[155]   Johansson, M. (2006). Image Registration with Simulated Annealing and Genetic Algorithms. Master of Science Thesis, Stockholm, Sweden

[156]   Silva, L., Bellon, O.R.P. (2003). Enhanced, Robust Genetic Algorithms for Multiview Range Image Registration. Proceedings of the Fourth International Conference on 3-D Digital Imaging and Modeling, IEEE Fourth International Conference on 3-D Digital Imaging and Modeling, 268-275

[157]   Brunnstrom K. & Stoddart, A. (1996). Genetic Algorithms for Free-form Surface Matching. Proc. of the 13th Intl. Conf. on Pattern Recognition, Vol. 4, 689-693

[158]   Robertson C. & Fisher, R. (2002). Parallel Evolutionary Registration of Range Data. Computer Vision and Image Understanding, 87(1), 39-50

[159]   Evolutionary Algorithms: Mutation. Retrieved April 17, 2007, from GEATbx – the Genetic and Evolutionary Algorithm Toolbox for Matlab:

http://www.geatbx.com/docu/algindex-04.html

[160]   Mühlenbein, H. and Schlierkamp-Voosen, D. (1993). Predictive Models for the
Breeder Genetic Algorithm: I. Continuous Parameter Optimization. Evolutionary
Computation, 1 (1), 25-49

[161]   Bäck, T. (1996). Evolutionary Algorithms in Theory and Practice - Evolution
Strategies, Evolutionary Programming, Genetic Algorithms. New York, Oxford: Oxford
University Press

[162]   Haupt, R.L. (2000). Optimum Population Size and Mutation Rate for a Simple
Real Genetic Algorithm that Optimizes Array Factors. IEEE Antennas and Propagation
Society International Symposium, Vol. 2, 1034-1037

[163]   Johnson, J.L., Padgett, M.L. (1999). PCNN Models and Applications. IEEE
Transactions on Neural Networks, 10(3), 480-498

[164]   Ranganath, H.S., Juntimad, G. (1999). Object Detection Using Pulse Coupled
Neural Networks. IEEE Transactions on Neural Networks, 10(3), 615-620

[165]   Bosacchi, B., Fogel, D.B., Bezdek, J.C. (2000). Neural Network for Image
Segmentation, Proc. SPIE Applications and Science of Neural Networks, Fuzzy Systems,
and Evolutionary Computation III, Vol. 4120, p. 28-35

[166]   Linblad T. & Kinser, J.M. (2005). Image Processing using Pulse-Coupled Neural
Networks (Second Edition). Springer

[167]   Keller, P.E., McKinnon, A.D. (1999). Segmentation of medical imagery with
pulse-coupled neural networks. IEEE International Joint Conference on Neural Networks,
Vol. 4, 2659-2663

[168]   Kuntimad, G., Ranganath, H.S. (1999). Perfect Image Segmentation Using Pulse Coupled Neural Networks. IEEE Transactions on Neural Networks, 10(3), 591-598

[169]   Wu, S., Melo, V.F. (2004). A Deformable Surface Model on the Basis of the Theory of a Cosserat Surface. IEEE Proc. 17th Brazilian Symposium on Computer Graphics and Image Processing, 274-281

[170]   Valverde, F.L., Guil, N., Munoz, J., Li, Q., Aoyama, M., Dio, K. (2001). A Deformable Model for Image Segmentation in Noisy Medical Images. IEEE Proceedings of International Conference on Image Processing, Vol. 3, 82-85

[171]   Valverde, F.L., Guil, N., Munoz, J. (2004). Segmentation of Vessels from Mammograms Using a Deformable Model. Computer Methods Programs in Biomedicine, 73(3), 233-247

[172]   Ghanei, A., Soltanian-Zadeh, H., Ratkewicz, A., Yin, F. (2001). A Three-dimensional Deformable Model for Segmentation of Human Prostate from Ultrasound Images. Medical Physics, 28(10), 2147-2153

[173]   Sullivan, J.M., Wu, Z., Kulkarni, A. (2000). 3D Volume Mesh Generation of Human Organs Using Surface Geometries Created from the Visible Human Data Set. Retrieved April 17, 2007, from NIH website:

http://www.nlm.nih.gov/research/visible/vhpconf2000/AUTHORS/SULLIVAN/SULLIVAN.HTM

[174]   Wu, Z. (2001). Accurate and Efficient Three-Dimensional Mesh Generation for Biomedical Engineering Applications. a PhD dissertation submitted to Worcester Polytechnic Institute, Department of Mechanical Engineering

[175]   Lorensen, W.E., Cline, H.E. (1987). Marching Cubes: A High Resolution 3D Surface Construction Algorithm. Computer Graphics, 21(4), 163-169

[176]   Ferris, C.F., Kulkarni, P., Sullivan, J.M. (2005). Pup Suckling Is More Rewarding Than Cocaine: Evidence from Functional Magnetic Resonance Imaging and Three-Dimensional Computational Analysis. The Journal of Neuroscience, 25(1), 149-156

[177]   Wu, Z., Sullivan, J.M. (2001). Automatic Finite Element Mesh Generation from MRI Scans for Breast Cancer Investigations. Proceedings of the IEEE 27th Annual Northeast Bioengineering Conference, 59-60

[178]   Bruckner, T., Lucht, R., Brix, G. (2000). Comparison of rigid and elastic matching of dynamic magnetic resonance mammographic images by mutual information. Medical Physics, 27(10), 2456-2461

[179]   Registration of volumetric images which are relatively elastically deformed by matching surfaces, http://www.freepatentsonline.com/5633951.html

[180]   AFNI: http://afni.nimh.nih.gov/afni/

[181]   NIH Visible Human Project. Retrieved April 17, 2007, from NIH website: http://www.nlm.nih.gov/research/visible/visible_human.html

[182]   Kulkarni, P.P. (2005). Functional MRI Data Analysis Techniques and Strategies to Map the Olfactory System of a Rat Brain. a PhD dissertation submitted to Worcester Polytechnic Institute, Department of Mechanical Engineering

[183]   Vannah, W.M. (1993). Modelling the Mechanics of Narrowly Contained Soft Tissues: The Effect of Specification of Poisson's Ratio. Journal of Rehabilitation Research and Development, 30(2), 205-209

[184]   Choi, A.P.C., Zheng, Y.P. (2005). Estimation of Young's Modulus and Poisson's Ratio of Soft Tissue from Indentation Using Two Different-sized Indentors: Finite Element Analysis of the Finite Deformation Effect. Journal of medical and biological engineering and computing, 43(2), 258-264

Appendices

Appendix I   Co-registration steps in MIVA
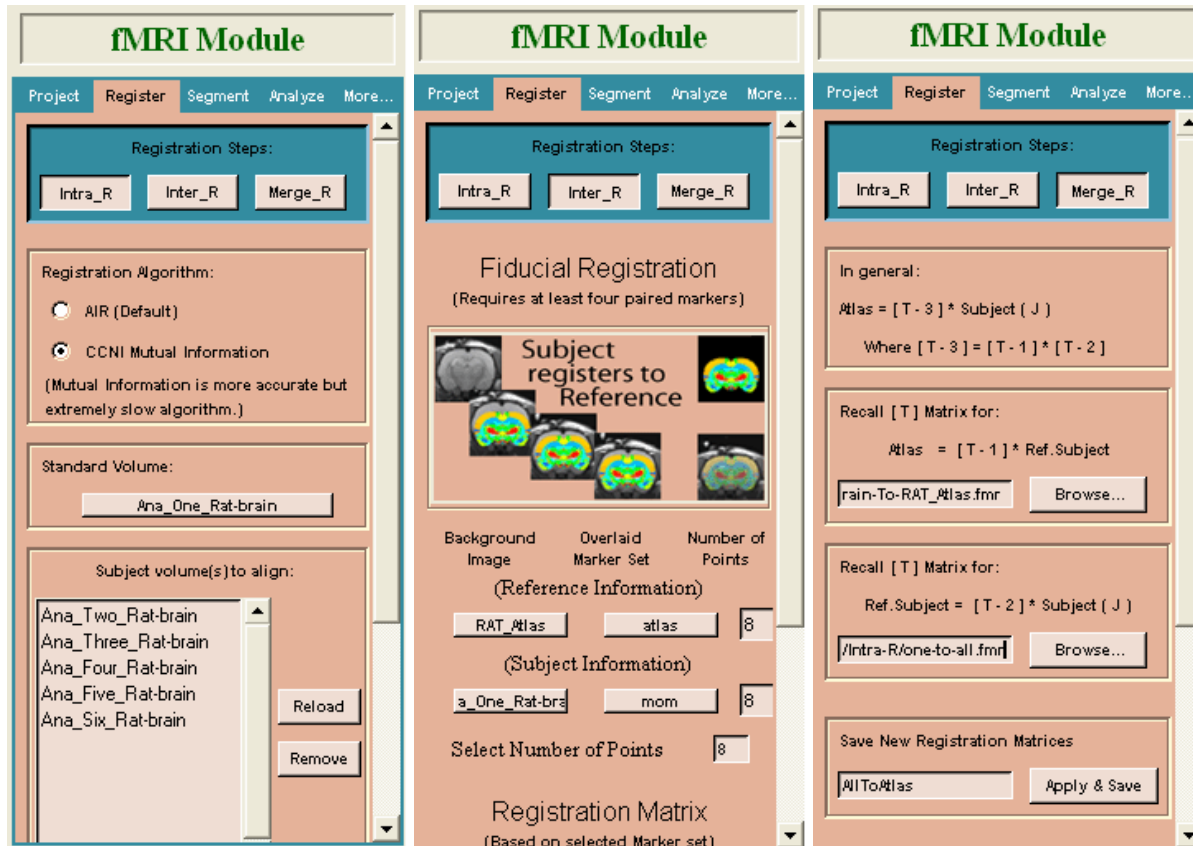
(a) intra registration   (b) inter registration   (c) merge registration

Appendix II fMRI analysis

Functional magnetic resonance imaging (fMRI) is a relatively new procedure that uses MR imaging to measure the quick, tiny metabolic changes that take place in an active part of the brain. User can specify the desired regions of interest via a user friendly graphic interface, e.g. a tree browser in MIVA (Figure II-1). Since all subject images are aligned to the atlas, a series of color-coded mapped files can be created according to the regions of interest. User can then do fMRI analysis such as t-test analysis and a composite result subject can be constructed (Figure II-2).
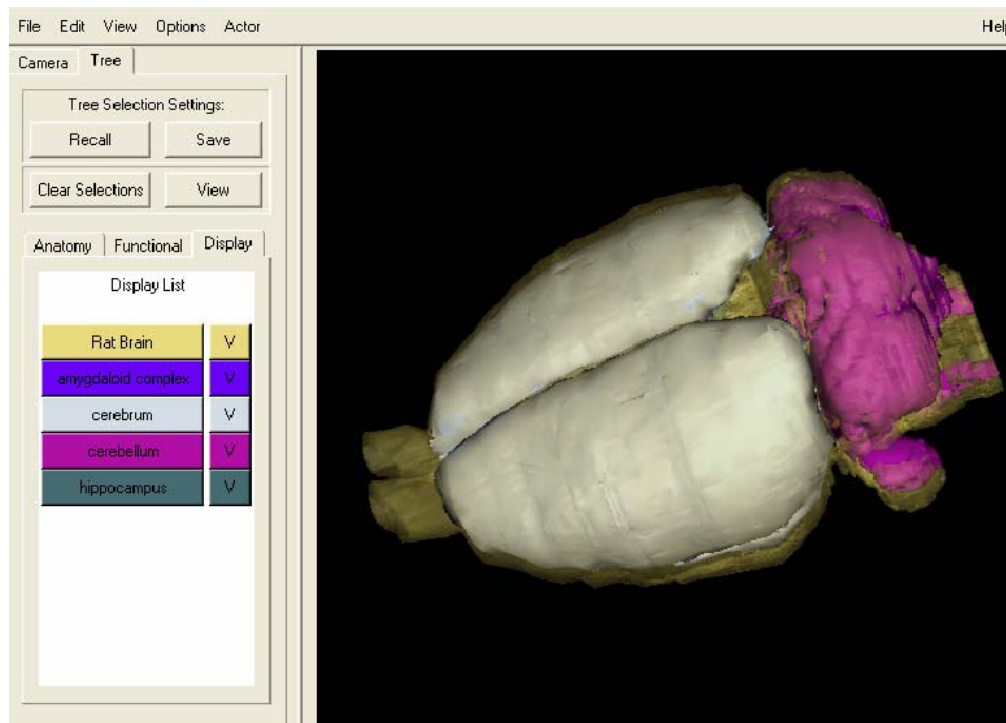
Figure II-1 Specify the regions of interest via Tree-browser in MIVA
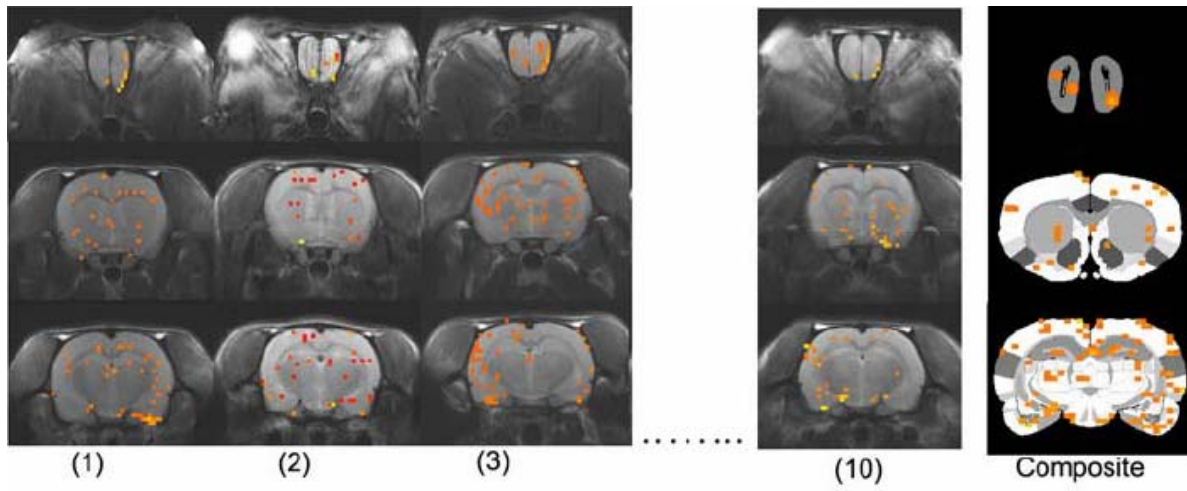
Figure II-2   Composite fMRI response of ten subjects created to map olfactory system in the atlas